Cellular biomechanics in 2D and 3D epithelial model tissues: from keratin intermediate filaments to breast gland *in vitro* reconstructed basement membranes

Doctoral thesis

submitted in partial fulfillment of the
requirements for the degree of

Doctor rerum naturalium (Dr. rer. nat.)

to the
Faculty of Mathematics and Natural Sciences of the
Rheinischen Friedrich-Wilhelms-Universität Bonn
by

Gloria Fabris
from Trieste

Bonn, February 2016

Angefertigt mit Genehmigung der Mathematisch-Naturwissenschaftlichen Fakultät der Rheinischen Friedrich-Wilhelms-Universität Bonn

1. Gutachter: Prof. Dr. Rudolf Merkel
2. Gutachter: Prof. Dr. Ulrich Kubitscheck

3. Gutachter: Prof. Dr. Werner Mader
4. Gutachter: Priv.-Doz. Dr. Gerhild van Echten-Deckert

Tag der mündlichen Prüfung: 18.11.2016
Erscheinungsjahr: 2017

Acknowledgements

While working on my PhD project, I was lucky enough to receive support and encouragement from many people.

First and foremost, I sincerely want to thank my Doktorvater, Prof. Rudolf Merkel, for having been such a precious mentor during these three years. From the day he welcomed me in Jülich, his enthusiasm and availability to always discuss the latest problem have been highly motivating, as well as incredibly helpful. But mostly, his deep passion for science and his intellectual honesty will remain a bright example for me to follow; and of this I am sincerely grateful.

Besides my promotor, I would like to thank the other doctoral referees, Prof. Ulrich Kubitscheck, Prof. Werner Mader and Dr. Gerhild van Echten-Deckert, for accepting to be part of the PhD commission and taking the time to review my work.

When arriving at the ICS-7, I wanted to study the physics of living systems: for being my personal "gurus" in the reign of biology, I especially want to thank Dr. Bernd Hoffmann and Dr. Erik Noetzel-Reiss. Along with Erik, for the fruitful daily teamwork, I cannot but acknowledge the precious collaboration of my closest lab partners, Lena Ramms and Aljona Gaiko-Shcherbak. Their company has made the work feel much lighter, and our many discussions have rendered my understanding of cellular biology much more concrete!
During his stay at the ICS-7, Toni Marković has been a great summer student. I especially want to thank him for the measurements on keratin monolayers.
A big thanks also to Dr. Jeong-Hun Yi for the constructive discussions on continuum mechanics and the very helpful introduction to FEM simulations. My most sincere gratitude then goes to Georg Dreissen and Dr. Ronald Springer (a.k.a. "The I-Tea"); their fantastic IT support and their readiness to always help solve yet another MatLab-related issue surely make the life of us students much simpler!

The many discussions I had with Dr. Evelin Jaschinski during our time sharing an office have been precious and intellectually stimulating: I sincerely appreciated the great colleague she has been.
For his passion in constantly creatively solving the strangest lab-problems, and for the fun evenings spent together at the LSM, I want to acknowledge the precious support of Nico Hampe. To Nils Hersch and Simone Born, the "laboratory wizards" I owe my gratitude for their endless patience and for introducing me to the practices of cell culture.
Through her constant readiness to always help with a smile, Claudia Klamandt deserved my warmhearted gratitude: she made my first steps in a scary world of German paperwork much less scary! And thanks to Wolfgang Rubner for all the provocative talks about Italian politics and French wine!
Looking back, I will always think with affection at the whole group of ICS-7 colleagues: Benni, Babsi, Agnes, Guillermo, Tobi, Britta, Sabine, Zhanna, Kritika and Galiya. They all helped to create the welcoming atmosphere which over time allowed me to go from feeling like the italian newcomer to someone who is integrally part of the group.

Last but not least, stepping outside our institute's borders, I want to mention the BioSoft fellows and our coordinator, Thorsten Auth, for the stimulating discussions and interesting experiences related to the IHRS graduate school, which I enjoyed tremendously.

But, above all, my deepest thanks goes without doubt to Evelin, Lena and Ronald. For having become my dear friends, for having made me feel at home in a new country and for having taught me so much of this incredibly frustrating and yet wonderful language that is German. This whole experience would not have been as rich without them. I am grateful when I rethink of all the good memories of our time in Jülich, and I am sure that many more are still ahead!

Finally, for being such an immensely enriching presence in my life, I feel the need of thanking my dearest Mattias with my whole heart.
And for their infinite encouragement, dedication, and love, a most grateful thought goes to my parents, Clementina and Franz, together with the rest of my family (in Italy and in Flanders). You are always present, even from far away.

Abstract

The mechanical organization of biological tissue is crucial to the load-transmitting capacity of our bodies, and follows a hierarchical architecture that macroscopically results in organ's formation and function. At the base of such a tightly regulated structure we find single cells, whose mechanical properties are decisive in shaping their interaction with the surrounding environment.
Developing a fundamental understanding of this interplay over a wide range of length scales is essential to reach the deep working knowledge of the biomechanics of multicellular systems required for tissue engineering, surface design and nanomedicine.
In this work, the mechanical properties of epithelial model systems were analyzed at different organizational scales (namely, from single cells to microtissue) by means of atomic force microscopy (AFM) micro- and nano-indentation experiments. Despite the intrinsic difficulty in characterizing soft and heterogeneous biological samples in terms of mechanical response, this technique still offers an exciting possibility to quantitatively probe their viscoelastic behavior.
At first, a murine epidermal cell line completely devoid of keratin intermediate filaments (knock-out keratinocytes) was compared to its wild type counterpart in order to assess the role played by this cytoskeletal component in conferring mechanical stability to single cells. Then, cellular monolayers were analyzed, to validate the relevance of our findings also in a more physiological context. Despite its presence in organs such as skin and nails, which obviously serve a barrier function, the mechanical role of keratin in deeper tissue remained controversial for a long time. Reconstructed keratin polymer gels in fact display properties resemblant of viscoelastic solids; in vivo, the networks are formed of bundles that are relatively sparse and show lower connectivity than other cytoskeletal components. This fact, together with the low values of bending stiffness and extremely high extensibility reported for these filaments, would suggest that keratin networks confer resilience and elasticity to cells, rather than a scaffolding function against compressive stress. Our results though clearly pointed at a substantial softening of keratin-lacking cells, with elasticity moduli differences of 25% to 35% between wild type and knock-out according to the cellular region probed. The presented data represent the first proof

of this effect on the single cell level. Validation of this result further came from the observation that the difference could be partially suppressed by reintroducing a single keratin protein in the mutant cells.

In the second part of this work, a three-dimensional cell culture system mimicking the elementary unit of a human breast gland was analyzed in terms of its biomechanical and permeation properties. The cell line used for this purpose (MCF10A), when grown in an extracellular matrix-resembling environment, can develop into growth-arrested acinar structures which follow the same substantial maturation steps of a human breast gland; cells organize according to an apico-basal polarization scheme, secrete a dense matrix of cross-linked extracellular matrix proteins to surround them (the so called *basement membrane*) and finally develop a hollow lumen necessary, in vivo, for milk production and secretion.

The centrality of breast gland tissue in a context of cancer research cannot be overstated: alveolar units are *the* hotspot for tumor formation, and as such have been the focus of much attention in the past years. Relatively little effort, though, has been dedicated to understanding the mechanical interplay of healthy breast gland microtissues with their surrounding environment, despite the fact that one of the hallmarks of cancer progression is a set of strong alterations in the mechanical phenotype of aberrant cells.

Here, we offer an experimental analysis of the mechanical properties of healthy 3D acinar structures at different developmental stages, and briefly compare them with those of invasive microtissues. The application of different hyperelastic models to the interpretation of nanoindentation experiments is discussed, along with a tentative clarification of some of controversies arising during AFM data analysis.

Additionally, a characterization of isolated basement membranes performed by means of atomic force microscopy imaging, scanning electron microscopy and superresolution light microscopy is reported; experimental evidence suggests that basement membranes act as fundamentally elastic materials whose thickness and structural stability change throughout the different developmental stages. To complement this biomechanical analysis, we investigated the acinar permeation properties; in short, data elucidate that the basement membrane acts as a passive diffusion barrier with a size-selectivity threshold for the retardation of macromolecular permeation of about 40 kDa and a pore size of at least 9 nm. At the same time, it offers a fundamental mechanical shielding function, reaching elastic modulus values of up to about 400 kPa in the fully matured state.

Taken together, the presented data underline how intra- and extra-cellular polymer networks serve a crucial function in defining the mechanical properties of epithelial tissue.

Contents

1. Introduction

The mechanical organization of cells into tissue relies on a complex hierarchy of interactions: on the single cell level, cellular shape and function are highly dependent on the *cytoskeleton*, a dynamic network of biopolymers fundamental for cellular proliferation, locomotion and adhesion [1]. So many are the functions served by these filaments, and so complex is the regulation of their activity, that the decoding of the "cytoskeletal interactome" remains to date one of the open challenges in molecular biology.
Besides the structure of its fundamental building blocks, the intricate architecture of tissue of course also relies on the capacity of single cells to form *connections* between each other. These are offered by *cell-cell contacts*, stable multiprotein complexes that provide anchoring between neighboring cells and at times even "bridge" the cytoskeletal filaments from one cell to the next [2].
An additional element fundamental to the picture is the *extra-cellular matrix* (ECM): a stable collection of proteins, molecules and fibers secreted by cells that provides biochemical and structural support to their surroundings by filling the interstitial space and serving as a scaffolding system. For the mechanical stability of tissue, cell-ECM adhesions are just as important as cell-cell contacts. The interactions between cells in vivo are in fact orchestrated by a number of factors; not only intercellular signaling pathways, but also the surrounding microenvironment with its mechanical cues are determinants of tissue function, proliferation, differentiation and, in essence, survival [3].
When interested in understanding the mechanics of such complex systems, it becomes necessary to decompose them into their fundamental building blocks and, if possible, to follow a bottom-up approach. This is the rationale leading the upcoming introduction: in a first step (Section 1.1), we will present a single cell system (*epidermal keratinocytes*) for which the mechanical role of the cytoskeleton is especially interesting to assess.
Keratinocytes will successively be analyzed on the multicellular level to understand the impact of cell-cell adhesions on the overall mechanical behavior of 2D cellular clusters.
In the second part (Section 1.2), we will present an artificial tissue system (i.e. *in vitro breast gland acini*) bringing us one step up on the hierarchical level: the introduced epithelial cells, in fact, can build 3D cellular spheroids surrounded by a condensed layer

of ECM-proteins, whose mechanical properties, as we will see, are especially relevant to decipher in a context of breast cancer research.

1.1. Getting support from within: the cellular cytoskeleton and its keratins

1.1.1. The cellular cytoskeleton

Since the discovery, in 1942, that the mechanism of muscular contraction is due to the interaction of actin and myosin chains [4], it has become clear that most cells owe their structural and mechanical integrity to a vast network of protein polymers spanning their interior, collectively known as *cytoskeleton*.
This intricate and highly dynamic system performs a variety of functions crucial for cell survival and reproduction: it spatially organizes organelles and cytoplasmic content; it generates the forces necessary for locomotion and shape rearrangement; and it physically and biochemically connects the interior of the cell to its external environment, be it via focal adhesions anchoring it to the ECM or via cell-cell contacts, which are ubiquitously present in tissue [2].
An incredible complexity accompanies these phenomena; only acting synergistically with a multitude of cytoplasmic proteins and organelles can the cytoskeleton perform its functions. And yet its fundamental building blocks are comparatively simple and well characterized: the typical cytoskeletal organization of an epithelial cell is depicted in Figure 1.1. Three main classes of protein polymers form this very dynamic "backbone" of eukaryotic cells: *microfilaments*, made of actin, *microtubules*, made of tubulin, and *intermediate filaments*, a broader class whose composition can differ with cell type [2].

- *Microfilaments* are semiflexible linear polymers formed by two helical coiled structures composed of globular (G-) actin subunits. Their typical diameter is of about 6 nm. When the concentration of G-actin proteins in pool is higher than a certain critical concentration C_c (defined as K_+/K_-, with K_+ and K_- the association and dissociation rates, respectively), then a monomer will bind to the filament. When the concentration is lower than C_c, on the other hand, a monomer will dissociate. Given that filaments are polar, the critical concentration is different for the (+) and the (-) end, implying that a preferential growth direction is present [6]. A multitude of regulatory proteins helps cross-linking, capping, severing and depolymerizing of the filaments, thereby continuously dynamically reshaping the actin network. Microfilaments play a fundamental role in cell locomotion, forming the

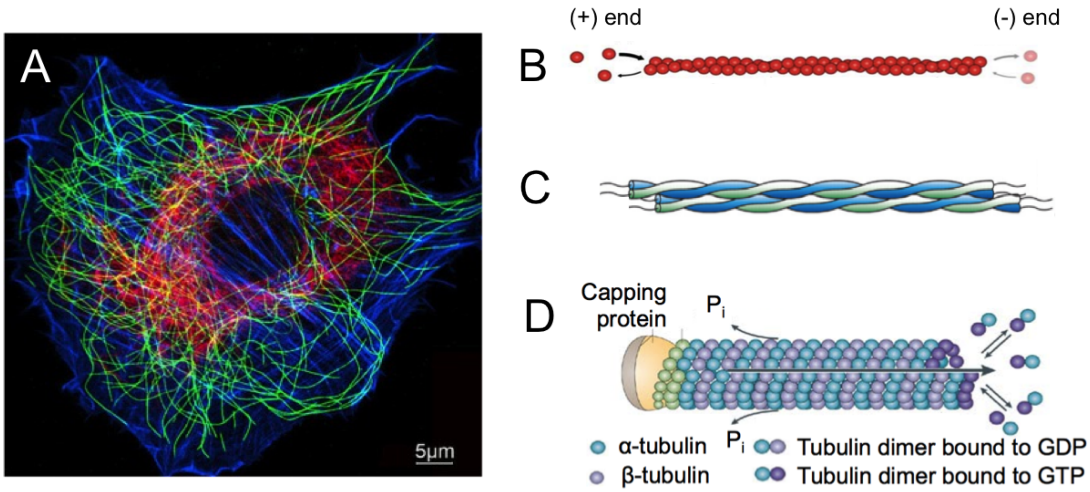

Figure 1.1.: A. Immunofluorescence staining depicting the three different components of the cellular cytoskeleton. In blue: microfilaments; in green: microtubules and in red: intermediate filaments (IFs). **B.** Structure of an actin filament, with the (+) and (-) end denoting polymerization and depolymerization directions, respectively. **C.** Basic structure of an IF and (**D**) of a microtubule. Adapted from [5].

very fine network present in lamellipodia and filopodia, but are also essential for cell adhesion, through the anchoring of much thicker actin stress fibers to focal adhesions [1].

- *Microtubules*, in contrast, are rigid hollow tubes with an outer diameter of about 24 nm and a length that can go up to 50 µm; they are most typically found as single fibers. Microtubules are composed of dimers of two proteins, α- and β-tubulin, which polymerize end-to-end into linear protofilaments that then associate laterally into the final cylindrical structures. Due to their high tensile strength and bending rigidity, microtubules are involved in chromosome separation during mitosis and meiosis (they are a fundamental constituent of the mitotic spindle) and can even drive the protrusion of bacteria and sperm by forming up the interior of cilia and flagella [7]. They periodically undergo depolymerization catastrophe events due to the dynamic instability of their ends [8] and are associated with intracellular transport and organelle positioning.

- Finally, *intermediate filaments* (IFs) are a heterogeneous class of biopolymers sharing, rather than protein content, the fundamental structure of their building blocks. Unlike actin filaments and microtubules, in fact, IFs are formed by rod-shaped subunits that self-assemble into parallel coiled coil dimers in the absence of ATP. Such

non-polar subunits associate laterally into antiparallel tetramers which then bind head-to-tail into protofilaments; two protofilaments assemble longitudinally into a protofibril, and four protofibrils finally build up a filament, in an increasingly hierarchical structure (see Fig. 1.3). At least 74 functional IF proteins have been identified so far, encoded by 71 genes [9]. This large variety can be roughly subdivided into five sequence homology classes: the *lamin* family (type V), mainly expressed in the nuclear envelope; the *neurofilament* family (type IV), present in neurons and neuroepithelial stem cells; the *vimentin* family (also comprising desmin and peripherin), whose proteins are expressed in fibroblasts, smooth muscle cells, white blood cells and astrocytes; and finally the *keratin* families (type I and II), expressed in epithelial cells, hair and nails. The two types differ in aminoacid content of the proteins, size and isoelectric point, the first one exhibiting a more acidic character (type I keratins) and the second one a more basic one (type II keratins) [2].
The main IF proteins, along with their homology classes, tissue distribution and assembly groups, are presented in Figure 1.2.

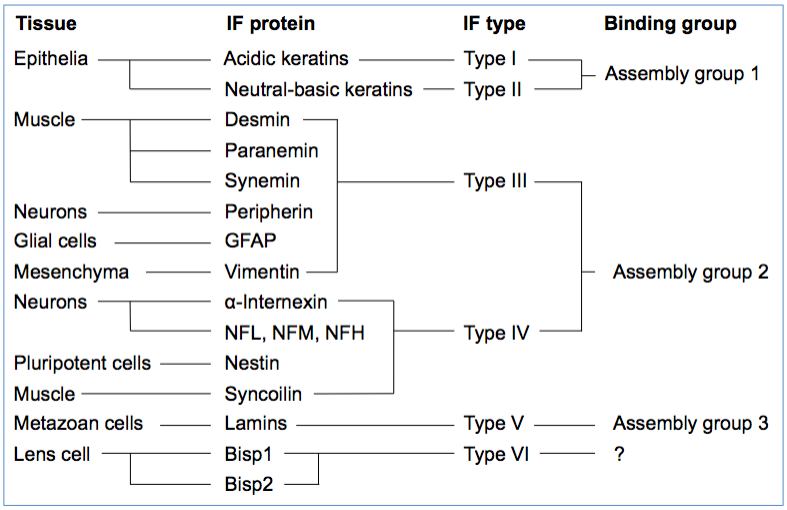

Figure 1.2.: Different homology classes of cytoskeletal IF proteins and their distribution in tissue. NFL, NFM and NFH stand for low-, middle-, and high-molecular weight neurofilament subunits, respectively. Type VI IFs form highly specialized filaments only found in the lens of the eye. The assembly groups are subdivided according to the ability of the IF proteins to copolymerize. Source: [10].

1.1.2. Keratin filament structure

More than 50 different genes encode for keratins, which are therefore the largest subgroup of IF network proteins. The structure of keratin filaments mirrors that of all other IFs. One important characteristic, though, is the fact that the initial dimerization can only take place between members of different types: one acidic keratin (type I) needs a basic binding partner (type II) in order to form a functional heterodimer (see Fig. 1.3).

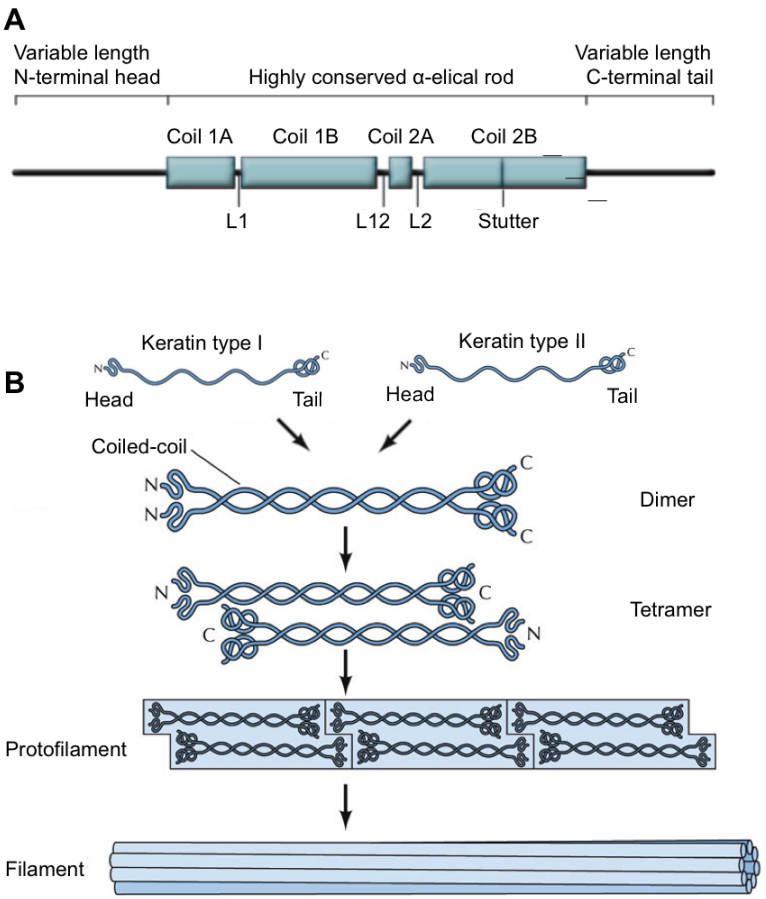

Figure 1.3.: A. Tripartite structure general to all IF proteins: a highly conserved α-helical central rod domain is flanked by a variable N-terminal head and a C-terminal tail domain. **B.** Schematization of the hierarchical structure of keratin IFs. Upon dimerization of an acidic keratin with a basic binding partner, the unit building blocks of filaments are formed.

In virtually all keratin proteins the secondary structure is pretty well conserved: surrounding a central, highly conserved α-helical subdomain are two globular units (the so

called head and tail domains), which can vary in length, sequence and structure (see Fig. 1.3). The central rod consists of four subdomains (1A, 1B, 2A, 2B) divided by three linker sequences (L1, L12, L2). The subdomains show heptad repeats, with the 1^{st} and 4^{th} position occupied by hydrophobic aminoacids [11]. The individual keratin protein expression levels are highly tissue specific: keratins K31-40, for instance (type I) are mostly present in hair and nails, together with K81-86 (Type II). K9-28 (type I) and K1-8 (type II), as well as K71-74 (type II) are to be found in epithelial tissues [12].

1.1.3. Skin and epidermal keratinocytes

As fundamental component of epidermal tissues, and a key player in wound healing processes, keratin is crucial for the stability and functioning of the skin. Skin, the largest organ present in most vertebrates, covers about 2 m^2 in the human body, with a thickness spanning from 1 to 4 mm. By protecting the underlying tissue from external damage, it constitutes the first and main barrier against pathogens, chemicals and mechanical stress. Histologically, it is subdivided into three layers.

- The deepest one, the *hypodermis* (or subcutaneous tissue), is composed of fibroblasts, macrophages and adipose cells and is mainly used as a fat storage [13].
- The *dermis* consists of irregular connective tissue and is host to blood vessels, sweat glands, hair follicles, and the mechanoreceptors providing the sense of touch.
- Finally, the *epidermis*, the most superficial layer, besides serving as a first natural mechanical barrier against external agents, is an immunologically active tissue and protects deeper tissue against UV radiation. It regulates the amount of water released from the body through transepidermal water loss [14], and keeps the electrolytes in balance [15].

This final layer is constituted for about 90% by *keratinocytes*, epithelial cells owing their name to the dense networks of keratin bundles present in their cytoskeleton. The constant regeneration and wound healing processes that make skin the highly dynamic tissue we know it to be start precisely from here.
Different types of keratinocytes build up the various layers of the epidermis, whose structure is presented in Figure 1.4: the production of new cells is ensured in the *stratum basale*, where epidermal keratinocytes originate from mitotic divisions of stem cells. From there, cells slowly start migrating towards the skin surface while undergoing a process called *cornification*, a set of morphological and biochemical transformations which

ultimately lead to cellular death. In the stratum basale, cells are packed regularly, cubical in shape and aligned perpendicular to the basement membrane (to which they are anchored via hemidesmosomes).
In the next layer, the *stratum spinosum*, the differentiation process already begins, with modifications in the keratin network that now expresses the keratin pair K1/K10 instead of K5/K14. The network then changes again as keratohyalin granules, filled with histidine- and cystine-rich proteins that bind keratin filaments together, are formed in the *stratum granulosum*. Cells at this point appear flattened and parallel to the skin surface.
Finally, when reaching the *stratum corneum* (what we commonly recognize as skin) functional keratinocytes have been replaced by corneocytes, dead cells devoid of nuclei and organelles and mostly constituted of a dense filamentous keratin matrix and of cross-linked proteins. The whole process lasts about 30 days [13].

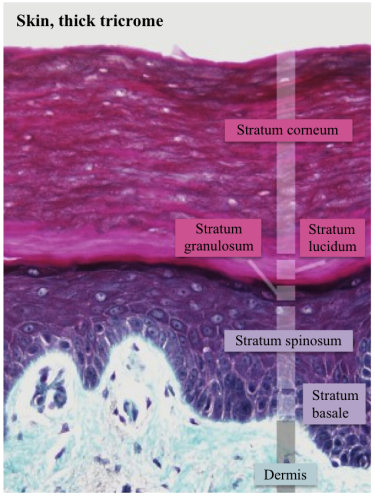

Figure 1.4: Thick trichrome (histologic image) of human epidermis, showing the layered structure of skin. Adapted from [16].

1.1.4. Desmosomes: cell-cell contacts connecting the IF networks

The most important cell-cell contacts between keratinocytes are *desmosomes*, junctional complexes localized on the lateral sides of plasma membranes. The interesting feature of these structures is that they allow direct anchoring of the keratin filaments to the plasma membrane via linker proteins like plakophilin and desmoplakin. The large multi-protein complex thus formed is also known as desmosome-intermediate filament complex (DIFC). Spanning the plasma membrane we find desmosomal cadherins, whose C-terminal domains are localized in the plaque and whose N-terminal domains instead are found in the intercellular space, where they couple the two halves of the desmosome

together [17]. A plethora of other proteins are associated to desmosomes, but the most important ones for the anchoring function are desmoplakin, plakoglobin and at least one isoform each of plakophilin and the desmosomal cadherins desmocollin and desmoglein [18].

Despite the rather large intercellular gap spanned by desmosomes (about 34 nm, as indicated by cryo-electron microscopy data [19]), these are incredibly robust cellular adhesion complexes, mostly expressed in highly mechanically stressed tissues such as skin and cardiac muscle. Desmosomes are often referred to as being *hyper-adhesive*, to indicate that they serve as a crucial scaffolding *coupling* mechanism in multicellular systems. In order to resist the shear forces it continuously experiences, epithelial tissue needs very stable cell-cell connections. It should therefore not come as a surprise to know that failure of the desmosomal connections can have pathological consequences as severe as those caused by keratin defects [20]. A schematics of the structure of a DIFC is presented in Figure 1.5.

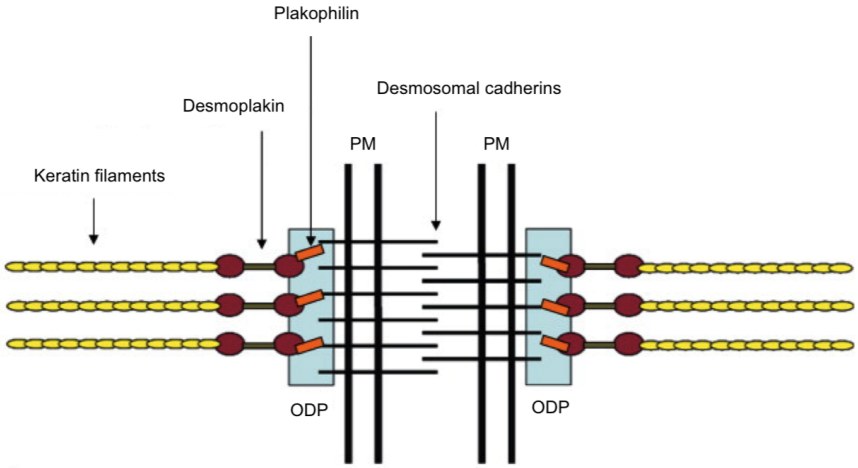

Figure 1.5.: Structure of a desmosome-intermediate filament junctional complex. PM: plasma membrane. ODP: outer dense plaque. The interaction between desmoplakin and the protein complex within the ODP is not yet fully understood, although it is hypothesized that plakophilin might serve as an intermediary connection. Adapted from [17].

1.1.5. The role and function of keratin

In the stratum basale, keratin can constitute up to 85% of the cellular protein content [11]. Such an enormous quantity must indicate a crucial function of this protein for the correct functioning and maintenance of homeostasis in keratinocytes. On a tissue level, it is well known that keratin provides strength and rigidity, but at the same time the single filaments remain extremely flexible and resilient: they can reach extensions of more than 2.5-fold in vitro [21] whereas single keratinocytes can be stretched up to 133% without breaking down or losing filament's structure and functionality [22].
Keratin networks are highly dynamic: time-lapse imaging of cultured monolayers show perpetual cycles of filament assembly and disassembly, starting from the nucleation of keratin speckles at the cell periphery. After elongation and a progressive translocation toward the nucleus (which is densely surrounded by the keratin network) they are eventually integrated into the existing filaments [23]. Some of these will be disassembled into soluble oligomers that diffuse throughout the cytoplasm, others will become integral part of the network and possibly even bind to desmosomes.
The disruption of a functional keratin network can have dramatic consequences: even point mutations in the genes encoding single keratin proteins can cause terrible blistering skin diseases (like *epidermolysis bullosa simplex* or *pachyonychia congenita*), which induce cellular fragility, damage, and constant blistering of the epidermis [24].
But many IF-related diseases are not just associated with a defect in mechanical functions: an example for this are laminopathies, a group of disorders resulting from mutations in the genes encoding nuclear lamins. Symptoms can go from muscular dystrophy to accelerated aging in children, and even appear as metabolic disturbances [10]. Such findings point at the involvement of IFs in a broader spectrum of functions.
Keratin filaments act as signaling organizers capable of sequestering and positioning signaling molecules, including developmentally active and fate-determining kinases. Therefore the keratin network has a broad range of regulatory functions, spanning from motility to organelle trafficking, from the organization of cytoplasmic architecture to the regulation of stress-activated enzymes. Filaments can even act as translation regulators [10] and are involved in modulation of the immune response. It is very well possible that many important functions of keratin IFs are still to be discovered.
Due to the lack of drugs allowing simple degradation of IF networks, and owing to the large redundancy in keratins protein expression, it has so far been hard to isolate their contribution to the most diverse functionalities they serve in cells.
For decades, the question of the role of keratin networks in determining *single* cellular

mechanics and stability has remained open. It is known that cornified tissue protects skin against external stress: but whether or not K5/K14 keratin networks present into basal layer keratinocytes also help conferring resistance to single cells, despite the highly flexible and extensible nature of the biopolymers forming it, was unclear. Our goal here is precisely that of determining the contribution of keratin to single cell stiffness, and to do so we performed examinations of cellular elasticity comparing normal and keratin-lacking cells.

1.1.6. Keratin-free keratinocytes

The generation of the first epithelial murine keratin-free kerartinocyte cell line is due to the efforts of the Translational Center for Regenerative Medicine (TRM) in Leipzig, guided by Prof. T.M. Magin [25]-[26]-[27]. Cre/Lox recombination technology was successfully applied to the deletion of the whole gene complex encoding for keratins of type I (acid). Keratins of type II (basic) are still expressed in the cell, but in absence of their natural binding partner these cannot dimerize and hence do not build a functional keratin network. The genetic tool system used to such end consists of a single enzyme, the Cre (cyclization) recombinase, which catalyzes the recombination of two short target sequences called loxP (*locus of X-over P1*), after the bacteriophage P1 from which the enzyme is derived. During enzymatic activity, the double stranded DNA sequence lying between the loxP sites is cleaved out as a circular product and successively simply degraded by the cell.
In brief, to produce keratin type I knock-out (KO) cells, C57B16 homozygote mice having two floxed (loxP-flanked) alleles of the keratin gene complex of type I where mated to 129S1hprt Cre mice. The resulting heterozygote offsprings were mated to each other to obtain keratin type I gene complex free mice. Keratinocytes were then isolated from the epidermis of E18.5 KO and wild-type (WT) mice and cultivated under conditions that lead to a spontaneous immortalization of the cells. Rescue cells (RES) re-expressing a keratin network were generated as a control through stable insertion of YFP-marked human keratin 14 (K14) cDNA in the KO cells via lentiviral vectors. Given that the basic keratins were left unaffected, in fact, the re-expression of the acidic K14 proteins was sufficient to restore the potential for heterodimerization with the basic binding partner K5. Similarly, keratin type II KO cells and the corresponding K5 RES keratinocytes were also produced.

1.2. Getting support from around: breast glands and basement membranes

So far our description has focused on the cellular cytoskeleton, its specific sub-classes, and the role they play in providing an internal scaffolding able to confer shape and stability to single cells. But, as we already anticipated, when analyzing multicellular aggregates or tissues it becomes clear that their mechanical stability largely relies also on other structures: besides the intrinsic differences in cellular stiffness, in fact, all kinds of "external" scaffoldings are present as well. A notable example is represented by basement membranes (BMs), thin, fibrous extra-cellular matrix (ECM) structures typically separating epithelial cell layers from connective tissue.

In this section we will introduce a specific type of multicellular structure which is also surrounded by a basement membrane, whose properties have so far been poorly characterized. The structure and importance of mammary breast glands is quickly outlined in the following section; and the role played by the BM surrounding it in determining its stability will be analyzed in the following chapters.

1.2.1. Human breast and mammary gland anatomy

The human breast is a highly dynamic organ whose development proceeds via a series of accurately timely-articulated phases: the neonatal stage for instance dramatically differs from the postpubertal or post-menopausal one, and full maturation in not reached until a woman experiences pregnancy and childbirth. Before that moment, the mammary glands undergo extensive micro- and macro-anatomical remodeling, but have the potential of regressing again to their resting state after cessation of lactation. Such a plasticity is induced by a finely-tuned hormonal regulation, with oestrogen, progesterone, prolactin and epidermal growth factor (amongst others) determining the physiological state of milk glands [28].

In their matured state, breasts are mostly composed of adipose and glandular tissue supported by a loose framework of fibrous connective tissue also known as Cooper's ligaments [29]. By providing its secretory function, mammary glands play a central role in contributing to the breast's functionality: they consist of elongated, ramified structures connecting the single functional units of the breast (the terminal-ductal lobular units, TDLU) to the nipple.

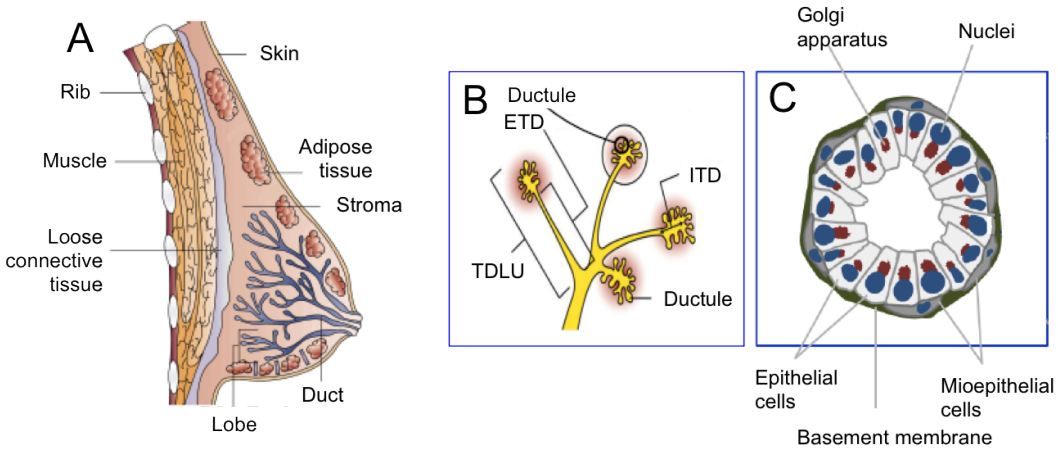

Figure 1.6.: Schematics of breast (**A**) and mammary glands (**B**) anatomy. Each milk duct terminates in bunches of ductal lobular units (TDLUs), structures composed of a layer of epithelial and myoepithelial cells enclosed by a basement membrane. ETD: extralobular terminal duct. ITD: interlobular terminal duct. **C.** Schematics of a single terminal ductule (plane cut). Note the baso-apical polarization of the inner layer of epithelial cells. Image courtesy of A. Gaiko-Shcherbak.

Typically, each of the 15 to 20 lobes are comprised of lobules containing about 10 to 100 alveoli (the effective milk secreting units).
These terminal acinar structures have a diameter of about 0.12 mm [29] and are formed of an outer layer of contractile myoepithelial cells enclosing one or more inner layers of epithelial cells (see Fig.1.6). With pregnancy, differentiation of the ducts results in the creation of luminal structures, and hence to the formation of a hollow space necessary for milk production and lactation. Surrounding the whole system is a basement membrane whose fundamental properties we will briefly review in the following.

1.2.2. Basement membrane structure and composition

As already anticipated, basement membranes are highly organized and condensed extracellular matrix protein layers secreted by epithelial cells and tightly bound to them via cell-extra cellular matrix adhesion complexes. They are mostly found adjacent to epithelium, endothelium, mesothelium, as well as around smooth and striated muscle cells, Schwann cells and adipocytes [30]. Their function and composition can be tissue specific and vary according to physiologic or patho-physiologic conditions [31], but their major constituents are typically the proteins collagen (most commonly isotype IV),

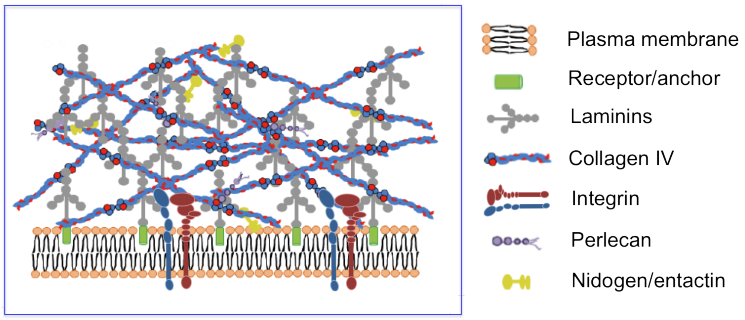

Figure 1.7: Schematic representation of breast gland's BM structure and composition: a dense network of collagen IV and laminin isoforms is stabilized by nidogen and perlecan, while anchoring to the plasma membrane is ensured by cell surface receptors like integrin. Adapted from [40].

laminin, nidogen (entactin) and the proteoglycan perlecan [32]. Both collagen IV and laminin individually self-assemble into suprastructures that are essential for network stability [30]. Structure, composition and biophysical properties of BMs can change in an age-dependent manner [33], and in some tissues display an asymmetric, side-specific organization [34]. Typically, BMs provide an anchoring site for epithelia thanks to the numerous cell-matrix adhesions that can develop between single cells and such a condensed ECM network; but they also regulate cellular motility and behavior, influencing signaling pathways that can lead to tissue remodeling in what is turning out to be a tight interplay between cells and their surrounding environment [3]-[35].
They also provide a first mechanical barrier against metastatic cancer cells, and in some tissues they act as highly selective semi-permeable membranes (notably, in the kidneys, where the glomerular BM helps performing the blood filtration function of the glomerulus, [36]-[37]).

The first ultrastructure study of a breast gland dates back to 1971 [38]. Now, we know that collagen IV and laminins (in the four isoforms present: laminin-111 (LM-1), -322 (LM-5), -511 (LM-10), and -521 (LM-11) [39]) are assembled in the Golgi apparatus and then secreted to the extracellular space, where they start organizing a network by binding to cell surface receptors (i.e., integrins) and creating a laminar structure in combination with collagen. This meshwork is then stabilized by nidogen and perlecan, that act as cross-linkers bridging the polymers together. A schematic representation of the structure of a breast gland basement membrane is given in Figure 1.7.

1.2.3. Force homeostasis in healthy tissue and during tumor invasion

Cancer is the common name given to a class of diseases characterized by acquired genetic mutations resulting in uncontrolled cell proliferation and pathological behavior. One of

the most dramatic modifications it causes concerns cellular motility: cancer cells, in fact, besides abnormally growing at a certain location, can invade adjacent tissues and spread through the body; this process, known as *metastatization*, is the leading cause of cancer deaths worldwide [41].
Normally, healthy cells possess a series of control mechanisms allowing to detect and correct for minor DNA mutations; the most important genetic sentinels are the so-called *tumor suppressor proteins*, which perform a series of functions spanning from repairing DNA or inducing apoptosis (the mechanism of programmed cell death), to regulating the cell's cycle. The set of alterations in cellular physiology a mutated cell needs to achieve in order to overcome such surveillance mechanisms include: an insensitivity to growth-inhibitory signals; the capacity to evade apoptosis; a limitless replicative potential; the capability to sustained angiogenesis; and finally the potential for tissue invasion [42].
Typically, cancer is caused by an interplay between genetic disorders and different risk factors. The same holds for the family of breast carcinomas, which are a large group of very heterogeneous subtypes: some are contained in the lining of the breast milk ducts (DCIS, or *ductal carcinomas in situ*), while others spread to the adjacent stroma (*invasive ductal carcinomas* and *metastatic carcinomas*). What they have in common, though, is the fact that nearly all of them arise in the same part of the breast, the terminal ductal-lobular units, where the first step tumor formation is the loss of epithelial polarization. Breast glands are therefore *the* hotspot for cancer formation, and understanding the interplay between malignant cells and the environment surrounding the ductules is of crucial importance.
As already mentioned, the basement membrane is the first barrier that invasive cells need to overcome in order to invade adjacent tissue: already since the 1980s, electron microscopy studies have shown that often invasive neoplasms are associated with BM interruptions [43]. Typically, this process starts with the attachment of cancer cells to the membrane (mediated by specific attachment factors like laminin); the matrix is then degraded by tumor-cell-associated proteases, like matrix metalloproteinases (MMPs); and finally, cell locomotion in the modified BM network can take place.
But the interaction between tumor cells and the ECM also proceeds in less direct fashions: in response to the presence of malignant cells, for instance, normal tissue can increase the production of matrix components by growing a dense fibrous tissue around the tumor (a process known as *desmoplastic response*). In carcinomas, the extent of BM components expression can sometimes be directly correlated with the degree of differentiation of malignant cells [44]. Interestingly, it has been observed that breast gland BMs

are integral to the polarity of luminal epithelial cells: in breast cancer, the absence of myoepithelial cells probably results in a lack of laminin-α chains which may contribute to loss of polarity of the malignant phenotype [45].
Another important hallmark of breast cancer is a series of changes in cellular rheology and tissue stiffness; the normal mammary gland is in fact a very mechanically active tissue, whose development and proper functioning crucially depend on tensional homeostasis. Together with hormonal and growth cues, the forces exerted by the surrounding microenvironment literally shape tissue architecture.
During lactation, for example, the luminal epithelial cells and the surrounding basement membrane undergo an outward compressive stress caused by the accumulation of milk in the luminar space, which is counterbalanced by a reciprocal resistance force exerted by the surrounding stroma (see Fig. 1.8 A).

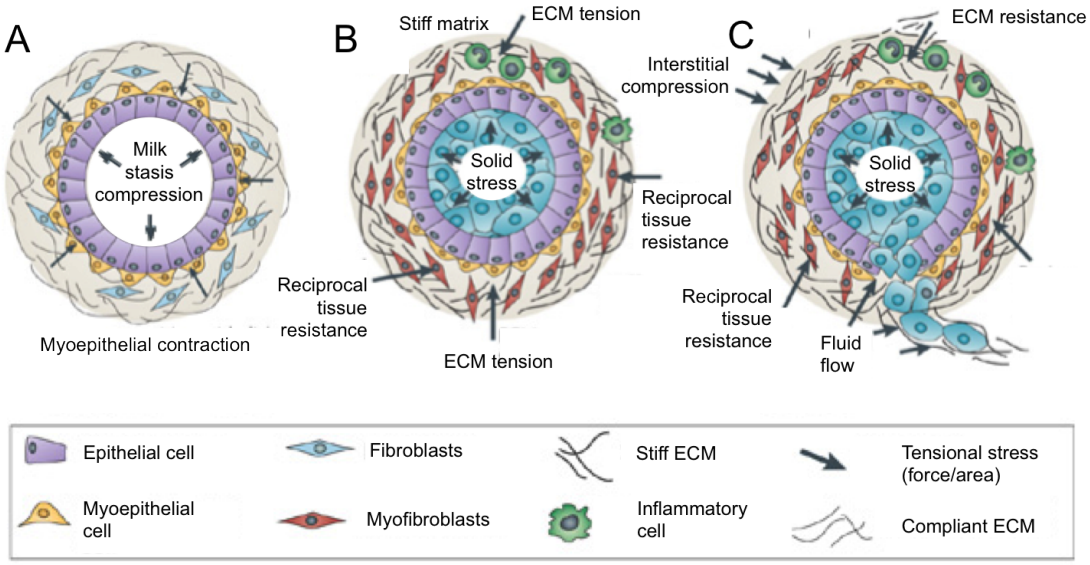

Figure 1.8.: Sketch showing normal tissue homeostasis in a healthy milk-secreting ductule (**A**) and its alteration in the pathological situation (**B**-**C**). Upon growth of a tumor mass within the luminar space, an increased tension is exerted upon the surrounding BM and connective tissue. Interstitial pressure grows (B) until the point in which the proliferating cancer cells manage to break through the ECM matrix and invade the nearby tissue (C). Drawing not to scale. Adapted from [46].

Upon suckling, oxytocin-stimulation makes the myoepithelial layer surrounding the epithelial cells contract, thereby inducing milk to flow out of the alveolar space [46]. In case of prolonged milk stasis, the continuous glandular distension eventually compromises the

integrity of the tight junctions present between luminal alveolar cells; this triggers an involution of the gland which consequently returns to the pre-lactating state.
In epithelial cancers, such a tensional homeostasis is completely altered (see Fig. 1.8 B-C): over time, the expanding tumor mass generates a higher outward compressive force as the number of myoepithelial cells surrounding it decreases; poor lymphatic drainage causes a build-up in interstitial pressure [47] and desmoplastic response induces matrix stiffening [48].
The altered material properties of the BM, together with the genetic modifications enhancing cellular motility and the disturbed tensional balance, is the result of a combination of factors eventually leading to a break-through of cancer cells into the connective tissue.

1.2.4. Epithelial cell lines and 3D cultures

For decades, the use of immortalized cell lines as culture systems has allowed researchers to unravel the complexities of signaling pathways and molecular mechanisms determining the fate of the most diverse cell types: such in vitro systems, easy to handle and characterized by limitless proliferation, are excellent tools to decipher cellular behavior under physiological as well as pathological conditions. The incredible variety of currently existent cell lines (more than 100 only deriving from human breast cancers are commercially available) offers great potential in this direction.
Traditional cell culture systems, though, are two-dimensional (2D), meaning that cells tend to grow as a flat monolayer when cultured under standard laboratory conditions. In vivo, the situation is very different: not only do tissues organize in complex architectures which are not really well represented by cell cultures, but a body of research suggests that most cell types behave very differently when they are embedded in tissue compared to when they are isolated from it [49]. Adhesion and locomotion properties, differentiation and proliferation rates, as well as force modulation and tissue organization are in fact tightly regulated by extracellular signals which are dramatically altered in artificial growth conditions. An important regulatory factor, in this regard, is the extracellular matrix; besides providing mechanical support and anchoring sites, this protein-based milieu helps regulating intercellular communication and segregating tissues form one another. The lack of ECM in 2D cultures imposes limitation to the amount of information that can be won by studying such traditional cell culture systems.

In recent years, the scientific community has undertaken significant efforts towards the development of more complex model systems: it suffices to think about the field of tissue engineering, now so advanced that it allows for the production of artificial cartilage or pulmonary arteries, but which did not even exist until the 1970s [50]. Also on a smaller scale (for instance when studying clusters of few dozens of cells), there is a growing understanding that the real determinants in multicellular behavior are not only chemical and biochemical signaling cascades, as traditionally postulated by classic cellular biology, but rather lie in a complex interplay between chemical, electrical and mechanical cues. The importance of forces and pressures in shaping tissues during morphogenesis, for instance, or the discovery of substrate-stiffness dependent stem cells differentiation [51] have opened the way to understanding the fundamental role played by mechanics in biology. Therefore, especially when studying a mechanically active tissue like the breast, three-dimensional cell cultures are much better approximations of the in vivo situation than flat monolayers.

Thanks to the pioneering work of J. Debnath, S. Muthuswamy and J. Brugge, today we come one step closer to realistically modeling a breast gland in vitro. In 2003, the first protocol for growing three-dimensional (3D) cellular spheroid model systems derived from human breast epithelia was published [52], and since then has been a powerful tool to investigate mammary morphogenesis and cancer development in a biologically relevant context. Given the dramatic incidence of breast carcinoma (it is the most common female cancer in the Western world and the leading cause of cancer deaths worldwide [41]), the use of 3D models for understanding the biology of healthy and pathological situations is of course of prime importance. So far, 3D breast cellular systems have lead to a better comprehension of the mechanisms leading to the formation and maintenance of a hollow glandular lumen [53] as well as the regulation of apicobasal polarity; they allowed to understand that cell-cell and cell-matrix adhesion pathways can interfere with the phenotypic expression of the tumorigenic state; and finally, they served as a basis to start deciphering the importance of tensional forces in driving 3D tissue architecture [46].
The key to growing three-dimensional cell structures in vitro lies in the mimicking of their in vivo environment. When seeded on hard plastic cell culture flasks, epithelial breast cells just form a flat 2D layer; but if they are cultivated on reconstituted basement membrane gels, they spontaneously start the differentiation and polarization process that will turn them into spherical structures resembling individual breast gland ductules. To this end, the most commonly used substrate is a gel-like assembly of ECM

proteins and growth factors extracted from Engelberth-Holm Swarm (EHS) mouse sarcoma, commercially available under the brand names of Matrigel or GelTrex.
Different cell lines, corresponding to different invasiveness levels, are available and can be grown under such conditions. A healthy breast acinar ductule is best approximated by an MCF10A spheroid, a structure derived from a non-tumorigenic human mammary epithelial cell line. The structure and maturation process of an MCF10A acinus are outlined in Figure 1.9.

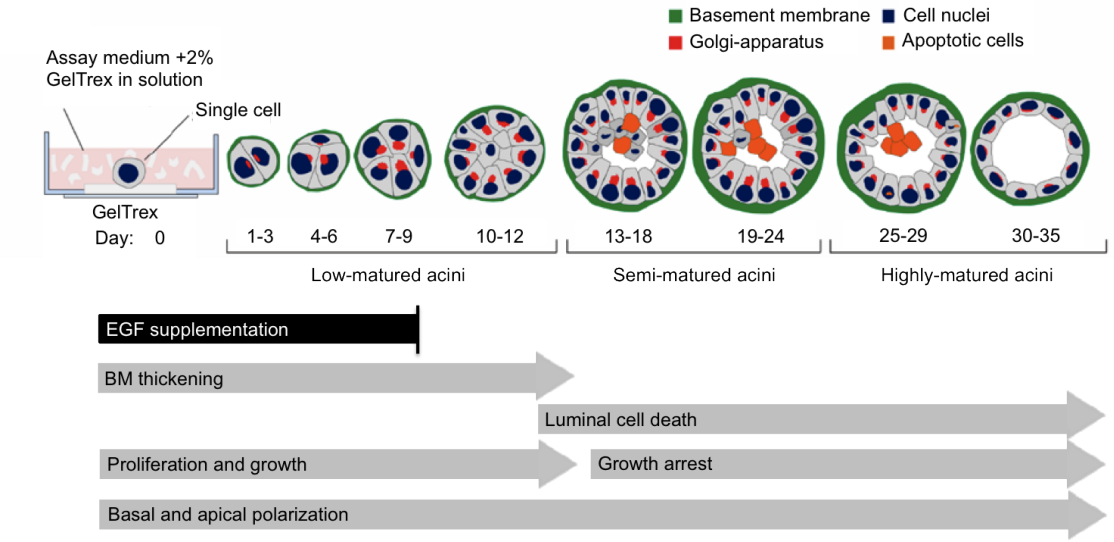

Figure 1.9.: Sketch representing the indicative in vitro maturation stages of 3D MCF10A acini seeded on an EHS matrix substrate (GelTrex). Three main developmental phases can be identified, according to parameters like cell proliferation, baso-apical polarization, BM growth and lumen formation. Carefully tuned EGF supplementation is crucial to the establishment of a reproducible cell culture protocol. Adapted from [54].

After seeding on an EHS matrix substrate, single cells have to be held in culture for a period of approximately 30-35 days before full development can be achieved. A fine tuning of media composition is absolutely mandatory in order to obtain spheroids displaying all the most physiologically relevant characteristics: namely, apico-basal polarization, basement membrane secretion and lumen formation. Especially the latter has been found to be highly sensitive on EGF supplementation [54].

During development, three stages can be roughly identified. The first 10-13 days are characterized by high rates of proliferation: spheres grow in size and start producing a basement membrane, both by secretion of collagen and laminins and by recruiting of

growth factors and other macromolecules from the ECM-like gel. We will call spheres in this age group "low-matured acini". Polarization of the cells starts almost immediately, and eventually leads to the positioning of nuclei on the basal and the Golgi-apparati on the apical side. After this initial phase, the growth arrests and the inner cells start undergoing apoptosis: this process goes on for about 7-10 days and corresponds to an intermediate degree of maturation ("semi-matured acini"). The process of programmed cell death has the purpose of clearing out luminal space and producing the hollow sphere sketched in the final image of Figure 1.9, which only starts appearing after about 25-30 days of culture (we will refer to this group as "highly-matured acini"). Typical acinar diameters can vary individually, but span 20-100 µm according to the maturation stage. Interestingly, this system allows to model the different stages that are found in vivo: hollow lumens are in fact only developed during pregnancy and lactation, while in the post-pubertal stage the ductules are filled with epithelial cells.
Other cell lines (like the tumorigenic MCF7 and the invasive MDA-MB-231) can also form 3D spheroidal structures when grown on EHS-substrates; but they completely lack the high level of organization displayed by MCF10A and they do not produce a basement membrane [55].

1.3. Motivation and aim of this work

As introduced in this chapter, this work focused on the analysis of two different cellular systems, murine epidermal keratinocytes on the one hand (both as single cells or as monolayers) and human breast epithelial 3D spheroids on the other hand.
While a hierarchical analysis encompassing the study of single cell, cell-cell and 3D cellular architectures would have ideally been conducted on a single biological system, the relevance of these particular cellular cultures at specific levels of tissue organization is such that we decided to analyze them separately. Nonetheless, on an abstract level we tried to reach a comprehensive view of the different factors that can impact the mechanical properties of epithelial tissue. In the following we shall briefly discuss the relevance of the two cellular cultures used and the rationale of this thesis.

It is well-known that point mutations in keratin-encoding genes are the cause of severe diseases that include, but are not limited to, skin fragility and severe blistering problems [24]; and yet the impact of keratin on the mechanical properties of epithelial keratinocytes had so far not been fully clarified.
When thinking about the skin it is clear that it offers a barrier function; the epidermis, though, is subdivided into a rich variety of layers, differentiating themselves not only in function and composition but also in keratin content. The part of the epidermis we are used to considering as skin (namely, its outer layer) is actually composed of dead cells which have undergone cornification, a set of morphological and biochemical transformations resulting in cellular stiffening, nuclear degradation, and profound alterations in the keratin network: basically, keratins become enclosed within an insoluble amalgam of other proteins, crosslinked by transglutaminases and surrounded by a lipid envelope [56]. The cells used in this work instead are isolated from the stratum basale, the deepest layer of the epidermis, where keratinocytes are first produced from mitotic divisions of stem cells [13]: here, the role of keratin was not completely clarified yet.
Isolated keratin networks have in fact proved to be extremely resilient [21], and cells expressing them very stretchable [22], but a comprehensive analysis of the impact of keratin networks on the stiffness of such cells had been missing so far.
This was due to a number of difficulties: firstly, the absence of drugs able to simply depolymerize the intermediate filaments cytoskeleton [57] impeded so far to have easy access to completely keratin-free cells. Secondarily, the high genetic redundancy of keratin (with over 50 different genes encoding for different isotypes of this protein [12]) is such that deletion of single genes encoding it is not enough to destroy the polymer net-

works. Thanks to the Translational Center for Regenerative Medicine (Leipzig), though, today we have access to keratinocytes completely lacking intermediate filaments.

The goals of the first part of this thesis are therefore the following:

- Characterizing the mechanical properties of wild-type and knock-out keratinocytes, and by doing so understanding the role played by keratin networks in determining the cellular mechanical response on the single cell level.
- Bridging the gap to the multicellular level by analyzing differences in the mechanical response of wild type and knock-out keratinocytes monolayers in order to assess potential differences arising when tissue architecture becomes more resembling the in vivo situation.

In the second part of this work, a more complex model system was analyzed, namely MCF10A spheroids. These highly organized, three-dimensional cell culture systems mimic the fundamental units of a breast gland, and represent a precious tool in a wide range of research applications. In vivo, the breast gland is a hotspot for cancer formation and invasion, and is a very mechanically active tissue [29].
It is ubiquitously surrounded by a basement membrane (BM) that probably acts as a mechanical barrier, and potentially as a size-selective filter for various macromolecules. The characterization of such permeation properties would be highly relevant in a context of drug delivery, in order for example to understand whether specific chemotherapeutic agents could penetrate the BM and reach cancer cells, and yet no single study is present in literature investigating this aspect. Similarly, since the establishment of this cell culture model, little or no effort has been dedicated to the study of its mechanical properties, despite the fundamental importance that forces and pressures exert in maintaining the functional homeostasis of the breast gland; one notable exception is the work of G. Venugopalan, D. Camarillo and coworkers, who analyzed the mechanical differences between single MCF10A cells and 3D spheroids and simulated the viscous creep response of fluid-filled hollow spheres by modeling the material as a standard linear solid model [58]. Their work though completely neglected the presence of the basement membrane, whose impact we expected to be of relevance in determining the architecture, and hence the material response, of MCF10A acini.

Our goal here is therefore that of characterizing the mechanical and permeation properties of basement membrane-enclosed MCF10A acini: given the much higher structural

complexity that such spheroids display when compared to single cells, though, such an analysis has been subdivided in various parts, namely:

- Characterizing the permeation properties of the basement membrane surrounding breast glands acini.
- Characterizing morphology, structure and mechanical properties of isolated basement membranes and their importance for the structural stability of cellular spheroids.
- Comparing the different developmental stages of 3D MCF10A cultures and quantifying their resistance against externally applied mechanical stress.
- Finding an appropriate material model for describing such a complex, non-linear, viscoelastic material.

2. Theoretical foundations

2.1. AFM as a tool to measure cellular elasticity

The birth of SPM (Scanning Probe Microscopy) during the 1980s boosted enormously the possibilities of research in the field of biophysics. Images of surfaces having unprecedented resolution (even beyond that of optical diffraction of light) could suddenly be obtained by making physical probes interact with the samples. Scanning tunneling microscopy, for instance, exploiting the principle of quantum tunneling of electrons, allowed to image surfaces at the atomic level. Atomic force microscopy (AFM), developed shortly afterwards (it was invented by Gerd Binnig, Calvin Quate and Christoph Gerber in 1986, [171]), quickly established itself as one of the leading techniques for imaging, measuring, and manipulating matter at the nanoscale. The flexibility of operation of this instrument and the experimental possibilities it opens are wide, and of large interest to surface physicists, material scientists and biologists, amongst others. An AFM can in fact be used for the analysis of very different samples (organic or inorganic, analyzed in air or liquid, characterized by different physical properties, stiffness, chemical composition and so on), and is therefore a precious and versatile tool particularly suited for interdisciplinary research.

2.1.1. Principle of operation and setup

The core of an atomic force microscope is to be found in a microfabricated cantilever just a few hundred micrometer long (typically made of silicon or silicon nitride) ending in a tip that can have different geometries. The cantilever support chip can be moved along the z direction by means of a piezoelectric actuator, and the tip position is followed via the optical lever method: a laser beam aligned on the back of the cantilever is reflected into a quadrant photodiode, allowing for a very precise mapping of the vertical position of the tip.
A schematics of a typical AFM setup is given in Figure 2.1.

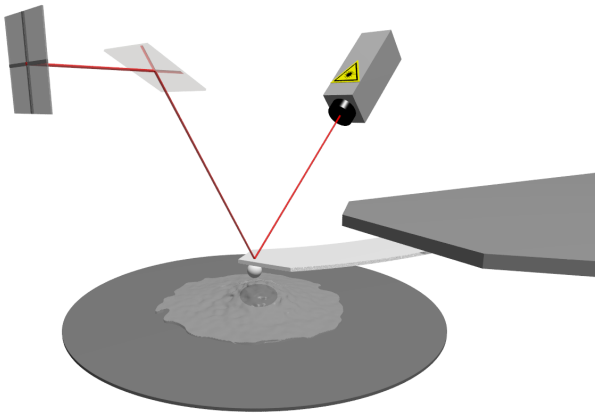

Figure 2.1.: Schematics of the AFM working principle: the laser beam reflected on the back of a microfabricated cantilever is guided into a quadrant photodiode allowing to measure the z-position of the tip with great accuracy. The cantilever sketched here is used as an indenter pressing on a cell. Adapted from [189].

When interacting with a surface, the cantilever deflects in a way that depends on the forces acting between tip and sample. The dependence of interatomic forces on distance can be empirically modeled via the Lennard-Jones potential [95]:

$$U_{LJ}(r) = 4\epsilon\Big[\Big(\frac{\sigma}{r}\Big)^{12} - \Big(\frac{\sigma}{r}\Big)^{6}\Big] \tag{2.1}$$

where r is the distance between particles, ϵ the depth of the potential well and σ the distance at which the interparticle potential vanishes ($U_{LJ}(\sigma) = 0$). A few angstroms away from the sample's surface, the interaction is repulsive: Pauli's principle forbids the overlap of the electronic orbitals of substrate and tip. Such short-range repulsive interaction is mathematically described by the term r^{-12} (see Fig. 2.2). With growing distances (up to hundreds of angstroms), the Van der Waals forces become predominant, and cause a long-range attractive interaction approximated by the term r^{-6} [94]. Once the separation between substrate and tip becomes too large, the intermolecular forces simply fade away and are not sensed anymore. The tip therefore deflects according to the distance from the sample's surface.

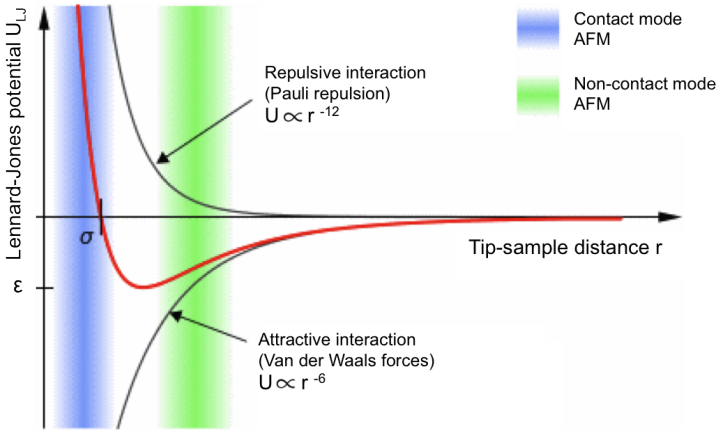

Figure 2.2: Red line: Lennard-Jones potential $U_{LJ}(r)$ describing interatomic forces as a function of distance. Green and blue shaded areas: ranges corresponding to the different AFM imaging modes. Black lines: attractive and repulsive terms of the potential. ϵ: potential well depth. σ: distance of vanishing interparticle potential. Source: [170].

This deflection is modeled as perfectly elastic. Hooke's law therefore correlates force and spatial information, and if the spring constant k of the cantilever is known, the maximal tip-sample adhesion force can be calculated by:

$$F = -k\Delta d \tag{2.2}$$

with Δd the displacement signal measured by the photodetector.
Based on this fundamental functioning principle, the AFM can be used for a number of different applications, according to the range of forces and substrate properties one wants to investigate. Let's briefly describe the main working modes relevant for this thesis.

2.1.2. Imaging modes

One of the main applications of AFMs lies in the recording of images having a spatial resolution in the order of the nanometer: by raster scanning the tip across a surface, the information on the z-position of the tip collected by the photodetector allows a line-by-line reconstruction of a specimen's topography. In this case, two different mechanisms for image capture are possible, according to which feedback loop system is used to tune and control the distance between sample and tip.
In the first case, while the tip is raster-scanned across the substrate's surface, its distance from the sample is held constant. By recording the cantilever's vertical deflection (via the laser's spot displacement on the photodiode quadrants) one obtains a direct information of the sample's height. The single line scans are then mapped together to

recreate a 3D topographical image. This modality is known as *contact mode*.
Note that in this case the image resolution will strongly depend on the tip's aspect ratio. The line profiles resulting from each scan will in fact always carry a certain degree of information on the tip's geometry (an effect known as *tip convolution*).
This is why the tip sharpness should be chosen according to the sample to analyze. Typical values for the nominal radius of curvature of standard tips span 8-10 nm, but for the imaging of very fine structures ultrasharp tips going down to radii of curvature of 2 nm might be favored [135]. Usually, provided that the tip's geometry is well-characterized, one can correct for the tip convolution effect at least to some extent; but in the worse cases, if the tip is broken or damaged, this will become so pronounced as to prevent proper measurements.

In the second imaging mode, known as *tapping* or *intermittent-contact* mode, the cantilever vibrates at its resonance frequency while scanning the surface. This time it is the oscillation amplitude that is held constant by the piezoactuator feedback loop. While "tapping" the sample, in fact, the cantilever's vibration will be modified by contact with the surface: when passing over a protruding feature, the amplitude will be dampened, when scanning a valley it will be enhanced. This change is reflected in the deflection amplitude of the laser beam, that eventually leads to a height mapping of the substrate. The main advantage offered by this imaging mode lies in the lower interaction of the tip with the sample, which therefore minimizes the risk of scratching or damaging of surface features. Friction disappears, and dragging of soft substrates is avoided. Another interesting feature is the possibility of extrapolating additional information by recording the phase lag of the cantilever oscillation relative to the signal sent to the cantilever's piezo driver. This lag is in fact very sensitive to variations in the sample's material properties, and can therefore provide a complementary mapping of the sample according to its rigidity and adhesion: this is the so called *phase image*.
In any case, once a reliable topographical image is obtained, parameters like the root mean squared roughness ($\mathrm{RMS_{rough}}$) can be computed from the standard deviation of the height (z) data:

$$RMS_{rough} = \sqrt{\frac{1}{N}\sum_{i=1}^{N}(z_i - \bar{z})^2} \tag{2.3}$$

In the formula, N is the number of pixels measured in the scanned area, z_i is the height of point i and $\bar{z}$ the average over all the z_i values.

2.1.3. Force spectroscopy

In force spectroscopy experiments, the cantilever is not scanned across the sample's surface but is driven up and down on a specific x- and y-position on the sample while its deformation is recorded by the photodiode. The result is a force-distance curve displaying the cantilever deflection against the z-position of the piezoelectric driver. A typical approach and retraction cycle performed on a soft substrate is shown in Figure 2.3: the tip is lowered (a) to a distance at which it enters in contact with the surface (b), where a certain user-defined load is exerted (c). The tip is then driven upwards, but its retraction is obstructed by the adhesive interactions with the substrate (d) until the pulling force is high enough to overcome them (a). At this point, the tip detaches and can be retracted.

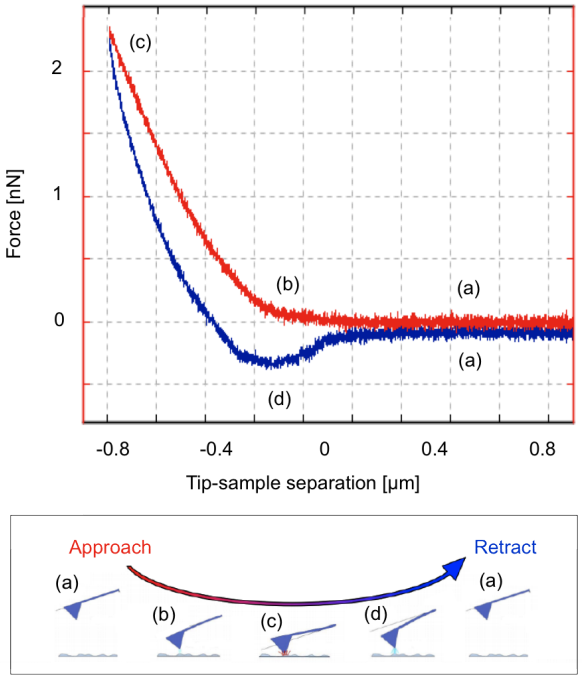

Figure 2.3: Force-distance curve recorded on a live cell via AFM force spectroscopy. In red: approach curve. In blue: retraction curve. The indentation cycle starts with lowering of the cantilever (a) until the tip snaps in contact with the surface (b). After a certain indentation force has been reached (c), the tip is retracted. Once the adhesive interaction with the substrate (d) has been overcome, the tip snaps out of contact and goes back to the initial position (a).

After the initial contact between tip and sample, pressing the cantilever like depicted in (c) will of course have the effect of bending it. On hard surfaces, the relation between cantilever deflection and force exerted is purely linear (and is given by Equation 2.2). But on soft substrates, the tip can slightly sink into the material without bending before a deflection can be measured by the photodiode. The resulting force-distance curve will not be perfectly straight, but will rather show a curvature, after the contact point, that is well depicted in Figure 2.3. In this case, one has to correct for this difference.

The effective indentation depth δ is taken to be the piezo-displacement z minus the cantilever deflection d:

$$\delta = z - d \tag{2.4}$$

The adhesive forces recorded upon retraction depend on the specific substrate composition and roughness (for instance, they can be very high for soft biological materials) but are also sensitive to factors like temperature and humidity. Under ambient conditions, in fact, capillary condensation can cause a thin water meniscus to form between the AFM tip and underlying hydrophilic substrates. Clearly, when working in liquid such non-specific interactions will be minimized [135].
Force spectroscopy experiments can be the source of precious information regarding the mechanical and elastic response of the analyzed samples. In this sense, the AFM literally works as a nano- (or micro-) indenter even capable of probing the material response of samples as small as single proteins [187].

2.2. The Hertz model

In order to extract material parameters from force-indentation curves, one must be able to model the contact mechanics problem of an indenter pressing onto the sample's surface. Obviously, cells are highly inhomogeneous, soft, viscoelastic materials which cannot be mechanically characterized with the ease we would expect from simpler linearly elastic objects such as crystals or elastomers. Talking about the elastic modulus of a cell, for instance, is per se an approximation that can only hold within a certain scale of observation and therefore range of measuring conditions.

Nonetheless, a number of simplified models have been developed over the years to try to quantitatively describe the mechanical properties of biological materials as assessed by means of AFM indentation. Some try to account for viscoelastic effects, for instance by approximating cells to combinations of springs and dashpots (good examples are the standard linear solid model or the Maxwell model [168]), others just describe biological materials as linear elastic objects. The simplest and most widely used in this sense is certainly the Hertz model: in its original formulation, it describes the contact between two smooth elastic spheres of homogeneous and isotropic material and demonstrates that the shape and size of the contact region vary with the deformation of the contacting bodies [182].

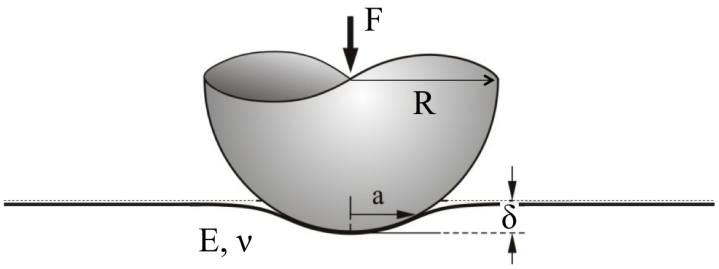

Figure 2.4.: Sketch depicting a hard spherical indenter of radius R pressing upon a semi-infinite, homogeneous, perfectly elastic substrate characterized by material parameters E and ν: this is the situation described by the Hertz model (Eq. 2.5). F: exerted force. a: contact radius. δ: indentation depth. Adapted from [169].

For a rigid spherical indenter pressing onto a semi-infinite, homogeneous, perfectly elastic substrate, in the absence of friction or adhesion, (the situation depicted in Figure 2.4) the force-indentation relation at small indentations is predicted to be of the form [182]:

$$F = \frac{4}{3}\frac{E}{(1-\nu^2)}\delta^{3/2}\sqrt{R} \tag{2.5}$$

where F is the force exerted by the indenter, δ the indentation depth reached, R the indenter radius, and ν and E the Poisson's ratio and Young's modulus of the substrate, respectively. Let's briefly recall the latter notions: Poisson's ratio (also known as *coefficient of expansion*) is the negative ratio of transverse to axial strain for the case of uniaxial stress:

$$\nu = -\frac{d\epsilon_{\text{trans}}}{d\epsilon_{\text{axial}}} \tag{2.6}$$

Assuming that a certain material is compressed along the z direction, ν basically quantifies the extent to which it will expand (or shrink) in the orthogonal directions x and y. Mathematically, in this case:

$$\nu = -\frac{d\epsilon_{\text{x}}}{d\epsilon_{\text{z}}} = -\frac{d\epsilon_{\text{y}}}{d\epsilon_{\text{z}}} \tag{2.7}$$

where $d\epsilon_{\text{x}} = \frac{dx}{x}$, $d\epsilon_{\text{y}} = \frac{dy}{y}$ and $d\epsilon_{\text{z}} = \frac{dz}{z}$ describe the infinitesimal diagonal strains.
The Young's (or elastic) modulus is instead a material parameter describing the mechanical properties of linear elastic solids by summarizing the relationship between tensional stress σ (force per unit area) and extensional strain ϵ (relative deformation).

It is in fact defined as:

$$E = \frac{\sigma}{\epsilon} \tag{2.8}$$

Clearly, no cell possesses such absolute material parameters as a Poisson's ratio or a Young's modulus, simply because the fundamental assumptions underlying such a description are not met by most biological materials. Within certain limits, though, the Hertz model can prove a useful approximation for describing experimental data, and a precious analytical tool for performing comparative studies of cell stiffness: the fact that the ever-growing body of literature describing cellular elasticity measurements often lacks in systematic coherence is not a measure of the unreliability of the method, but simply indicates how the values of E that are obtained from fitting the data can very strongly depend on a number of experimental settings. Such an approach is therefore only valuable provided that all experimental conditions are controlled very carefully.

2.2.1. Hertz model correction for thin layers

Given the assumptions made by the Hertz theory, the problem of extracting the elastic module of thin samples clearly cannot be addressed by directly using such an approach. For a long time, calculations for the case of finite thickness have imposed the need of extensive numerical computations based on complex mathematical manipulations.
Early examples include the works of Popov [162] as well as Chen and Engel [163]; the first method valid for incompressible materials (i.e., having a Poisson's ration ν=0.5, like typically assumed for biological samples) was developed by Hayes [161].
But it was not until the work of Dimitriadis [173] that an approximate analytical solution was developed. An important step in this direction was the finding that, for the case of very thin layers, the force-indentation relation strongly depends on whether or not the sample is bonded to the substrate [160]. This fact is of importance for biological materials, as it is not always easy to control their attachment to the underlying surfaces.
The approach followed by Dimitriadis is fascinating in its conceptual, if not mathematical, simplicity: imagine a spherical indenter applying a force F onto a sample of thickness h extending in the x-y plane and resting onto a rigid substrate located at $z = -h$ (the force is therefore applied in the negative z direction). An equivalent problem is constructed which combines multiple images of the actual probe so to satisfy all the boundary conditions of the original problem: this approach is the so-called method of images.
An infinite number of images is superimposed, and each of them is assumed to apply

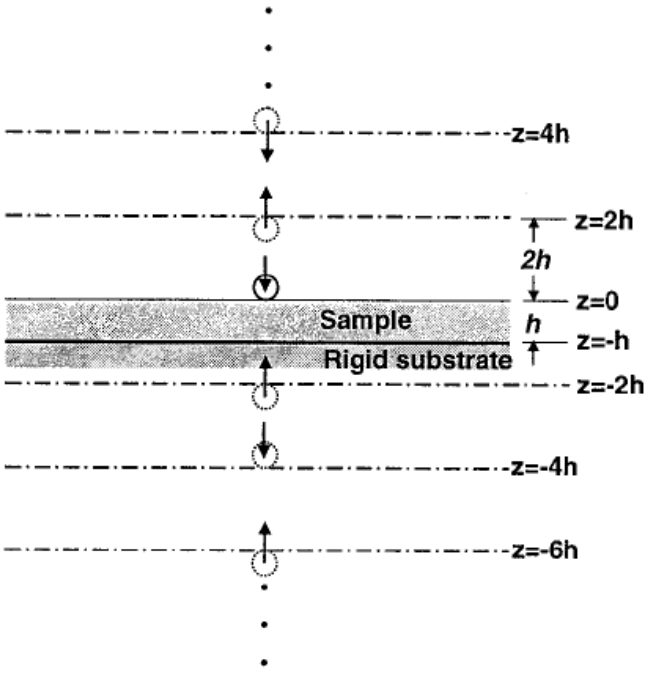

Figure 2.5: Method of images. An infinite sequence of images of the spherical probe satisfies all the boundary conditions (BCs) for the thin sample while acting on semi-infinite samples in the direction indicated by the arrows. The first $z = -2h$ image satisfies the rigid interface $z = -h$ BC, but results in a net stress on the free surface of the thin sample. That stress is eliminated by the second image source $z = 2h$ which, however, violates the rigid interface BC $z = -h$. This requires the next image $z = -4h$, and so on, ad infinitum and with the degree of BC violation decreasing with every pair of images. Source: [173].

the force to a semi-infinite sample for which the solution is known. This allows the construction of the pressure profile in Figure 2.5. The numerous mathematical steps required for this approach will not be reviewed here: it suffices to report the final solution, an expanded version of the Hertz formula taking into account the sample's thickness h according to:

$$F = \frac{4}{3}\frac{E}{(1-\nu^2)}\sqrt{R}\delta^{3/2}\Big[1-\frac{2\alpha_0}{\pi}\chi+\frac{4\alpha_0^2}{\pi^2}\chi^2-\frac{8}{\pi^3}\Big(\alpha_0^3+\frac{4\pi^2}{15}\beta_0\Big)\chi^3+\frac{16\alpha_0}{\pi^4}\Big(\alpha_0^3+\frac{3\pi^2}{5}\beta_0\Big)\chi^4\Big] \tag{2.9}$$

where $\chi = \sqrt{R\delta}/h$ (R and δ, according to the usual nomenclature, being the indenter radius and indentation depth, respectively).
In the case of a sample bonded to the substrate, the expansion parameters α_0 and β_0 are given by:

$$\alpha_0 = -\frac{1.2876 - 1.4678\nu + 1.3442\nu^2}{1-\nu}$$

$$\beta_0 = \frac{0.6387 - 1.0277\nu + 1.516\nu^2}{1-\nu}$$

Given the huge simplification it offers in data analysis, this approach has become growingly popular within the community of AFM users. Over time, its formulation has been expanded to describe other situations as well: E. Darling and coworkers, for instance, have adapted it to describe thin-layer viscoelastic models of stress relaxation [117].
J. Santos and colleagues instead focused on the generalization of the load-displacement relationship to describe other tip geometries [118]: finite element simulations have not only validated the resulting analytical solutions, but also calculated the error introduced by erroneously applying the Hertz model when the analyzed samples are too thin.
Finally, we mention the work of N. Gavara and R.S. Chadwick, who developed an analytical correction introduced for the indentation of adherent thin layers by means of conical tips. In this case, the force-displacement relationship becomes [91]:

$$F = \frac{8E\tan\alpha}{3\pi}\delta^2\Big(1 + 1.7795\frac{2\tan\alpha}{\pi^2}\frac{\delta}{h} + 16(1.7795)^2(\tan\alpha)^2\frac{\delta^2}{h^2}\Big) \tag{2.10}$$

with α the cone opening half-angle. When $h \to \infty$, the above equation reduces to the standard formulation of the Hertz model for conical indenters. This expression, as we will see in Section 5.4.1, is of great advantage for analyzing indentation curves recorded with sharp imaging tips.

2.3. Beyond the Hertz model: hyperelastic materials

The problem of modeling the mechanical response of biological materials has received growing attention over the past years. The complexity inherent in the behavior of soft tissues is in fact manifold: on the one hand, the very low elastic moduli and high heterogeneity in their composition gives nonlinear mechanical responses; on the other hand, it is hard to describe such materials without taking into account their viscoelastic nature and the large deformations they can sustain.
For now, a comprehensive theoretical framework in which experimental results can be embedded is still lacking, but a great deal can be learned from the application of continuum and contact mechanics to the analysis of indentation experiments. In the following, some basic concepts and nomenclature are introduced [157].

Cauchy's stress tensor and its invariants

Let's start by imagining a force ΔF which is exerted on the element of area ΔS belonging to the boundary surface S of a given body. Call $\boldsymbol{n}$ the unit vector normal to ΔS (see Fig. 2.6 A). If we assume that as ΔS tends to zero, the ratio $\Delta\mathbf{F}/\Delta$S tends to a definite limit $d\mathbf{F}/d$S, we can introduce a stress vector so defined:

$$\mathbf{T}^n = \frac{d\mathbf{F}}{dS} \tag{2.11}$$

We call this vector the *traction*.
Cauchy's stress theorem states that if the components τ_{ij} of the stress tensor are known, then the stress vector acting on any surface having unit outer normal vector $\boldsymbol{n}$ can be written as

$$T_i^n = n_j \tau_{ji} \tag{2.12}$$

where the Einstein notation for index summation is implied. This result basically assures us that knowing the nine components of stresses τ_{ij} is a necessary and sufficient condition to define the traction across any other surface element in a body. This leads to the definition of Cauchy's stress tensor $\boldsymbol{\sigma}$; a second-order tensor consisting of nine components σ_{ij} that define the state of stress at a point inside a material in the deformed state. Each component describes the force per unit area that the part lying on the positive side of a surface element (i.e., the positive side of the outer normal) exerts on the part lying on the negative side (see Fig. 2.6 B). In mathematical terms:

$$\mathbf{T}^n = \boldsymbol{n} \cdot \boldsymbol{\sigma} \text{ or } T_j^n = \sigma_{ij} n_i \tag{2.13}$$

where

$$\boldsymbol{\sigma} = \begin{bmatrix} \sigma_{11} & \sigma_{12} & \sigma_{13} \\ \sigma_{21} & \sigma_{22} & \sigma_{23} \\ \sigma_{31} & \sigma_{32} & \sigma_{33} \end{bmatrix} = \begin{bmatrix} \sigma_x & \tau_{xy} & \tau_{xz} \\ \tau_{yx} & \sigma_y & \tau_{yz} \\ \tau_{zx} & \tau_{zy} & \sigma_z \end{bmatrix}$$

Here, the components σ_{11}, σ_{22} and σ_{33} are called the normal stresses, and the remaining τ_{ij} components are the shear stresses (note that the second notation is most often encountered in engineering books, whereas the first one is favored in physics literature).

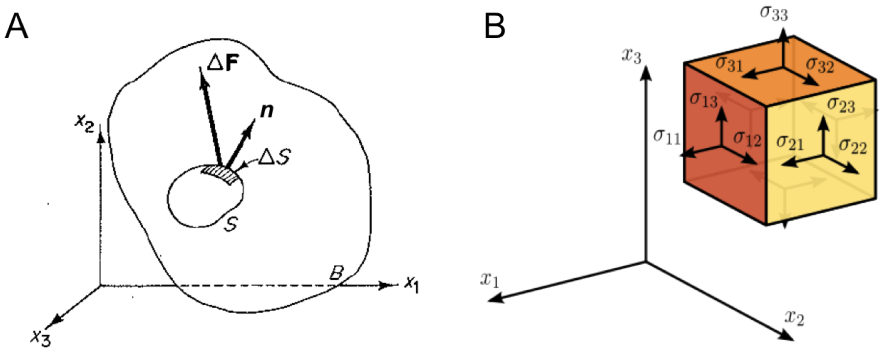

Figure 2.6.: A. Surface force ΔF acting on an element of area ΔS and the outer normal unit vector $\boldsymbol{n}$ defining it. **B.** Components of the stress tensor in a cartesian coordinate system.

The principle of conservation of angular momentum implies that the stress tensor is symmetric: this means that it is always possible to find a set of coordinates with respect to which $\boldsymbol{\sigma}$ can be reduced to a diagonal matrix of the form:

$$\boldsymbol{\sigma} = \begin{bmatrix} \sigma_1 & 0 & 0 \\ 0 & \sigma_2 & 0 \\ 0 & 0 & \sigma_3 \end{bmatrix}$$

This set of coordinates are called the *principal axes* and the coordinate planes they determine are called the *principal planes*. Let now $\boldsymbol{n}$ be a unit vector in direction of a principal axis and let $\boldsymbol{\sigma}$ be the corresponding principal stress. Then the stress vector acting on the surface normal to $\boldsymbol{n}$ has components σn_i, but the same vector is also given by $\tau_{ji} n_j$. Therefore,

$$(\tau_{ji} - \sigma\delta_{ji}) n_j = 0 \;\text{ for }\; i = (1, 2, 3) \tag{2.16}$$

where, again, the Einstein notation for index summation is implied. Here and in the

following, δ_{ji} is the Kronecker delta. This system of three equations has a set of non-vanishing solutions n_1, n_2 and n_3 only if the determinant of the coefficients vanishes, i.e.:

$$|\tau_{ij} - \sigma\delta_{ij}| = -\sigma^3 + I_1\sigma^2 - I_2\sigma + I_3 = 0 \tag{2.17}$$

where

$$\begin{aligned} I_1 &= \sigma_1 + \sigma_2 + \sigma_3 = tr(\boldsymbol{\sigma}) \\ I_2 &= \sigma_1\sigma_2 + \sigma_2\sigma_3 + \sigma_3\sigma_1 = \frac{1}{2}[tr(\boldsymbol{\sigma})^2 - tr(\boldsymbol{\sigma}^2)] \\ I_3 &= \sigma_1\sigma_2\sigma_3 = det(\boldsymbol{\sigma}) \end{aligned} \tag{2.18}$$

I_1, I_2 and I_3 are important quantities which are independent of the coordinate system: therefore, they are called the *invariants* of the stress tensor. The same principle can apply also to other tensors: physically, I_1 is directly related to the hydrostatic component of the tensor; I_2 tends to be related to the deviatoric aspects of (in this case) the stress, and finally I_3 does not seem to have any physical significance in general, but it does when applied to the deformation gradient (in that case, in fact, I_3 represents the ratio of deformed to initial volume: $I_3 = V_F/V_0$).
Studying the mechanical response of a body would be impossible without analyzing its deformation. To this end, it is useful to introduce the *displacement vector* $\mathbf{u}$ with components

$$u_i = x_i - x_i' \tag{2.19}$$

where x_i' are the initial coordinates of a point in the body, and x_i the deformed ones. For small displacements, an *infinitesimal strain tensor* $\boldsymbol{\epsilon}$ can be defined

$$\boldsymbol{\epsilon} = \begin{bmatrix} \epsilon_{11} & \epsilon_{12} & \epsilon_{13} \\ \epsilon_{21} & \epsilon_{22} & \epsilon_{23} \\ \epsilon_{31} & \epsilon_{32} & \epsilon_{33} \end{bmatrix} \tag{2.20}$$

having components

$$\epsilon_{ij} = \frac{1}{2}\Big[\frac{u_j}{x_i} + \frac{u_i}{x_j}\Big] \tag{2.21}$$

The idea that stress in a body is related to the strain was first announced by Robert Hooke in 1676, when he observed the proportionality between the force of a spring and the extent of its deformation [158]. Since then, major progress has been made in deci-

phering the mechanical behavior of large classes of materials, but the central problem in solid mechanics has remained that of determining the displacement field $\mathbf{u}(\mathbf{x}, t)$ and the Cauchy stress distribution σ_{ij} as a function of position and time.

In general, for non-fluid systems, the internal forces generated by the deformation dominate the response: as a consequence, a huge number of material models exists. If we exclude viscoplastic and plastic responses, we mainly distinguish two major groups:

- *Linear elastic* constitutive laws model the reversible behavior of materials under small strains. In this case, all governing equations can be linearized (provided that the stresses are sufficiently small) rendering this theory the simplest to apply and thereby the most used approximation of solid mechanics.

  As previously mentioned, this is also the assumption made by the Hertz model, which describes elastic materials for which in uniaxial stretching stress and strain are linked via the proportional constant E

  $$E = \frac{\sigma}{\epsilon} \tag{2.22}$$

  commonly known as Young's (or elastic) modulus.

- *Hyperelastic* constitutive relations model materials that behave elastically under very large strains. The stress-strain relation is no longer linear, and is typically defined by an equation relating the free energy of the material to the deformation gradient. Given the importance of this class of models in describing biological materials, we shall briefly introduce the most relevant ones.

Hyperelastic materials

The governing equations of hyperelastic materials are often written in terms of quantities such as the deformation gradient, having components:

$$F_{ij} = \delta_{ij} \frac{u_i}{x_j} \tag{2.23}$$

or the right and left Cauchy-Green rotation-independent deformation tensors, having components:

$$C_{ij} = F_{ki} F_{kj} \text{ and } B_{ij} = F_{ik} F_{jk} \tag{2.24}$$

respectively. Similarly to what done for the principal stress tensor, one can also derive invariants of the various strain tensors. The invariants of $\mathbf{C}$, for instance, can be written as follows:

$$\begin{aligned} I_1 &= tr(\mathbf{C}) = C_{kk} \\ I_2 &= \frac{1}{2}[(tr(\mathbf{C}))^2 - tr(\mathbf{C}^2)] \\ I_3 &= det(\mathbf{C}) \end{aligned} \tag{2.25}$$

An alternative set of invariants, more convenient for models of nearly incompressible materials, are:

$$\begin{aligned} \bar{I}_1 &= I_1/J^{2/3} \\ \bar{I}_2 &= I_2/J^{4/3} \\ J &= \sqrt{I_3} \end{aligned} \tag{2.26}$$

where J represents the Jacobian determinant ($J = det(\mathbf{F})$). Constitutive equations for hyperelastic materials are based on a strain energy function $W(\epsilon_{11}, \epsilon_{12}, ..., \epsilon_{33})$ which relates the energy stored in a material to the deformation [154]. Such function depends on the strain components according to the relation:

$$\sigma_{ij} = \frac{W}{\epsilon_{ij}} \tag{2.27}$$

An alternative way to explain this is perhaps the following: elastic materials are those for which the constitutive behavior is only a function of the current state of deformation; in the special case in which the work done by the stresses during such a deformation are path-independent (i.e., only depend on the initial and final configuration), materials are classified as hyperelastic. This path-independence allows to define the strain energy function (per unit of undeformed volume) as the work done by the stresses during the whole deformation [119]. Equation 2.27 is a consequence of such definition.

In the case of isotropic materials (i.e. those materials whose constitutive equations are unaltered under orthogonal transformations of coordinates, meaning translations, rotations and reflections), it can be shown that the strain energy function depends on the invariants of the strain only:

$$W = W(I_1, I_2, I_3) \tag{2.28}$$

One of the first works introducing this approach was published by Y.C. Fung in 1967 [159]. His paper, a cornerstone amongst biomechanical studies, reported data from uniaxial tests on rabbit mesentry (a thin membranous tissue lining the walls of the peritoneal cavity) that revealed a strongly non-linear relationship between stress and stretch. Tissue response under cyclic loading was relatively insensitive to strain rate, and resulted reproducible only after a few "preconditioning" cycles. This lead Fung to coin the term *pseudoelasticity* to refer to the behavior of soft tissue. He noted that by plotting an equivalent measure for the stiffness of the mesentery (i.e., $dP_{11}/d\lambda$, where P_{11} is the uniaxial first Piola-Kirchoff stress $\mathbf{P} = \frac{W}{\mathbf{F}}$ and λ the stretch ratio) versus the applied stress, one obtained a near linear relationship ($dP_{11}/d\lambda = \alpha + \beta P_{11}$, with α and β two material parameters). This first-order differential equation implied an exponential form of the stress-strain relation. Fung therefore postulated the existence of a three-dimensional pseudostrain energy function $W = c(e^Q - 1)$, where c is a constant and Q a function of the Green strain tensor $(\mathbf{F}^T \cdot \mathbf{F} - I)/2$ ($\mathbf{F}$ being the above-defined deformation gradient tensor). Various functional forms for Q were considered and the final quadratic form (in terms of the components of $\mathbf{E}$) was chosen based on fits of data. This assumption then allowed to derive the stress-strain relationship [159].

Such an approach well exemplifies the phenomenological nature of most hyperelastic models (such as those developed by *Mooney-Rivlin*, *Ogden*, *Tschoegl-Gurer* or *Saint Venant-Kirchhoff* [155]). A few notable exceptions lie in the so called mechanistic models, derived from arguments about the underlying nature of materials, rather than by mere data fitting: these generally premise on the description of materials as networks of interconnected chains, and are developed from the statistical thermodynamics of the underlying macromolecular network structure [155]. The *neo-hookean model*, for instance, perhaps the simplest hyperelastic model, assumes the networks can be described as freely jointed chains obeying Gaussian statistics [156]. Other molecular formulations include the *Arruda-Boyce* or the *Gaylord-Douglas* approaches.
Generally, most hyperelastic models have been developed to describe elastomers and rubbers, but a lot of soft tissues happen to exhibit the same non-linear, inelastic character and a thermoelastic behavior very similar to that of elastomers. Advances in rubber and tissue elasticity proceeded hand in hand during the whole first half of the 20^{th} century [124], and hyperelastic models became increasing popular to describe biological materials.
In the following section we will introduce the ones that have been most successfully applied to the study of soft tissue.

2.3.1. The Mooney-Rivlin model

Despite being developed independently, the Mooney-Rivlin model results into a generalization of the neo-Hookean one: it assumes a strain energy function that is linear in the first and second invariant of the deviatoric part of the right Cauchy-Green strain tensor [122]-[121] and is uncoupled in its deviatoric and volumetric parts:

$$W = C_1(\bar{I}_1 - 3) + C_2(\bar{I}_2 - 3) + \frac{K_1}{2}(J-1)^2 \tag{2.29}$$

Here, $\bar{I}_1$ and $\bar{I}_2$ are the first and second deviatoric invariants, J is the Jacobian of the deformation and C_1 and C_2 are the Mooney-Rivlin material coefficients.
For small deformations, K_1 is a constant that reduces to the bulk's modulus K and the sum of the C_i coefficients is proportional to the initial shear modulus μ_0 according to $\mu_0 = 2(C_1 + C_2)$ [120].
Poisson's ratio is related to the bulk modulus and the initial shear modulus by:

$$\nu = \frac{3K - 2\mu_0}{6K + 2\mu_0} \tag{2.30}$$

If C_2=0, Equation 2.29 reduces to the neo-Hookean model. In the case of incompressible materials (i.e., if $\nu = 0.5$), the condition of volume conservation is expressed by J=1; the notion of bulk modulus loses its meaning (or, more precisely, $\lim_{\nu \to 0.5} K(\nu) = \infty$).
Given that many biological samples exhibit a rather incompressible behavior, under physiological loading (due to the high volume fraction of water they contain), this simplification is adopted very often. In this case, the invariants become $\bar{I}_1$=I_1 and $\bar{I}_2$=I_2 and Equation 2.29 reduces to:

$$W = C_1(I_1 - 3) + C_2(I_2 - 3) \tag{2.31}$$

2.3.2. The Ogden model

The Ogden material model, developed in 1972 for describing incompressible rubber-like solids, assumes a strain energy function of the form [93]:

$$W = \sum_{i=1}^{N} \frac{2C_i}{\alpha_i^2}(\lambda_1^{\alpha_i} + \lambda_2^{\alpha_i} + \lambda_3^{\alpha_i} - 3) + \frac{K_1}{2}(J-1)^2 \tag{2.32}$$

where λ_1, λ_2 and λ_3 are the principal stretches in the cartesian directions, and C_i and α_i represent material parameters. For small strains, K_1 reduces to the bulk's modulus K and the sum of the coefficients C_i approximates the shear modulus according to

$\mu_0 = \sum_1^N \mu_i$. Fitting of the experimental data is usually performed by retaining up to several terms in the summation [155]. Again, in case of incompressible materials J=1.

2.3.3. The Fung model

Finally, as already anticipated, the Fung model was developed for describing preconditioned soft biological materials [159] by postulating an exponential form of the stress-strain relationship. For isotropic materials, the simplified strain energy function is in the form [155]:

$$W = \frac{C}{2b}\{\exp[b(I_1 - 3)] - 1\} \tag{2.33}$$

where I_1 is once again the first strain invariant, b represents a stiffening parameter and, for small strains, C is the infinitesimal shear modulus μ_0.

2.3.4. Adaptation of hyperelastic models to AFM indentation experiments

The general stress-strain formulations of the aforementioned strain energy equations are rather bulky; but if one is interested in only analyzing specific deformation modes, they can be simplified. It is important at this point to underline that constitutive equations only describe the behavior of a material *under specific conditions of interest* rather than the material itself.
Hyperelastic models basically offer curve-fits of various polynomials to test data, but the coefficients determined from one deformation type have limited values for predicting the behavior of other deformation types [155]. In other words, the stress-strain equations (along with the corresponding C_i values) will be different for different modes of deformation (like, for instance, uniaxial tension, equibiaxial tension, pure shear, etc.).
We will focus our attention to the simplest case, that of uniaxial tension, and restrict to the Mooney-Rivlin model. The stress-strain relationship can in this case be written as:

$$\sigma = 2C_1(\lambda - \lambda^{-2}) + 2C_2(1 - \lambda^{-3}) \tag{2.34}$$

where λ is the principal stretch. As we are about to see, this equation can be rewritten in order to directly apply to the analysis of AFM indentation experiments.
D. Lin and co-workers [153] were the first to derive the force-indentation relation expected from the contact problem of a rigid spherical indenter pressing on a Mooney-Rivlin material. Starting from Equation 2.34, they defined an effective stress due to indentation as the mean contact pressure:

$$\sigma^* = \frac{F}{\pi a^2} \tag{2.35}$$

where F is the force exerted by the indenter and a the contact radius. Similarly, an effective indentation strain is defined as:

$$\epsilon^* = \frac{a}{R} \tag{2.36}$$

R being the indenter radius. Since λ is the extension ratio, we can substitute it with $\lambda = 1 - \epsilon^*$ in Equation 2.35. After some algebraic manipulation, Equation 2.35 becomes:

$$\frac{\sigma^*}{\epsilon^*} = B_1\Big(\frac{\epsilon^{*3} - 3\epsilon^{*2} + 3\epsilon^*}{\epsilon^{*3} - 2\epsilon^{*2} + \epsilon^*}\Big) + B_2\Big(\frac{\epsilon^{*3} - 3\epsilon^{*2} + 3\epsilon^*}{-\epsilon^{*4} + 3\epsilon^{*3} - 3\epsilon^{*2} + \epsilon^*}\Big) \tag{2.37}$$

where the constants C_1 and C_2 have been replaced by $B_1/2$ and $B_2/2$, respectively. Assuming that the relationship between indentation depth and contact radius is of the form $a = \sqrt{R\delta}$, this finally leads to an equation expressing the force F in terms of the indentation depth δ:

$$F = \pi R^{1/2} B_1\Big(\frac{\delta^{5/2} - 3R^{1/2}\delta^2 + 3R\delta^{3/2}}{\delta - 2R^{1/2}\delta^{1/2} + R}\Big) + \pi R^{1/2} B_2\Big(\frac{R^{1/2}\delta^{5/2} - 3R\delta^2 + 3R^{3/2}\delta^{3/2}}{-\delta^{3/2} + 3R^{1/2}\delta - 3R\delta^{1/2} + R^{3/2}}\Big) \tag{2.38}$$

At infinitesimal strain (or indentation depth) the Hertz model applies again, so that the condition

$$B_1 + B_2 = \frac{4E_0}{9\pi(1-\nu^2)} \tag{2.39}$$

holds. A similar approach has enabled the derivation of force-indentation relations for a number of other hyperelastic models [155]. The ones used in this work are described in Tables 2.1 and 2.2.

Table 2.1.: Hyperelastic strain energy functions and corresponding uniaxial stress-strain equations. Source: [155].

Model	W: strain energy potential $\sigma = \sigma(\lambda)$: uniaxial stress-stretch equation μ_0=initial shear modulus
Mooney-Rivlin	$W = C_1(I_1 - 3) + C_2(I_2 - 3)$
	$\sigma = 2C_1(\lambda - \lambda^{-2}) + 2C_2(1 - \lambda^{-3})$
	$\mu_0 = 2(C_1 + C_2)$
	Fitting parameters: C_1,C_2
Ogden	$W = \sum_{i=1}^{N} \frac{2C_i}{\alpha_i^2}(\lambda_1^{\alpha_i} + \lambda_2^{\alpha_i} + \lambda_3^{\alpha_i} - 3)$
	$\sigma = \sum_{i=1}^{N} \frac{2C_i}{\alpha_i}(\lambda^{\alpha_i - 1} - \lambda^{-\alpha_i/2-1})$
	$\mu_0 = \sum_{i=1}^{N} C_i$
	Fitting parameters: C_i,α
Fung	$W = \frac{C}{2b}\{\exp[b(I_1 - 3)] - 1\}$
	$\sigma = C(\lambda - \lambda^{-2})\exp[b(I_1 - 3)]$
	$\mu_0 = C$
	Fitting parameters: C, b

Here, assuming material incompressibility, $\mathrm{I}_1 = \lambda_1^2 + \lambda_2^2 + \lambda_3^2$; $\mathrm{I}_2 = \lambda_1^{-2} + \lambda_2^{-2} + \lambda_3^{-2}$; $\lambda_1 = \lambda; \lambda_2 = \lambda_3 = \lambda^{-1/2}$; $\sigma = \lambda(\partial W/\partial\lambda)$ and $\epsilon = \lambda - 1$.

Table 2.2.: Force-indentation relations for hyperelastic strain energy functions. Source: [155].

Model	$F = F(\delta)$: uniaxial force-indentation equation	
Mooney-Rivlin	$F = B_1\pi\left(\frac{a^5 - 15Ra^4 + 75R^2a^3}{5Ra^2 - 50R^2a + 125R^3}\right) + B_2\pi\left(\frac{a^5 - 15Ra^4 + 75R^2a^3}{-a^3 + 15Ra^2 - 75R^2a + 125R^3}\right)$	(2.40)
	$B_1 + B_2 = \frac{20E_0}{9\pi(1-\nu^2)}$	(2.41)
Ogden	$F = \frac{B\pi a^2}{\alpha}\left[(1 - 0.2\frac{a}{R})^{-\alpha/2-1} - (1 - 0.2\frac{a}{R})^{\alpha-1}\right]$	(2.42)
	$B = \frac{40E_0}{9\pi(1-\nu^2)}$	
Fung	$F = B\pi\left(\frac{a^5 - 15Ra^4 + 75R^2a^3}{5Ra^2 - 50R^2a + 125R^3}\right)exp\left[b\left(\frac{a^3 - 15Ra^2}{25R^2a - 125R^3}\right)\right]$	(2.43)
	$B = \frac{20E_0}{9\pi(1-\nu^2)}$	

E_0: initial Young's modulus; R: indenter radius; $a = a(R) = \sqrt{R\delta}$: contact radius.

2.4. Finite element simulations

The analytical solutions introduced above are in all cases only approximations of the mechanical response of cellular systems. Their precision can vary, but they still rely on large simplifications of the systems under study in order to provide the governing equations of material behavior. When trying to characterize the mechanical response of complex and heterogeneous materials, therefore, numerical methods can represent a far richer alternative to simplified analytical formulations.

The finite element method (FEM) is a numerical technique used to obtain approximate solutions to boundary value problems in engineering. First systematized by A. Hrennikoff [129] and R. Courant [128], this technique actually is rooted in the work of B. G. Galerkin and W. Ritz, who developed a method allowing to convert continuous operator problems, such as for instance differential equations, into discrete problems.
This technique was originally used to solve complex structural analyses in civil and aeronautical engineering, but it quickly expanded to cover a large variety of applications. The idea at the base of FEM simulations is the following: all the laws characterizing the mechanical behavior of biological materials described so far are expressed with respect to a continuous deformation in space, and are often partial differential equations (PDEs). Imagine now to discretize this continuum into a mesh composed by a set of discrete sub-domains (also known as *elements*): if one could find a way to connect many simple element equations over the small sub-domains so as to approximate the complex PDE characterizing the whole continuum, the problem would basically be broken down into many smaller problems. This is exactly the idea at the base of the Galerkin method [127]: in practice, the PDE is locally approximated with a set of algebraic equations (in the case of steady-state problems) or ordinary differential equations (in the case of transient problems) which can be more easily handled numerically.
The following steps summarize the basic steps performed during a finite element analysis [126]:

- *Discretization of the continuum*: the complex geometry of the object under study is defined and then subdivided into mesh of smaller elements connected at nodal points (see Fig. 2.7); the mechanical behavior of each element can be defined by a set of differential equations.

- *Selection of interpolation functions*: the differential equations are converted into appropriate approximated algebraic equations and then into matrix equations (of-

ten via the Galerkin method).

- *Assembly of the element equations*: element equations must be combined in order to obtain a global equation system for the whole solution region.
- *Incorporation of load and boundary conditions* into the structural matrix.
- *Solution of the structural matrix* and calculation of all nodal deflections.
- *Computation of additional results*: often, additional parameters need to be calculated. An example in mechanical problems are stresses and strains, which can only be obtained after the displacements have been computed from solution of the global equation system.

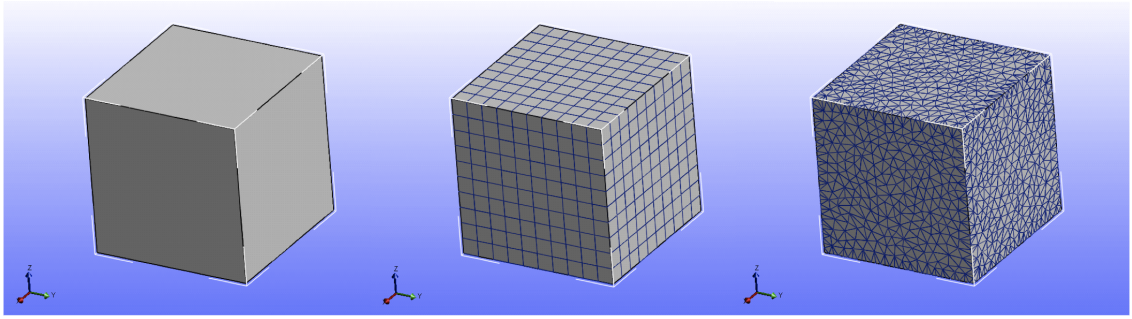

Figure 2.7.: Example of the creation of two different meshes on top of a cubical volume element: in the first case a simple hexahedral geometry is used; in the second, we create a finer 10-node quadratic tetrahedral mesh.

In the final part of this work, we will use FEM simulations to complement the experimental results on the mechanical characterization of MCF10A acini and to validate the hyperelastic material models used to analyze AFM data.

3. Materials and methods

3.1. List of materials

The following tables present a list of all materials, chemicals and instrumentation used during this work; the only exception are the fluorescent dyes and antibodies used during immunostainings and western blots, which will be described in the upcoming section.

3.1.1. Disposable materials

Arrow-TL1Au tipless AFM cantilevers	Nano World
Aspiration pipettes (5 mL, 10 mL)	VWR
Borosilicate glass microcapillaries (R=0.5 µm)	Hilgenberg
Cell culture dishes with 18 mm hole (diameter: 35 mm)	Cell E&G
Cell culture flasks (25 cm^2, 75 cm^2)	BD Biosciences
Cryogenic vials	VWR
Culture treated Petri dishes (diameter: 35 mm)	VWR
Eppendorf tubes, safe lock	Eppendorf
Falcon tubes (15 mL, 50 mL)	BD Biosciences
Glass coverslips (thickness: 80 µm)	Menzel Gläser
Glass coverslips (thickness: 170 µm)	Menzel Gläser
Glass coverslips (thickness: 160 µm, diameter: 18 mm)	Menzel Gläser
Glass microspheres (radius: 30-50 µm)	Polysciences Inc.
Glass Pasteur pipettes	VWR
Hybond-P PVDF membrane	Amersham Pharmacia Biotech.
Kimtech Science precision wipes	Kimberly-Clark

DISPOSABLE MATERIALS	SUPPLIER
Latex gloves	Meditrade
Low bind reaction vessels (1.5 mL)	Eppendorf
Mini-PROTEAN TGX gels	BioRad
µ-Dish$^{35\ mm}$	Ibidi
µ-Slide 8 well	Ibidi
Pipette tips (1-10 µL, 2-200 µL, 50-1000 µL)	Eppendorf
Point probes-CONT-50 silicon AFM cantilevers	Nanosensors
Reaction vessels (0.5 mL, 1.5 mL, 2 mL)	Eppendorf
Silica microspheres (radius: 5 µm)	G.Kisker GbR
Sterile filters (radius: 0.1 µm)	Pall corporation
Sterillium Virugard	BODE Chemie
Sylgard-184 silicone elastomer kit	Dow Corning
Thick blot paper	BioRad
UHU plus Endfest 300 bicomponent glue	UHU
Weighing boats	VWR

3.1.2. Chemicals

Acetic acid, glacial ACS grade	VWR
Acetone for analysis, Emsure grade	Merck Millipore
Adenin	Sigma
BCIP/NBT (5-brom-4-chlor-3-indoxylphosphate)	Sigma Aldrich
BSA (bovine serum albumin)	Merck Millipore
Chelex 100	BioRad
Cholera toxin	Sigma Aldrich
Cell recovery solution	BD Bioscience
Collagen, type I (rat tail)	BD Bioscience

CHEMICALS	SUPPLIER
Collagenase type IV	Worthington Biochemical Corporation
Cryo-SFM (serum-free-medium)	Promo Cell
DABCO (1,4-Diazabicyclo[2.2.2]octane)	Sigma-Aldrich
Dextran Conjugates, TexasRed (3 kDa, 10 kDa, 40 kDa) neutral	Molecular Probes, Invitrogen
DMEM/F12 (1:1) medium	Life Technologies
DMEM/Ham's F12 (3.5:1.1) medium	Life Technologies
EGF (epidermal growth factor), human	Sigma Aldrich
EDTA (ethylenediaminetetraacetic acid)	Sigma Aldrich
EGTA (ethylene glycol tetraacetic acid)	Sigma Aldrich
Ethanol absolute for analysis, Emsure grade	Merck Millipore
FCS (fetal calf serum) Gold	PAA
Fibronectin, human	BD Biosciences
Fluoromount	Sigma Aldrich
Formaldehyde, proteomics grade, 37%	Sigma Aldrich
GelTrex LDEV-Free Reduced Growth Factor Basement Membrane Matrix	Life Technologies
Glucose	Sigma Aldrich
Glutamin	Invitrogen
Glutaraldehyde, EM Grade, 25%	Ted Pella, Inc.
Glycine	Sigma Aldrich
HBSS (Hank's balanced salt solution)	Life Technologies
HEPES buffer	Sigma Aldrich
Horse serum	Life Technologies
Hydrochortisone	Sigma Aldrich
Insulin human recombinant	Sigma Aldrich
KCl	Sigma Aldrich

CHEMICALS	SUPPLIER
KH_2PO_4	Sigma Aldrich
Latrunculin A	Sigma Aldrich
MES (2-(N-morpholino)-ethanesulfonic acid)	Sigma Aldrich
Methanol for analysis, Emsure grade	Merck Millipore
$MgCl_2$	Sigma Aldrich
Na_2HPO_4	Sigma Aldrich
$NaBH_4$	Merck Millipore
NaCl	Sigma Aldrich
Octyl-β-D-glucopyranoside	Sigma Aldrich
Paraformaldehyde, ACS reagent grade, 37%	Sigma Aldrich
Penicillin-Streptomycin, liquid, 10000 Units/mL	Life Technologies
Poly-L-lysine	Sigma Aldrich
Precision Plus Protein Kaleidoscope Prestained Protein Standards	BioRad
Pyruvate	PAA
RPMI 1640 Medium, GlutaMAX	Life Technologies
RPMI 1640 Medium, HEPES	Life Technologies
Skim milk powder	Sigma Aldrich
Tris/Glycine/SDS buffer	BioRad
Triton-X-100	Sigma Aldrich
Trypsin-EDTA 0.05%, phenol-red	Life Technologies
Tween-20	Sigma Aldrich

3.1.3. Instrumentation

208 HR sputter coater	Cressington
Atomic force microscope AFM Nanowizard Lifescience	JPK
Axio Observer Z1	Carl Zeiss

INSTRUMENTS	SUPPLIER
Axiovert 200	Carl Zeiss
Axiovert 40 CFL	Carl Zeiss
Centrifuge 5415R	Eppendorf
CPD 030 critical point dryer	Bal-Tec
FemtoJet microinjector	Eppendorf
Flaming/Brown P-97 micropipette puller	Sutter Instruments
FluoArc fluorescent lamp	Carl Zeiss
Incubator XL 2	Carl Zeiss
InjectMan micromanipulator	Eppendorf
KNF Laboport Solid PTFE Vacuum Pump	KNF Neuberger Inc.
Laboratory scales JB1603-C/FACT	Mettler-Toledo
Laser scanning microscopes LSM 510, LSM 710, LSM 880 with Airyscan	Carl Zeiss
Megafuge 1.0 (Rotor: BS4402/A)	Heraeus/Kendro
Mini-PROTEAN electrophoresis system	BioRad
Mini Trans-Blot cell	BioRad
Moxi Z mini, automated cell counter	Orflo Technologies
pH-Meter, 766 Calimatic	Knick
STEMI-2000 CS stereo microscope	Carl Zeiss
Sterile workbench Hera Safe	Heraeus/Kendro
Scanning electron microscope Gemini SEM 500	Carl Zeiss
Thermo-Forma Steri-Cycle CO2 Incubator	ThermoFisher Scientific
Vortex REAX top	Heidolph
Waterbath WB22	Memmert

3.2. Cell culture

All cells were cultivated in a humidified environment at controlled temperature (37°C) and CO_2 level (5%), and all handling and working with cells was conducted in sterile conditions under a bench.

Preparation of glass bottom culture dishes

For the cultivation of 3D cell cultures on substrates which would allow microscopy, hollow plastic culture dishes having an outer diameter of 35 mm and an inner diameter of 18 mm were glued to precision cover glasses (170±5 µm in thickness) by means of Sylgard-184 silicone elastomer kit with a base to curing agent mass ratio of 10:1. Before it could be applied to the culture dishes, the elastomeric compound was thoroughly mixed and subsequently degassed for several minutes using a vacuum pump. After application of the glass coverslips, the culture dishes were heat cured at 60°C for at least three hours.

3.2.1. Buffer composition

In the following tables, the composition of the buffer solutions used during routine cell culture work is reported.

CB (Cytoskeleton Buffer) pH 6.1	
EGTA	1.902 g/L
Glucose	0.9 g/L
MES	1.95 g/L
$MgCl_2$	0.476 g/L
NaCl	8.77 g/L
Streptomycin	1 g/L

PBS (Phosphate Buffered Saline) pH 7.2	
NaCl	8 g/L
Na_2HPO_4	1.15 g/L
KCl	0.2 g/L
KH_2PO_4	0.2 g/L

3.2.2. Keratinocyte cell culture

Production of keratin-lacking KO keratinocytes was performed at the faculty for biosciences, pharmacy and psychology of the University of Leipzig by the group of Prof. T. Magin and described in detail in [25]. Wild-type (WT), knock-out (KO) and rescue (RES) epidermal keratinocytes were grown in FAD^+ medium having the composition reported in Table 3.1.

Table 3.1.: Medium recipes for cultivation of WT, KO and RES keratinocyes

FAD^+ medium	
DMEM/Ham's F12 (3.5:1.1) medium	ad 500 mL
Adenin	0.18 mM
Chelex-treated FCS	10%
Cholera toxin	10^{-5} M
EGF	10 ng/mL
Glutamin	2 mM
Hydrocortisone	0.5 µg/mL
Insulin	5 µg/mL
Penicillin	100 U/mL
Pyruvate	1%
Streptomycin	100 µg/mL

Prior to addition of all necessary supplements, fetal calf serum (FCS) was incubated overnight on a rotor with 8 g/50 mL Chelex 100 in order to remove Ca^{2+} ions. This procedure was repeated a second time before a sterile filtration was performed (filter radius: 0.1 µm); FCS was then added to DMEM/Ham's F12 (3.5:1.1) medium, which was thereafter denoted as FAD^+.
Cells were passaged every 3-4 days upon reaching about 90% confluence. To this end, all media were pre-warmed to 37°C; cells were washed with PBS and incubated at 37°C for 10 minutes with 1 mL of trypsin-EDTA solution. The enzymatic reaction induced by trypsin was blocked by addition of 2 mL of serum-containing FAD^+ medium. The cells were resuspended and centrifuged at 180 g for 3 minutes. After elimination of the supernatant, the cell pellet was resuspended in 2 mL of fresh FAD^+ medium and used for experiments or for further cultivation.

Western blotting on keratinocytes

Sodium Dodecyl Sulphate - PolyAcrylamide Gel Electrophoresis (SDS/PAGE) on crude protein extracts of all cell lines analyzed (WT, KO and RES keratinocytes) was performed as described in [178]. Separation of total protein extracts was performed by standard procedures (4-20% SDS-PAGE). Using GAPDH as constitutively expressed marker (antibody G8795; Sigma-Aldrich), overall protein levels of actin and tubulin were determined using mAB8457 (Cell Signaling Tech.) and MAB1864 (Merck Millipore) as antibodies.

3.2.3. MCF10A cell culture

MCF10A cells were obtained by ATTC (Manassas, USA) and grown in DMEM/F12 medium having the composition reported in Table 3.3, based on [52].

Table 3.2.: Medium recipe for maintenance of MCF10A in 2D and 3D cultures

Components	**Growth medium (2D)**	**Assay medium (3D)**	**EGF-free assay medium (3D)**
DMEM/F12 1:1	ad 500 mL	ad 500 mL	ad 500 mL
Cholera toxin	100 ng/mL	1 ng/mL	1 ng/mL
EGF	20 ng/mL	5 ng/mL	-
Horse serum	5%	2%	2%
Hydrocortisone	0.5 µg/mL	0.5 µg/mL	0.5 µg/mL
Insulin	10 µg/mL	10 µg/mL	10 µg/mL
Penicillin/streptomycin	100 U/mL	100 U/mL	100 U/mL
GelTrex	-	2%	2%

Cells were passaged every 3-4 days upon reaching about 80% confluence. To this end, all media were pre-warmed to 37°C; cells were washed with PBS and incubated at 37°C for about 5-7 minutes with 2 mL of 0.05 Trypsin-EDTA solution. 2 mL growth medium were added to the suspension which was successively centrifuged at 180 g for 4 min. After elimination of the supernatant, the cell pellet was resuspended in 2 mL of fresh medium and used for experiments or for further cultivation.

3D cell culture of MCF10A acini

The protocol for 3D cell culture was adapted from previous publications [52]-[179]. In short, MCF10A acini were cultivated for a period of up to 35 days on growth factor reduced EHS-substrate (GelTrex) following the on-top method. A thin layer of ice-cold GelTrex (about 44 µL/cm^2) was uniformly deposited on a pre-chilled culture dish which was then incubated at 37°C for 15-20 minutes to allow gelation. The total protein concentration of GelTrex varied among different lots, but had a nominal value between 15.4 - 16.0 mg/mL. MCF10A single cells in suspension were seeded on the matrix layer at a density of about 200 cells/mL and incubated in assay medium containing 2% EHS gel. Medium was renewed every 3-4 days. After 9 days of cultivation (with the day of seeding set as day 0) assay medium supplemented with EGF was substituted with EGF-free medium, as this was shown to improve lumen formation efficiency [54].

3.2.4. MDA-MB231 cell culture

MDA-MB231 cells were obtained by ATTC (Manassas) and grown in DMEM/F12 medium having the following composition:

Table 3.3.: Medium recipe for cultivation of MDA-MB-231

MDA-MB-231 medium	
DMEM/F12	ad 500mL
L-Glutamin	1%
FCS	10%
Penicillin/streptomycin	1%

Cells were passaged every 4-5 days upon reaching about 60% confluence. To this end, all media were pre-warmed to 37°C; cells were washed with PBS and incubated at 37°C for about 5 minutes with 2 mL of 0.05 Trypsin-EDTA solution. 2 mL growth medium were added to the suspension which was successively centrifuged at 180 g for 4 min. After elimination of the supernatant, the cell pellet was resuspended in 2 mL of fresh medium and used for experiments or for further cultivation.

3D cell culture of MDA-MB231 acini

The protocol for 3D cell culture of MDA-MB-231 cells was taken from previous publications [106]. The seeding procedure was identical to that for MCF10A cells (about 200 cells/mL were deposited on a thin layer of GelTrex following the on top method). Spheres were cultivated for about 20-25 days in growth medium supplemented with 2% GelTrex in solution, and medium was renewed every 3-4 days.

3.2.5. Isolation of 3D cell cultures from EHS gel and transfer on hard substrates for AFM and SEM characterization

To isolate acini from the GelTrex matrix prior to AFM indentation experiments, samples were first washed with ice cold PBS for 5 minutes, then incubated in cell recovery solution for 45-60 min. The incubation was performed at 4°C given the propensity of the EHS-substrate to liquify at low temperatures. Individual spheres were then carefully pipetted out of the fluid gel matrix under a stereo microscope and transferred in centrifuge tubes treated for minimizing protein binding (Lo-Bind, Eppendorf). 5 min of centrifugation at 4°C and 800 rpm followed. After elimination of the supernatant, the pellet of MCF10A acini (or the MDA-MB-231 3D aggregates) could be resuspended in their respective EGF-free medium and transferred on culture-treated Petri dishes for AFM indentation experiments.

3.2.6. Basement membrane isolation

For basement membrane AFM and SEM characterization, two different isolation protocols were adopted. For spheres up to 12/15 days, after the isolation of acini from the GelTrex matrix, it sufficed to perform one extra round of centrifugation at 13500 rpm (4 min, 4°C). The acinar structures then literally broke apart, leaving in some cases thin BM fragments floating in the supernatant. These could then be carefully pipetted on cell culture-treated Petri dishes or on poly-L-lysine-coated glass (30 min, 37 °C) where they would adhere firmly and be stored for AFM imaging or for SEM probe preparation.

For older spheres, though, centrifugation was not sufficient for isolating the BM. A manual setup for peeling-off of the membrane had therefore to be established. This consisted of two self-produced bent glass microcapillaries that, being controlled via separate micromanipulators (InjectMan and FemtoJet microinjector, Eppendorf), could be employed to immobilize the MCF10A acinus on one end, and break through it on the other end, effectively allowing a partial "peeling" off of BM fragments. For the BM to

be visible, in this case a collagen IV staining had to be performed after the transfer (following the protocol described in Section 3.3.2). An idea of the procedure is given in Figure 3.1.

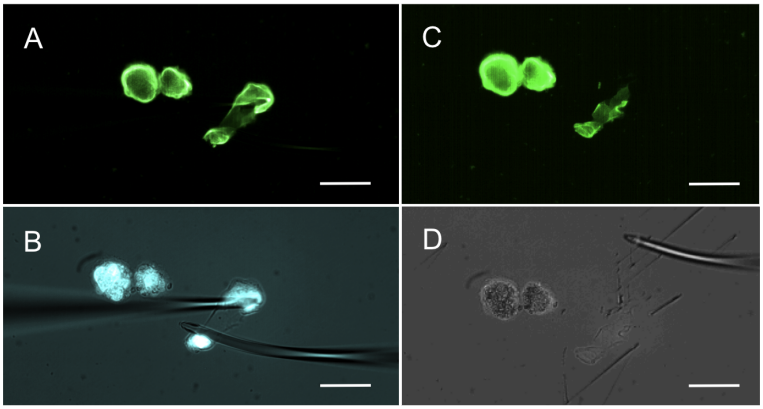

Figure 3.1.: MCF10A spheres isolated from GelTrex and transferred on a culture-treated Petri dish for BM isolation. **A.** In green: collagen IV fluorescent signal staining the BM. **B.** In cyan: CellTracker cytoplasmic dye allowing to verify that single cells were properly removed and only the BM was isolated. In transparency: transmitted light signal showing the micromanipulated capillaries used for peel-off. **C.** In green: collagen IV staining fluorescent signal of the isolated BM fragment. **D.** Corresponding transmitted light signal. Scale bar: 100 µm.

3.3. Light microscopy

Within the realm of light microscopy, one of the main advancements for the field of cell biology has been the introduction, in the early 1900, of fluorescence microscopy. The main advantage of this technique lies in the possibility of specifically labeling different sub-cellular structures with different fluorophores, thanks to the development of antibody-based methods to detect single proteins in a sample (also known as *immunostainings*) [69]. Upon illumination with light of a specific wavelength (λ_{ex}), fluorophores are excited to a higher electronic energy level; when they decay back into their ground state they emit a photon of lower energy (λ_{em}), which can be collected thereby providing information about the fluorophore position within the sample.

3.3.1. LSM: laser scanning confocal microscopy

Contrary to conventional light microscopes, where the whole sample is irradiated at once, in a confocal LSM the specimen is sequentially illuminated in a pointwise fashion.

The introduction of a pinhole along the optical path allows to exclude most out-of-focus light, resulting in increased x and y resolution and a drastic enhancement in contrast; sequential imaging of different focal planes allows precise 3D reconstruction of images. Figure 3.2 offers a schematic representation of the functioning principle of a LSM: a laser beam of a certain wavelength (λ_{ex}) is reflected via a dichroic mirror into a microscope objective and ideally focussed onto a diffraction-limited spot on the focal plane of the sample. Upon excitation, the sample's fluorophores will isotropically reemit light of longer wavelengths, which will then be collected by the objective, transmitted through the dichroic mirror and finally focussed onto the pinhole. The pinhole aperture will only allow photons coming from the focal plane (or, more precisely, the "focal slice") to reach the emission filter and finally the photomultiplier detector [69].

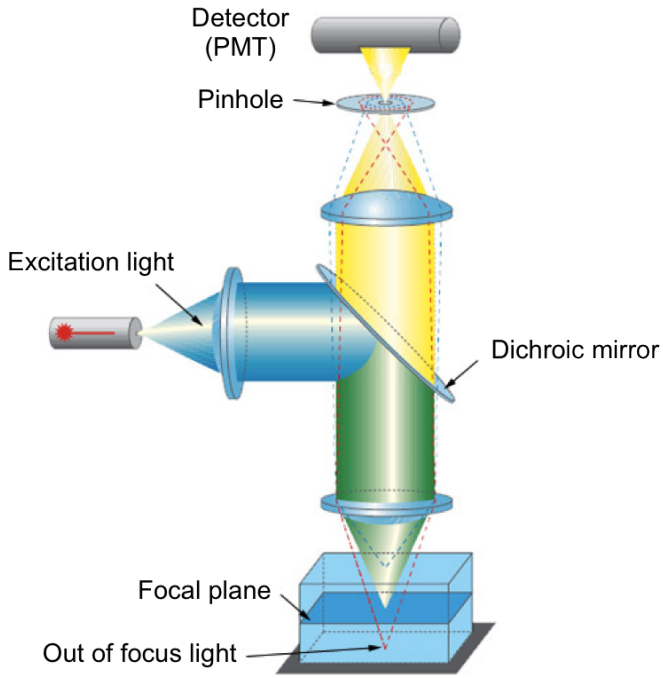

Figure 3.2.: Schematics of the optical path within a confocal laser scanning microscope. Image adapted from [184].

Superresolution Airyscan

The Airyscan (Zeiss) is an array detector allowing to produce images with increased signal-to-noise ratio and resolution by introducing many single detector elements acting as sub Airy pinholes. In standard confocal microscopy, when closing the pinhole to

reject out-of-focus light, part of the signal gets lost. This classical tradeoff between resolution and photon counting can be minimized by imaging the complete Airy disk on a concentrically arranged hexagonal detector array consisting of 32 single elements. Image acquisition takes place while the pinhole remains completely open, hence no photons are lost, and reassignment of the signals from all detector elements to their correct position allows image reconstruction [72].

Microscope settings and objectives

In this work, an LSM 710 (Carl Zeiss) and an LSM 810 with Airy scan (Carl Zeiss) were used in combination with different objectives. Live cells or multicellular structures were imaged under physiological conditions (37°C, 5% ambient CO_2), while fixed cells were imaged at RT. An overview of all the objectives used for the different experiments is given in the following table.

Table 3.4.: List of objectives (Carl Zeiss)

Plan-Neofluar air (10x/0.3)
EC Plan-Neofluar oil Ph3 (40x/1.3)
Antiflex EC-Plan Neofluar oil (63x/1.25)
LD Plan-Neofluar Ph2 corr M27 air (40x/0.6)
Epiplan air (50x/0.7)
C-Apo w autocorr M27 (40x/1.2)
LD C-Apochromat w corr M27 (63x/1.15)
Plan-apochromat with Airy scan performance oil (63x/1.4)

3.3.2. Immunofluorescence staining protocols

Immunofluorescence staining on keratinocytes

A quick overview of all the solutions required during the immunofluorescence staining of WT, KO and RES keratinocytes is given in the following tables.
Immunostainings of the intermediate filament network were performed on keratinocytes in order to characterize the keratin distribution in WT and RES cells, and confirm their absence in KO cells. To this end, cells were seeded at a density of about 5000/cm^2 on

Fixating solution (3.7% Paraformaldehyde)	
37% Paraformaldehyde stock	1 mL
CB buffer	9 mL

Glycine solution (30 mM)	
Glycine	0.1126 g
CB buffer	ad 50 mL

Permeabilization solution (5% Triton-X-100)	
Triton-X-100	500 µL
CB buffer	ad 10 mL

Blocking solution	
Skim milk powder	0.1 g
CB buffer	ad 10 mL

Dilution buffer
1% BSA in PBS

round coverslips (diameter: 24 mm, thickness: 170 µm) coated with collagen I (0.0475 mg/mL in acetic acid). After 24 h for single cells, and at least 48 h for monolayers, medium was removed and cells were washed with PBS prior to fixation via the methanol/acetone method: keratinocytes were incubated with -20°C cold methanol for exactly 3 minutes, and with -20°C cold acetone for exactly 20 seconds. Cells were then incubated with a 1:200 solution of primary antibody in dilution buffer for 1h at 37°C. Three washing steps (10 min, PBS) preceded incubation with the secondary antibody (1:100 in dilution buffer, 1 h, 37°C). The antibody combinations, along with the additional fluorescent dyes used, are listed in Table 3.5.

To characterize the microfilaments network, actin was stained with phalloidin: after a CB washing, cells were incubated in fixating solution for 20 minutes at 37°C. The solution was then removed and cells were washed with a 30 mM glycin/CB solution. Permeabilization of the plasma membrane was carried out via a 2 min incubation in 5% TritonX-100 solution in CB. Three additional washing steps in CB followed (5 min, RT),

Table 3.5.: Antibodies and dyes used for immunostaining of keratinocytes

Primary antibodies	Supplier
Polyclonal anti-keratin PAN (rabbit)	Progen Biotechnik GmbH
Anti desmoplakin 1,2 (guinea pig)	Magin Laboratory
Secondary antibodies	
Cy2 goat anti-rabbit	Jackson ImmunoResearch Laboratories
Alexa Fluor 633 goat anti-rabbit	Invitrogen
Alexa Fluor 633 donkey anti-goat	Invitrogen
Fluorescent dyes	
Alexa Fluor 488 phalloidin	Invitrogen
Alexa Fluor 633 phalloidin	Invitrogen

and finally keratinocytes could be incubated in a phalloidin solution (1:200 in blocking solution, 1 h, 37°C).
For both staining methods, after one final step of PBS washing the samples were coverslipped via 20 µL FluoroMount medium mixed with DABCO (5 µg/mL).

Immunofluorescence staining on MCF10A acini.

A quick overview of all the solutions required during the immunofluorescence staining of MCF10A acini is given in the following tables.

Fixating solution (2% formaldehyde/0.5% glutaraldehyde)	
37% formaldehyde stock	0.54 mL
25% glutaraldehyde stock	0.4 mL
CB buffer	9.06 mL

Quenching solution	
$NaBH_4$ in CB buffer	10 mg/mL

Glycine solution (30 mM)	
Glycine	0.1126 g
CB buffer	ad 50 mL

Permeabilization solution (1% Triton-X-100)	
Triton-X-100	100 µL
CB buffer	ad 10 mL

Blocking solution	
Skim milk powder	0.5 g
CB buffer	ad 10 mL

Dilution buffer
1% blocking solution in CB buffer

MCF10A acini in gel were stained according to the following protocol: after a washing step in CB, samples were incubated in a fixating solution for 20 minutes at RT. After fixation, a quenching step was performed with 1% $NaBH_4$ in CB for 5 minutes at RT. A washing step with the 30 mM glycine solution followed (5 min, RT), after which the membrane was permeabilized with 0.5% Triton X-100 solution (for spheres up to 15 days) or 1% Triton X-100 solution (for spheres older than 15 days) in CB for 20 minutes at RT. After an additional washing step (5 min in CB, RT), unspecific binding was blocked by incubation in blocking solution for 2 hours at RT. Incubation with primary antibodies was performed overnight at 4°C by means of a 1:200 antibody solution in dilution buffer. Three washing steps in dilution buffer followed (5 min, RT); at this point, the secondary antibodies solution (1:200 in dilution buffer) could be incubated for 45 minutes at RT. In case of additional nuclear co-stain, after 2 final washing steps in CB (5 min, RT), a solution of 5 mM Draq5 in CB was allowed to incubate for 10 minutes at RT (in dark). After aspiration of the solution and addition of fresh CB, the sample was ready to be analyzed. The antibody combinations, along with the additional fluorescent dyes used, are listed in Table 3.6.

Table 3.6.: Antibodies and dyes used for immunostaining of MCF10A acini

Primary antibodies	Supplier
Ploryclonal Collagen type IV-Biotin (rabbit)	abcam
Monoclonal laminin 5 (γ2 chain): clone D4B5 mouse anti-human	Merck Millipore
Secondary antibodies	
Avidin Alexa Fluor 488 goat anti-rabbit	ThermoFisher Scientific
Mouse IgG (goat) Alexa Fluor 546	ThermoFisher Scientific
Fluorescent dyes	
Alexa fluor phalloidin 488	Invitrogen
Cell Tracker Orange CMTMR Dye	Molecular Probes
DRAQ 5	Cell Signalling Tech.

Live MCF10A acini analyzed via AFM-like experiments at the confocal setup were stained according to the following protocol: after isolation from the EHS gel as described in Section 3.2.6 and transfer on culture-treated imaging dishes (µ-Dish^{35mm}), spheres were carefully washed with a 5% solution of milk powder in PBS (10 min, RT), then incubated with a 1:500 solution of Collagen IV-biotin in a 1% solution of milk powder in PBS (45 min, 37°C). Washing with the same 1% milk powder/PBS solution followed (3x, 5 min, RT) before the secondary antibody (Avidin Alexa Fluor 488) and the cytoplasmic dye (Cell Tracker Orange) were added (1:200 and 1:1000 in 1% milk powder/PBS, respectively). The solution was again incubated for 45 min at 37°C. At this point, after a washing step in PBS, spheres immersed in EGF-free medium were ready for analysis.

Pore size finding algorithm

To determine pore size of the collagen IV meshwork in isolated MCF10A spheroids, the following algorithm developed by G. Dreissen (ICS-7) was employed: Z-stacks of immunofluorescence staining images were smoothed via a binomial filter of size (5 × 5 × 3 pixels with pixel size: 0.21 × 0.21 × 0.22 µm^3). Then, the MatLab function imopen was used to perform a morphological opening; images were successively contrast inverted and a mask of the pores was obtained using the method for identifying focal adhesions

published in [73]. Masks of different focal planes were finally superimposed in order to display the full pore distribution and the areas of individual pores were calculated via the MatLab function regionprops.

3.3.3. RICM: reflection interference contrast microscopy

Reflection interference contrast microscopy is a technique allowing to determine a specimen's shape and distance from the flat, reflective surface of a coverslip with a very high precision thanks to the interference pattern created by the reflection of light from both the surface and the investigated object itself [185]. In the setup, before reaching the sample, linearly polarized light is guided through a $\lambda/4$ quarter wave plate that converts it into circularly polarized light of a certain handedness. The transmitted light that travels through the coverslip into the object placed on top of it (for example, an adhering cell) will be reflected with an inversion of the circular polarization handedness and a shift in phase caused by the difference between the refractive indices of the two optical media; this phase shift is proportional to the distance between the glass and the cell. The reflected light then travels back to the $\lambda/4$ quarter wave plate, and finally crosses a second polarizer, which is rotated of 90°with respect to the first one in order to prevent stray light from reaching the detector. RICM analysis was performed on an Axiovert 200 equipped with an Antiflex EC-Plan Neofluar 63x oil objective with a numerical aperture of 1.25 (Carl Zeiss) in order to analyze the surface topography of the silicon microbeads glued to the AFM cantilevers to be used as indenters in keratinocytes force spectroscopy experiments.

3.3.4. Dextran permeation assay

For in situ permeation assays, MCF10A acini were isolated from GelTrex according to the protocol described in Section 3.2.6, transferred onto GelTrex coated ($8\,\mu L/cm^2$) glass bottom dishes and let to adhere for 20 minutes. Medium was premixed with the respective dextran tracer before imaging started. TexasRed-conjugated dextrans of different molecular weights and concentrations (3 kDa: $133\,\mu g/mL$, 10 kDa and 40 kDa: $200\,\mu g/mL$, $\lambda_{Ex}/\lambda_{Em} = 585/905$ nm) were used.
Dextran signal was recorded every 1.5 minutes for the first 30 minutes, and every 8 minutes for the next 5 hours. At least 15 acini were analyzed for each group in at least three independent experiments. These experiments were performed by A. Gaiko-Shcherbak (ICS-7).

Collagenase IV assay

Acini were washed with Hank's Balanced Salt Solution (HBSS) and incubated with a solution of 290 U/mL of collagenase IV in HBBS for 3 hours at RT. Subsequently, dextran permeability assays were performed as described in Section 3.3.4.

Image processing masking algorithm

To isolate the fluorescence intensity profiles of MCF10A spheres during dextran permeation analysis, a masking algorithm was implemented in Matlab thanks to the help of G. Dreissen (ICS-7). Acinar domains were isolated from the background according to the following algorithm: first, all fluorescent images were median filtered with a filter size of 35 × 35 pixels (pixel size: 0.323 × 0.323 µm^2), leading to a smooth image divided into a background and a foreground (corresponding to the sphere). To extract the acinar boundary, the gradient of the filtered image was calculated using Matlab's Imgradient-function (Prewitt method). The boundary of the sphere was then identified by masking the gradient image with its mean gray value as a threshold (to avoid border artifacts, the 20 outer pixels of the whole mask were set to zero). In the next step, holes within the mask were filled and morphological closing was performed. In case more than one structure was found, the one chosen to be the current sphere mask was always the largest one.
The surface thereby identified still included the brighter basal membrane surrounding the sphere. To just analyze the fluorescent signal of dextrans penetrated through the BM and into the intracellular space, this needed to be removed. To do so, the mean gray value of the image covered by the mask was again used as a threshold: all pixels having a gray value higher than the threshold were therefore discarded. A new step of morphological closing and holes filling allowed to obtaining the final sphere mask (see Fig. 3.3 B). The mean fluorescent intensities of low-matured MCF10A acini were analyzed based on this mask. The semi-matured acini, in contrast, needed an additional step of analysis prior to data evaluation, because of the high autofluorescence caused by apoptotic cells in the sphere's interior. In this last step, the median of the grey value distribution of the image covered by the final mask was used as a threshold to isolate the very bright domains (i.e., each pixel brighter than the median): such pixels were discarded as autofluorescence, and the remaining part was analyzed (see Fig. 3.3 D, yellow domains). To determine the background intensity, ROIs (Region Of Interest) were manually marked at positions of the image that remained unchanged and free of defects throughout the observation period. The median gray values of these ROIs were

then calculated for each time frame and used to normalize the sphere's signals.

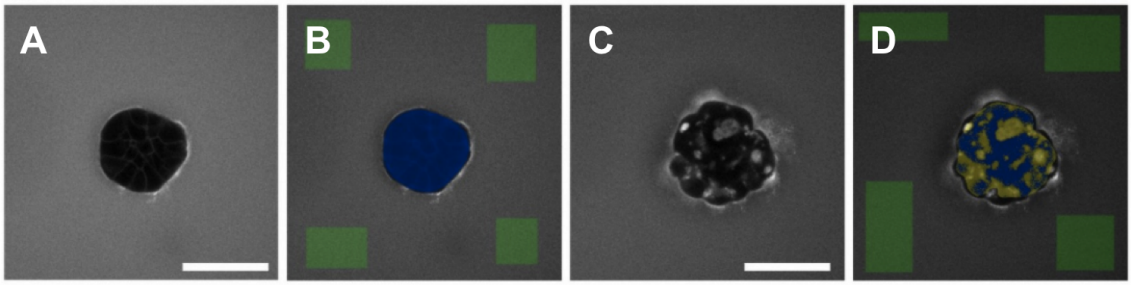

Figure 3.3.: Representative images of MCF10A acini before and after implementation of the masking algorithm used for permeation analysis. **A**. Florescent signal of TexasRed labelled dextrans permeating through the BM of a low-matured MCF10A sphere isolated from the GelTrex matrix and (**B**) in blue: mask used to measure the fluorescence intensity profile inside the acinus. In green: manually selected ROIs used for background calculation. **C**. Fluorescent image of an isolated semi-matured MCF10A sphere and (**D**) corresponding mask. In yellow: domains identified by the masking algorithm as autofluorescent, and therefore discarded from the analysis. Scale bars: 50 µm.

3.3.5. MCF10A detergent-induced decellularization assay at the LSM

MCF10A acini at different degrees of development (low-, mid- and highly-matured) were treated with octyl-β-D-glucopyranoside (OGP) detergent in order to induce decellularization and detachment of cellular substructures from the BM (see Fig. 5.7 E). Prior to incubation in OGP, reference images of all analyzed spheres were recorded. Live cell imaging started upon addition of a 1% OGP solution in PBS. Images were taken every minute during the first 30 minutes, and every 5 minutes for the following 5 hours. Subsequently, acini were fixated for further immunofluorescence staining analyses. These experiments were performed by A. Gaiko-Shcherbak (ICS-7).

3.4. AFM: atomic force microscopy

3.4.1. Probe selection and modification

In order to perform force spectroscopy experiments on live cells, cantilevers should be flexible and capable of very soft indentations. In practice, probes with a spring constant similar to that of measured substrate (around 0.02 N/m) are often preferred, since much stiffer cantilevers just would lack the sensitivity necessary to such measurements. In order to maximize the laser signal acquisition, AFM cantilevers are often back-coated with this layers of reflective metals, like silver or aluminium. Given the strong sensibility of live cells to ions of such metals, though, it is preferable to work with coatings of inert materials like gold. For these reasons, tipless cantilevers of the series Arrow-TL1Au with Ti/Au back tip coating (Nano World) with a nominal elastic constant k of 0.04 N/m and a resonance frequency f_0 of 7 kHz were chosen. To avoid the risk of damaging cell membranes by the use of sharp tips [174], spherical silica probes with nominal radius of 5 µm (G.Kisker GbR, PSI-5.0, surface plain) were glued to the cantilever extremity by means of bicomponent glue (UHU plus Endfest 300) and successively used as indenters for single cell elasticity measurements. The exact sphere radius was measured using a LD Plan Neofluar Ph2 (40x/0.6) air objective. For MCF10A acini, glass microspheres with a nominal radius of 30-50 µm were chosen (Polysciences Inc.). Typical images of tipless cantilevers modified for single cell (Fig. 3.4 A) and for MCf10A acini (Fig. 3.4 B) indentation experiments are given below.

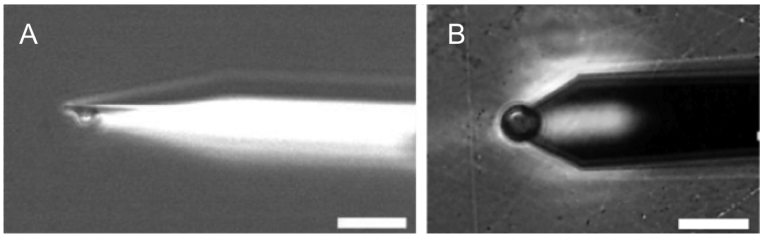

Figure 3.4.: A. Side view phase contrast image of a cantilever modified by attachment of a glass sphere of radius R = 5 µm. Scale bar: 50 µm. **B.** Top view phase contrast image of a cantilever modified by attachment of a glass sphere of radius R = 25 µm. Scale bar: 100 µm.

3.4.2. Calibration

In order to measure force values accurately, it is crucial to know the cantilever's spring constant k. In principle, if the cantilever's exact geometry and material parameters are

known, the theoretical values for k can be computed analytically, and are in fact typically provided for every commercially available cantilever along with the nominal resonance frequency f_0. But the small inhomogeneities arising from the production process are the cause of extremely large variations among the effective spring constant of different cantilevers: therefore it becomes necessary to perform individual calibration experiments before proceeding with any AFM measurement. To this end, different methods can be followed [177]. The simplest and most precise system, routinely used by the majority of AFM users, is without doubt the thermal calibration method [188].
Let us approximate the cantilever to an harmonic oscillator with one degree of freedom of elastic potential energy:

$$\frac{1}{2}m\omega_0^2 < z^2 >= \frac{1}{2}k < z^2 > \tag{3.1}$$

where m is the cantilever's mass, ω_0 its resonant angular frequency, k its spring constant and $< z^2 >$ the mean square displacement caused by thermal motion. This quantity is nothing but the expectation value of z^2 as measured over a long time interval t:

$$< z^2 >= \lim_{t\to\infty} \frac{1}{t} \int_{-t/2}^{t/2} z^2 dt \tag{3.2}$$

Now, the equipartition theorem states that an average thermal energy of $\frac{1}{2}k_BT$ (with k_B the Boltzmann's constant) can be attributed to each quadratic term of a system's Hamiltonian. Therefore, in a one-dimensional case, since $\omega_0^2 = k/m$ we can write:

$$\frac{1}{2}k < z^2 >= \frac{1}{2}k_BT \tag{3.3}$$

This means that by measuring the temperature T and the variance of the cantilever's position over time $< z^2 >$ we will be able to estimate the spring constant k.
In practice, first of all a force spectroscopy cycle is performed on a hard surface in order to determine the optic system sensitivity S [nm/V], which is taken as the inverse of the slope of the force curve.
Then, the tip's Brownian motion is tracked over time by recording the lasers' displacement on the photodiode: its power spectral density P_f (in units of pm^2/Hz or $\mu V^2/Hz$) typically follows a Lorentzian function centered around some resonant frequency:

$$P_f = \frac{D/(2\pi^2)}{(Q/f_0)^2(f_0^2 - f^2)^2 + f^2} \tag{3.4}$$

where f_0 is the characteristic frequency of the cantilever ($f_0^2 = k/(4\pi^2 m)$), $D = k_BT/\gamma$

(with γ the friction coefficient of the medium) and Q the cantilever's quality factor ($Q = \sqrt{mk}/\gamma$) [176]. Upon fitting this function and integrating it around the resonance peak one can compute the expectation value of the fluctuations over time $< z^2 >$, which is nothing but the area below it. Provided that all other parameters in Equation 3.3 are known, this allows to determine k.
Usually the first resonance is used, but for very soft cantilevers immersed in liquids this typically lies around 1-3 kHz: in this low frequency range, the first peak can be affected by noise, as can be seen from Figure 3.5. Therefore, the second resonance peak is used as it provides more reliable results [71].

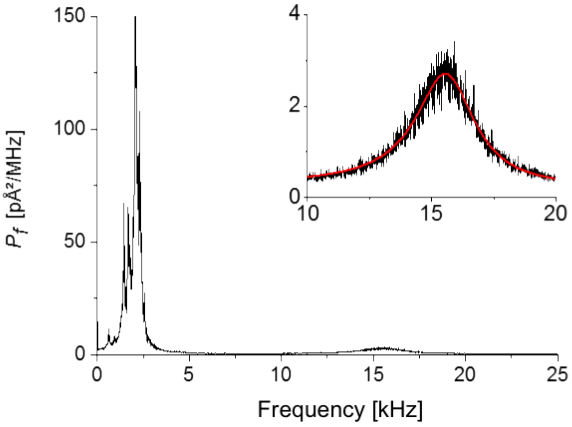

Figure 3.5.: Power spectral density of the tip-modified cantilever (series Arrow-TL1Au, Nano World) used during all indentation experiments performed on MCF10A acini (indenter radius R = 22.32 µm). The calibrated k was 0.091 N/m. Inset: zoom-in of the second resonance peak measured in liquid and used to compute the expected value of the Brownian fluctuations over time. In black: recorded data. In red: fit of Eq. 3.4.

3.4.3. AFM specimen preparation, imaging and force spectroscopy settings.

All AFM measurements were performed on a Nanowizard Life Science version instrument (JPK) equipped with an inverted optical microscope (Axiovert 200) for sample observation. A GFP fluorescent channel in the microscope allowed to visually control the presence of a keratin network in all the RES keratinocytes analyzed. For single cells elasticity measurements, 16 h before experiments about $12{\cdot}10^3$ cells were seeded on coverslips (thickness: 170 µm) coated with collagen I (0.0475 mg/mL in acetic acid); for measurements on cell monolayers, an extra 24 h were allowed for cell proliferation.

Measurements on single cells were performed in collaboration with L. Ramms (ICS-7), and, on cell clusters, with T. Marković (ICS-7).
Prior to the beginning of measurements, these were washed once with PBS and inserted in the Biocell chamber (JPK), where cells were immersed in 400 µL HEPES-buffered medium (20 mM). Only single, adherent and evenly spreading cells were analyzed.
Indentation experiments were performed at RT always using the same cantilever (k=0.04 N/m and f_0=7 kHz) of the Nanoworld Arrow-TL1Au with Ti/Au back coating modified through attachment of a silica bead of R=4.3 µm. To allow for thermal equilibration, the experiments were started only 10-15 minutes after medium exchange. Tip calibration was repeated before each experiment. During indentation cycles, the spherical indenter was pressed on top of the cells on the nucleus and at the cell body.
Tip velocity was fixed at 1.5 µm/s, and the maximal forces exerted (i.e. the force setpoint values) were of 1.48 nN above the nucleus and 0.5 nN above the cell body. In each position at least three consecutive curves were recorded to exclude the presence of plastic deformations. For actin depolymerization control experiments, WT and KO keratinocytes were incubated with 0.5 µM latrunculinA (latA) in medium (1 h, 37°C).
AFM imaging of single cells and isolated basement membranes, as well as BM force maps were performed using silicon tips (Nanosensor point probes-CONT-50) of nominal resonance frequency f_0 = 10-17 kHz and nominal spring constant k = 0.07-0.4 N/m. Images were processed using the JPK DP software.

Indentation experiments on MCF10A and MDA-MB-231 acinar structures were performed according to the following protocol: spheres were isolated from the GelTrex matrix as described in Section 3.2.5 and seeded on culture-treated Petri dishes (VWR). 400 µL HEPES-buffered EGF-free assay medium (20 mM) were added, and the system was allowed to thermally equilibrate for 30-45 min prior to experiments. Only rounded, normal-looking acini were analyzed. All indentation measurements were performed with the same Nanoworld Arrow^{TM}-TL1Au with Ti/Au back coating modified through attachment of a glass bead of R=22.32 µm. The calibrated k was 0.091 N/m (see Fig. 3.5). During indentation cycles, the spherical indenter was pressed on top of the 3D cell structure in correspondence of the center. Tip velocity was fixed at 2 µm/s, and the force setpoint value was of 40 nN. In each position at least three consecutive curves were recorded to exclude the presence of plastic deformations.
For comparison of native and decellularized MCF10A spheres, after completion of the measurements, acini were incubated in a 1% solution of OGP in medium (45 min, 37°C) to promote decellularization and then measured again. At least three force curves were

recorded on each native and OGP-treated sphere analyzed.

AFM images data processing

Processing of all topographical images recorded at the AFM was performed using the JPK-DP software (version 4.3.46). For comparison of the BM thickness, all images were subject to the same set of operations: first, a polynomial fit was subtracted from each scan line independently. Then, a polynomial surface was fitted through one or more rectangular regions chosen from the flat background and successively subtracted from the whole image (in both cases, a polynomial of degree = 1 was chosen, corresponding to a plane fit). Finally, histograms of pixel values were saved and analyzed via Gaussian fitting as shown in Section 5.4.1.

3.4.4. Contact point determination algorithm

It is well known that the determination of the contact point plays a crucial role for an accurate estimation of substrate's elasticity. For example, misidentifying its position of just 50 nm can lead to more than an order of magnitude difference in E values when calculated over the first 200 nm of the indentation curve [186]. A conspicuous body of literature presents methods for automatic and reliable contact point determination (amongst others, see [186]-[175]). Here, we chose to use the following MatLab-implemented algorithm, developed by Dr. R. Springer (ICS-7): at first, data were smoothed by dividing the curve in 100 intervals and averaging data points in each of them. With an acquisition rate of 5000 Hz, indentation curves typically contained about $10\text{-}15 \cdot 10^3$ data points, leading to a block size of 100-150 data points. Then, the third derivative of the reduced curve was calculated, and its maximum was identified.
Just in analogy to how the first derivative describes a curve's steepness, and the second derivative follows its curvature, the third derivative shows "how quickly" the curvature is varying, therefore its maximum will identify the knee-point we observe after the curve's baseline (see Fig. 3.6). Therefore, a neighborhood of this maximum consisting of 50 recorded values was averaged, and the resulting distance-coordinate was taken as that of the contact point. The last step consisted in the rescaling of the curve so that indentation and force values at the contact position would equal zero.

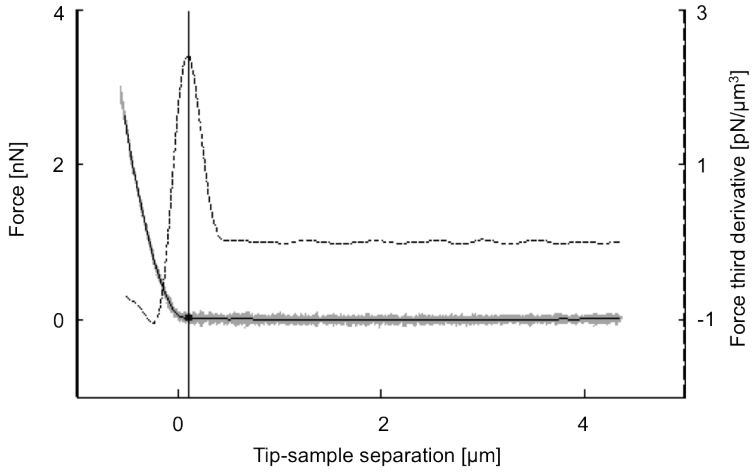

Figure 3.6.: Plot showing the contact point identified on a typical AFM indentation curve as the maximum of the curve's third derivative. Gray line: original data; dark gray line: smoothed data used for calculation; dashed line: third derivative. The zero of tip-sample separation axis corresponds to the contact point as identified by the JPK-DP software.

3.4.5. AFM force-indentation curve fitting

Fitting of AFM force-indentation curves according to the power-law model (for keratinocytes) and to the Fung, Ogden and Mooney-Rivlin hyperelastic models (for 3D cell structures) were performed via a MatLab implemented routine using the lsqcurvefit function and the Levenberg-Marquardt algorithm for least squares curve fitting. The squared norm of residuals was used to compare fit efficiency within any given data group. The fit range was selected as starting from the contact point (determined according to the protocol described in Section 3.4.4). The Poisson's ratio was fixed to ν=0.5 for keratinocytes and to ν=0.49 for MCF-10A and MDA-MB-231 spheroids.

3.4.6. Statistical analysis

AFM force distributions, fitted Young's moduli and material parameters, as well as permeation time constant distributions, were analyzed via the two-tailed nonparametric unpaired Wilcoxon signed-rank test (95% confidence interval). Throughout the results chapters, in case the experimentally obtained parameters were normally distributed, mean values ± standard deviation are presented. For log-normally distributed data, though, the median and multiplicative standard deviation σ^* are reported.
These parameters should be interpreted as follows: given a data set (X), this is log-normally distributed if log(X) is normally distributed. The logarithmized data set is

therefore characterized by a mean value μ and a standard deviation σ. Upon back transformation, e^{μ} will correspond to the median of the log-normal distribution (we call it med(X)) and e^{σ} will correspond to a multiplicative standard deviation which determines the distribution shape (we call it σ^*). For further details on the treatment of log-normal distributions, see [92].
Throughout the work, when box plots are presented, the bottom and top of the box represent the first and third quartiles, while the band inside is the median distribution value. Whiskers indicate distribution outliers. When shown, minimal and maximal values are represented by horizontal bars (-) and the 1% and 99% confidence intervals by crosses (×). All analyses were performed with Origin (9.0) software (OriginLab Corporation), R (version 2.155.3) and MatLab (R2015a) software (The MathWorks, Inc.).

3.4.7. AFM-like indentation experiments at the LSM

For observing the large-indentation behavior of MCF-10A acini, Z-stacks of isolated live cellular spheroids were recorded while the latter were being indented by AFM tips built in a confocal setup. Shortly, calibrated AFM tips modified by the attachment of glass microspheres with a nominal radius of 30-50 µm (Polysciences Inc.) were glued to glass microcapillaries via bicomponent glue (UHU plus Endfest 300). The holder chip was kept at an angle of about 30°with respect to the capillary to facilitate successive handling. Upon glue drying (after at least 24 h), the glass capillaries were carefully inserted in a micromanipulator (InjectMan, Eppendorf) built at the LSM setup which allowed for manual control of the AFM cantilever's z position.
MCF-10A acini were isolated from the EHS-matrix gel as described in Section 3.2.5 and transferred on glass coverslips precedently coated with Poly-L-lysine (30 min incubation at 37°C). At this point they were stained according to the protocol described in Section 3.3.2; after fresh medium addition, they could finally be inserted in the microscope and probed by AFM-like indentation. To get at least an estimate of the force exerted while lowering the AFM tip onto the acini by means of micromanipulator-driven indentation, Z-stacks of the whole cantilever were recorded using the microscope reflection channel. Knowing the calibrated value of the cantilever's spring constant k, and having images of its deflection, we could estimate the force exerted during indentation. The execution of these experiments was highly facilitated by the precious technical assistance of N. Hampe (ICS-7).

MCF-10A acinar volume calculation

Based on the Z-stacks recorded at the LSM during AFM-like indentation experiments, the volume of MCF-10A spheres at different stages of indentation was computed thanks to a MatLab routine developed by G. Dreissen (ICS-7). In each focal plane, at first the search area was manually identified; then, image smoothing was performed using a median filter of 5×5 pixels (pixel size: 0.497×0.497 µm^2 or smaller). At this point, the MatLab function activecontour was used to segment the object in a background and a foreground starting from the initial search domain. The number of pixels enclosed in each foreground mask was computed, summed up, and finally multiplied by the voxel size in order to obtain the sphere's volume.

3.5. SEM: scanning electron microscopy

As their name suggests, scanning electron microscopes do not rely on light, but rather on the point-wise interaction of electron beams with the atoms of a sample to form an image. It is well known that different kinds of electron-matter interactions are possible; for instance, upon arrival on a specimen's surface, electrons can undergo *elastic scattering* (meaning that the kinetic energy and velocity are conserved), resulting in backscattered electrons (BSE). Or they can lose energy through the interaction with the specimen (*inelastic scattering*), resulting in a plethora of possible phenomena: amongst others, the ejection of Auger electrons from the outer orbitals, the excitation of phonons leading to heating or the production of characteristic X-ray and continuum radiation (Bremsstrahlung). One of the most important interactions, for SEM imaging, is the generation of secondary electrons (SE), particles that are displaced and literally kicked out of the specimen by the primary electron beam. Such signals contain information regarding a sample's topography and composition.
SE (or BSE) are therefore collected by an electron detector, converted to photons by a scintillator, and then turned into electric signals in order to map their intensities into an image. Due to the very short wavelength of electrons, the resolution of a SEM image can be down to less than 1 nm [183].

SEM specimen preparation and imaging settings

For the preparation of endogenously expressed MCF10A acinar basement membranes, the latter were isolated as described in Section 3.2.5 and transferred on glass coverslips precedently coated with Poly-L-lysine (30 min incubation at 37°C). After a Triton-X 100

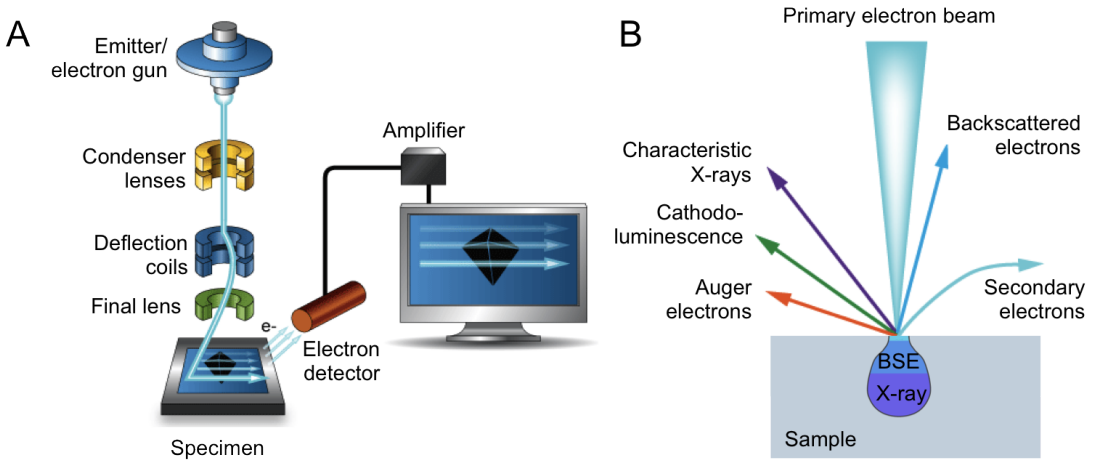

Figure 3.7.: A. Schematics of SEM. **B.** The sample's volume involved in the production of SE, BSE and X-rays takes the shape of a tear-drop whose depth and form depend on the specimen atomic number as well as on the energy of the incoming electron beam. Image adapted from [183].

washing step (0.5% solution in PBS, 5 min at RT), BMs were fixated for 20 min at RT in 3D fixating solution and then washed with PBS 3 times (5 min, RT). Dehydration in a graded series of ethanol in ultra-pure water proceeded through the following dilution steps: 10%, 30%, 50%, 70%, 90%, 95% (3 times), 100%. Each ethanol dilution was incubated for 5 min at RT, and was substituted quickly making sure the sample never dried out. The coverslips were then stored in pure ethanol (100%) until critical point drying, which was performed at a Bal-Tec CPD 030 instrument.

First, samples in ethanol were cooled down to 10°C; then the drying agent (liquid CO_2) was admitted into the chamber. A series of draining and filling cycles was performed until only liquid CO_2 was present. The sample was then heated up to the critical temperature and pressure of CO_2 (31.1°C and 73.8 bar, respectively), conditions at which the liquid medium changed to a gaseous phase; the sample could at this point be removed from the chamber.

Next, BM samples were sputtered with platinum/palladium (Pt/Pd) at a Cressington 208 HR sputter coater with MTM-20 thickness controller unit. Using a current of 60 mA and a vacuum pressure of $3{\cdot}10^{-2}$ mbar, a layer of about 2 nm was deposited on the samples. Imaging was performed on a Gemini 500 Zeiss SEM. The acceleration voltage (EHT) was held between 3 and 10 kV, and the signal analyzed was composed of secondary electrons collected via an in-lens detector.

3.6. Finite elements simulations

All FEM simulations were performed using the FEBiO software suite (including PreView 1.16.0 for model building, FEBiO 2.1.0 for FEM simulations and PostView 1.7.0 for results inspection). The system's geometry was set up in the following way: in all cases, the AFM indenter was modeled as a rigid sphere of radius R=22.3 µm; the MCF10A acini were described as full spheres of different radii in case of the low-matured (R=50 µm) and the semi-matured group (R=60 µm). The highly-matured group was instead modeled as a hollow sphere of outer radius R=51 µm and shell thickness of 15 µm. The acinar dimensions were chosen according to the experimentally measured ones (average values of the distributions for each age group).
All elements were modeled using hexahedral mesh of different sizes. The MCF10A acini laid on a rigid squared bottom slide. The contact of the acinus with the rigid indenter and the rigid plate was defined as a sliding contact (i.e. the two surfaces were not allowed to penetrate) characterized by the parameters listed in Table 3.7. A fixed contact point (for which no displacement nor rotation in x, y and z was allowed) was defined between the MCF10A acinus and the bottom plate along the spheres' z-symmetry axis. Similarly, the bottom plate was described as a fixed rigid body and the acinus was prevented from rotating. Indentation was simulated by imposing a prescribed rigid movement of 5 µm along the z-direction to the rigid indenter.
In the case of the simulation including a basement membrane, the latter was modeled as a thin shell of 800 nm thickness contacting the outer cellular shell via a tension-compression interface type: this describes a sliding interface that may optionally sustain tension. The contact definition parameters are listed in Table 3.7. The BM was described as an elastic material of parameters E=5 kPa and ν=0.49. In this case, an extra constraint was added to prevent rotation of the cells.

Table 3.7.: Parameters used for contact definition in FEM simulations

Sliding interfaces parameters definition	
Argumented Lagrangian	No
Argumentation tolerance	0.2
Penalty	$4.2 \cdot 10^9$
Two pass	No
Auto-penalty	No
Friction coefficient	0
Search tolerance	0.01
Contact type	Facet-on-facet
Tension-compression interface parameters definition	
Argumented Lagrangian	Yes
Argumentation tolerance	0.2
Gap tolerance	0
Penalty factor	$1 \cdot 10^8$
Two pass	No
Auto-penalty	No
Projection tolerance	0.01
Symmetric stiffness	Yes
Search radius	1
Tension contact	Yes

4. Results: keratinocytes elasticity analysis

In this chapter, the elasticity analysis of wild type, keratin knock-out and keratin rescue epithelial keratinocytes is presented. In order to understand the role played by keratin intermediate filaments in determining the mechanical properties of such cell lines, in a first step of analysis the keratin networks were characterized by means of immunocytochemical stainings; successively, AFM indentation experiments revealed the material response of single cells as well as of cell monolayers. The limitations of the traditional approach used for quantifying cellular elasticity (namely, the Hertz model) are explored, and an alternative approach of analysis is proposed. A number of control experiments that help validating the reliability of the results is finally reported.

4.1. Structure of keratin network in wild type, knock-out and rescue keratinocytes

In order to assess the role played by the keratin network in determining the mechanical properties of wild type (WT), knock-out (KO) and K14 rescue (RES) epidermal keratinocytes, the first fundamental step was very simply that of characterizing the network morphology in the different cell lines. To this end, immunocytochemical stainings based on the recognition of basic cytokeratins K1, K4, K8 and K14 by anti-keratin PAN antibodies were performed according to the protocol described in Section 3.3.2. Micrographs of the network structure are shown in Figure 4.1. WT cells showed homogeneously distributed, finely ramified keratin filaments spanning the whole cytoplasm and creating a network that gets denser around the nucleus. In KO cells, in contrast, no single filament could be identified under the same microscope acquisition settings. Only through a higher laser intensity and prolonged illumination times could a very faint diffused signal be identified, indication that the basic keratins still expressed by the cell were present as aggregates but they were incapable of building up filaments in absence of their acidic dimerization counterparts.

RES cells showed a restored keratin network that in first instance was comparable to that of WT cells, but to a closer observation appeared more heterogeneous and less uniformly distributed. In particular, in the majority of cells observed, the RES networks were less compacted and had a larger mesh size than the WT ones; this difference possibly hints at the absence, in K14 cells, of some genetic component necessary for a complete network formation.

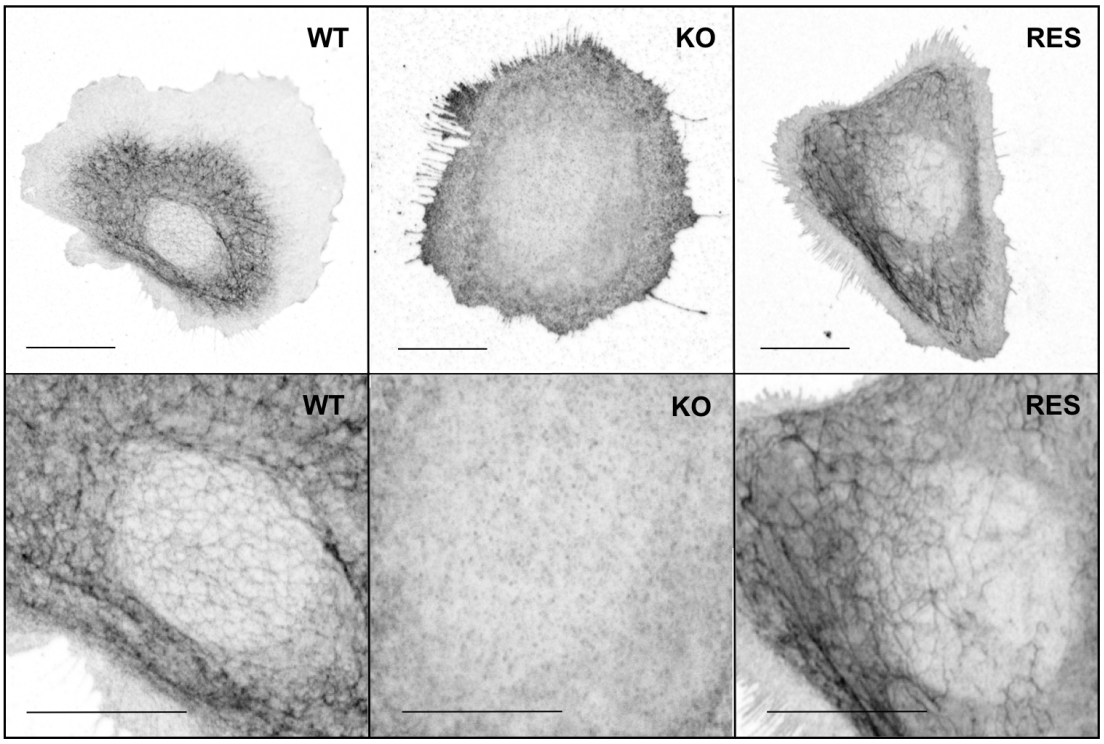

Figure 4.1.: Top row: immunostainings of the keratin network of a WT, a KO and a RES keratinocyte. Bottom row: zoom-in of the nuclear area. A higher laser intensity was used to image KO cells. Images are contrast inverted (scale bar: 20 µm). Adapted from [189].

4.2. Optimization of cellular elasticity measurements

The vast heterogeneity that characterizes any cellular population makes the quantitative study of properties such as single cell elasticity a challenging task. A comprehensive investigation of the different parameters affecting AFM experiments is therefore strictly necessary, in order to obtain reliable and reproducible results. In this section, the live cell indentation measurements are presented step-by-step along with the argumentations guiding the development of the experimental protocol used during our analysis.

4.2.1. Validation of elastic behavior upon indentation

A fundamental requirement for the analysis of indentation curves according to the Hertz model of course lies in their reproducibility. If, upon successive indentations, the force-indentation relations were to be very different from each other, we would find ourselves in the presence of viscous or plastic behaviors, which would prevent us from performing an elastic analysis. Therefore a control in this direction was strictly necessary.
For each measured cell, three successive curves were recorded immediately after each other, and were used for extraction of the Young's modulus E only if they showed good reproducibility. This was the case for the vast majority of data, which typically displayed an overlap whose representative example can be seen in Figure 4.2.

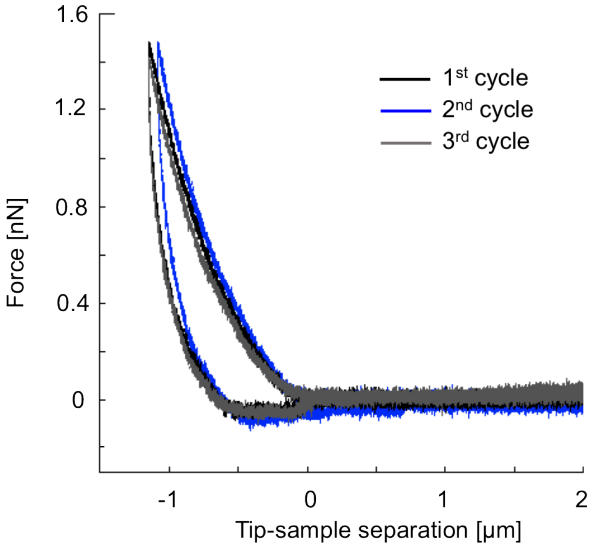

Figure 4.2: Plot showing the superposition of three AFM force-distance curves successively recorded on the same position above the nucleus of a WT keratinocyte. Adapted from [189].

4.2.2. Choice of indentation range

After having determined the contact point according to the algorithm described in Section 3.4.4, an important choice we needed to make was that of the indentation range to analyze. An approximate rule about the applicability of the Hertz model states that the analytical solution holds for indentations of up to 10% of the sample's thickness [173]. This restriction ensures that the analysis is performed at small indentations (hence in the linearly elastic domain) and that no influence from the hard substrate underlying the cell can affect the data. The typical thickness of WT and KO keratinocytes was therefore measured by means of live cell imaging. Above the nucleus, the measured cell

height was of 7.0 µm ± 1.4 µm for WT (N=6) and of 5.0 µm ± 0.8 µm for KO (N=4. Errors are s.d.). The cell body displayed a strongly variable thickness, but in proximity of the nucleus it was around 3-4 µm for all cells. A typical height profile is shown in Figure 4.3.

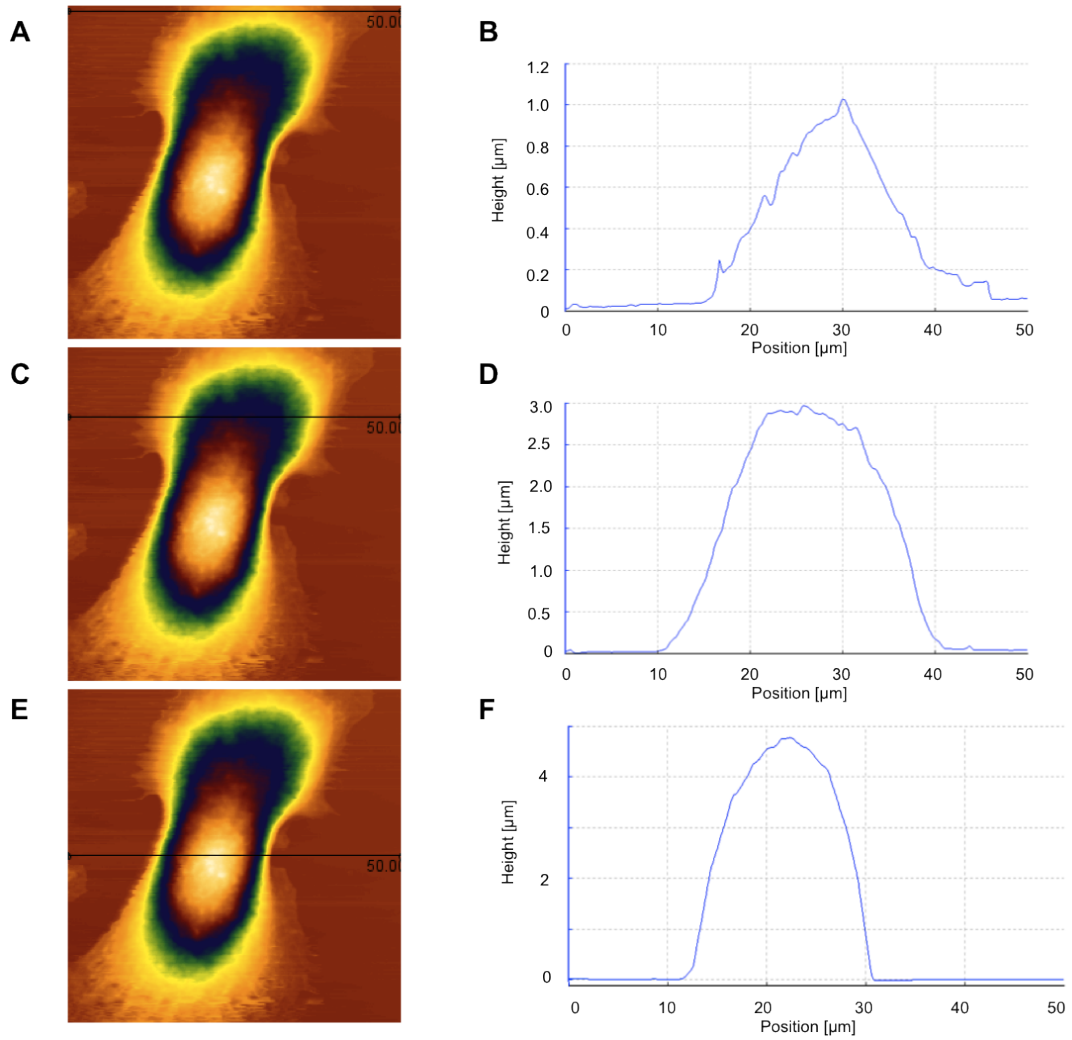

Figure 4.3.: A. C. E. AFM live contact imaging of a WT keratinocyte, and line profiles recorded above (**B**) the nucleus, (**D**) the cell body and (**F**) the lamellipodium. Tip velocity: 25 µm/s; force setpoint: 1 nN. Note the difference in height scale.

After obtaining such a first indication on the range of applicability of a Hertzian fit (which shall not exceed 500-700 nm from the contact point), we performed fits for increasing portions of the curve, using steps of 20 nm. It is well known that when observing

heterogeneous materials like single cells, the Young's modulus E will change as a function of indentation depth. By plotting such an "apparent modulus", we can observe this dependency and restrict our analysis to the range of indentation depths in which E remains roughly constant (see Fig. 4.4). Above the nucleus, a smooth plateau was present between 200-600 nm. Measurements performed above the cell body did not show the same level of homogeneity, perhaps due to the higher number of organelles, stress fibers or other subcellular structures that could be pressed upon while indenting. Despite the lack of precise indications coming from this control, the indentation depth used as a fit range for measurements performed on the cell body was fixed at 200 nm. For measurements performed above the nucleus, instead, the choice was of 500 nm.

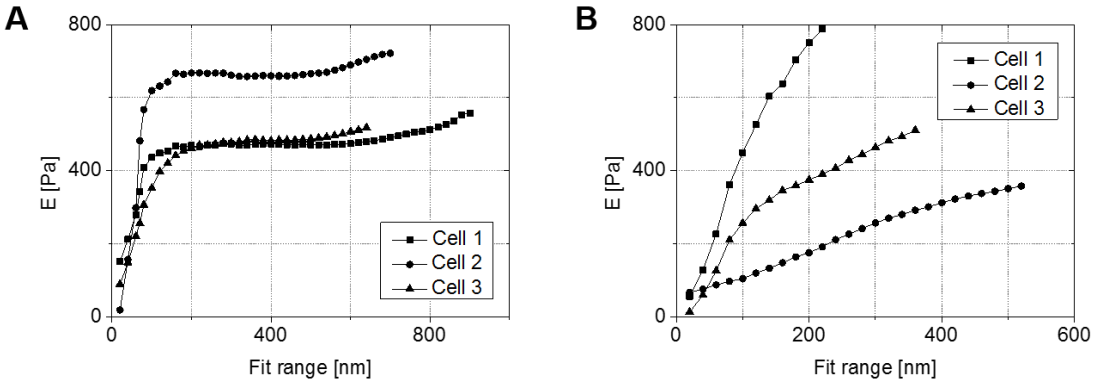

Figure 4.4.: Examples of the dependence of the Young's modulus E of three different cells on the choice of the fit range. For most measurements performed on the nucleus (**A**) a plateau is present in the interval 200-600 nm, whereas the same cannot be clearly identified over the cell body (**B**). Adapted from [189].

4.3. Determination of cellular elastic modulus via the Hertz model

4.3.1. JPK data processing software fit

Young's moduli E of WT and KO cells could at this point be determined: in a first step of analysis, the AFM manufacturer's data processing software (JPK-DP) was used to fit the Hertz model to the measured curves. To be noted that in this case Sneddon's formulation of the contact indentation problem was used as fitting function [181]:

$$F(a) = \frac{E}{1-\nu^2}\Big[\frac{a^2+R}{2}\ln\Big(\frac{R+a}{R-a}\Big) - aR\Big] \tag{4.1}$$

where

$$\delta = \frac{a}{2} \ln\left(\frac{R+a}{R-a}\right) \tag{4.2}$$

Here, δ is the indentation depth in terms of the instantaneous contact radius a and R is the indenter's radius. The Poisson's ratio ν was fixed to 0.5, assuming cells to be incompressible, and the Young's modulus E was the only fit free parameter.
As expected, the Young's modulus displayed an extremely large variance, with minimal and maximal values of 127 Pa and 3127 Pa for the WT and 100 Pa and 1509 Pa for the KO distribution, respectively. The number of analyzed cells was N_{WT}=105 and N_{KO}=110. Measurements above the cell body varied even more: WT cells had Young's moduli ranging between 24 Pa and 7104 Pa (N=110), and KO from 24 Pa to 5999 Pa (N=90). The resulting data sets appeared to be log-normally distributed, as is often the case for measurements performed on cells [92]. Histograms of E for WT and KO keratinocytes, along with the corresponding log-normal fits, are presented in Figure 4.5.

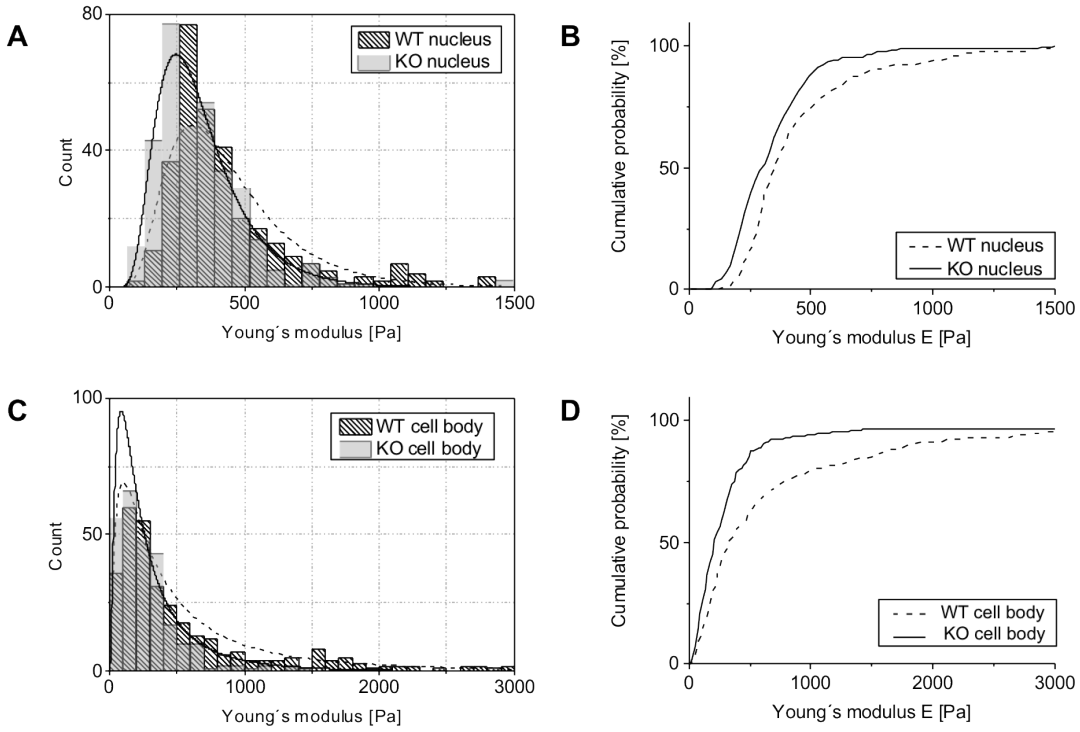

Figure 4.5.: Histograms of WT and KO keratinocytes Young's moduli E fitted via the JPK-DP software from curves recorded above the nucleus **(A)** and the cell body **(C)** with (lines) corresponding log-normal distributions. The shift becomes clear when representing the data as cumulative histograms (**B** and **D** respectively). In both cases, a statistically significant softening of the KO cells was observed (p = 0.003 and p = 0.0002 respectively). Adapted from [189].

When comparing the respective distributions, a statistically significant shift becomes apparent: a non-parametric Mann-Whitney-Wilcoxon test indicated p-values of 0.003 (nucleus) and 0.0002 (cell body), therefore hinting at the fact that keratin-free mutant cells are softer than their WT counterparts. To be noted that in the following we characterize all log-normal distributions in terms of their median values med(E) and multiplicative standard deviation σ^* as explained in Section 3.4.6. Such values are reported in Table 4.1.

Table 4.1.: Log-normal distributions of E moduli calculated according to the JPK-DP software ($E_{JPK\text{-}DP}$)

	med(E) [Pa]	σ^*
WT nucleus	395	1.64
KO nucleus	306	1.58
WT cell body	382	3.15
KO cell body	222	2.60

Force maps of whole WT and KO cells confirmed this softening (see Fig. 4.6).

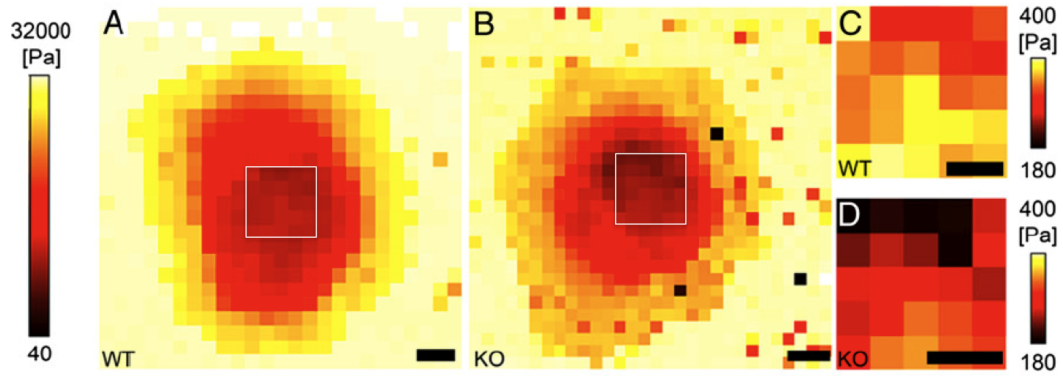

Figure 4.6.: Stiffness maps of a live **(A)** WT and **(B)** KO keratinocytes. Here, an indentation curve was performed on every grid position; the color coding displays the corresponding Young's moduli computed by means of the JPK-DP software. Scale bars: 10 µm. **(C)** and **(D)**: zoom-ins of the nuclear region of A. and B. respectively. Scale bars: 3 µm. Adapted from [189].

4.3.2. Hertz model with independent contact point determination

One problematic aspect in the automatized analysis performed via the JPK-DP software lies in the fact that during the fitting procedure the contact point is considered as a free fitting parameter, subject to optimization and change according to the fit range chosen. But an incorrect determination of the contact point can lead to very large errors in the calculation of the Young's modulus [186]. Given how sensible our results are to this parameter, we decided to develop a method for independently determining the contact point *prior* to any fitting procedure. The Matlab-implemented algorithm employed to this end is described in Section 3.4.4.
After identification of the contact points and fitting via the classical formulation of the Hertz equation:

$$F = \frac{4}{3}\frac{E}{(1-\nu^2)}\delta^{3/2}\sqrt{R} \tag{4.3}$$

it became apparent that, upon removal of this extra "artificial" degree of freedom, fit quality decreased significantly: the slight variations in the contact point allowed by the software were basically able to correct for the inaccuracy of the model at the cost of introducing a different error. A comparison of fits efficiency will be presented in Figure 4.10. This incapacity to accurately fit the AFM force curves is simply due to the assumptions underlying the Hertz model, that is inadequate to describe the complexity of biological systems. In spite of this, our previous results were confirmed: keratin-free keratinocytes are softer than the WT in correspondence of both the nucleus and the cell body (p=0.046 and p=0.032 respectively, see Fig. 4.7).

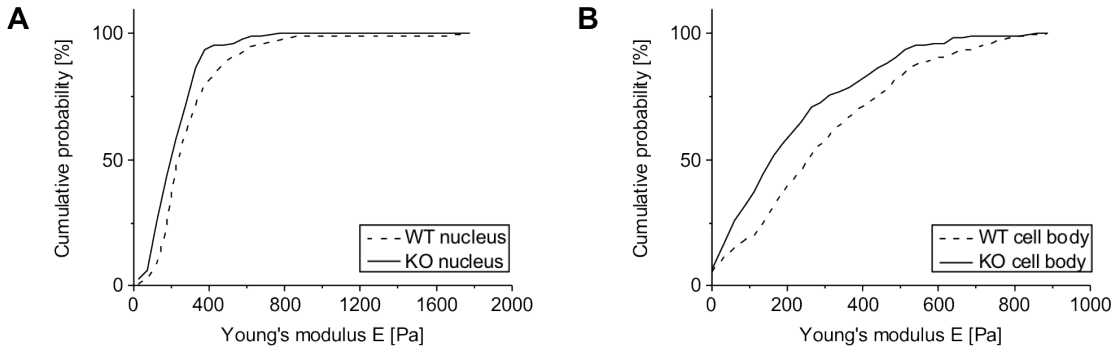

Figure 4.7.: Distribution of WT and KO keratinocytes E moduli fitted via the Hertz model after independent contact point identification. **A.** Nucleus **B.** Cell body.

In this case, the Young's moduli were lower than those obtained via the JPK-DP fitting

procedure (see Tab. 4.2), confirming the discrepancies in results that can derive from an inaccurate contact point determination.

Table 4.2.: Log-normal distributions of E moduli calculated according to the Hertz model (Eq. 2.5) after independent contact point determination

	med(E) [Pa]	σ^*
WT nucleus	272	1.69
KO nucleus	210	1.72
WT cell body	212	2.95
KO cell body	145	3.01

In any case, to improve the fitting quality, a further step of analysis consisted in an investigation of the optimal form of the force-indentation relationship.

4.3.3. Power law model with independent contact point determination

To this end, power law fits of the form

$$F = A\delta^b \tag{4.4}$$

(where A and b are free fit parameters) were performed in order to verify whether an exponent of 1.5 really is the best for fitting the data, as expected from Equation 4.3. The distribution of the resulting exponents b is plotted in Figure 4.8.
As it turns out, the exponents b were distributed normally and centered almost exactly around 2 (x_c=1.99, σ=0.26 for WT and x_c=1.98, σ=0.25 for KO, with N_{WT}=117 and N_{KO}=109). The distributions were practically undistinguishable between the two cell types, with a p-value>0.3. Therefore the exponent was fixed at a value of b=2 and, after independent contact point identification, fits were repeated on all measured curves in order to extract the prefactor A_2, now the parameter to be optimized during fitting:

$$F = A_2\delta^2 \tag{4.5}$$

Here, A_2 clearly does not exactly represent a Young's modulus, but by analogy with the classical form of the Hertz model we can assume that it must contain convolved information regarding both sample's stiffness and indenter's geometry. Although we do not know the explicit form of this dependency, we can nonetheless compare this "equivalent stiffness" parameter A_2 among the two cell populations.

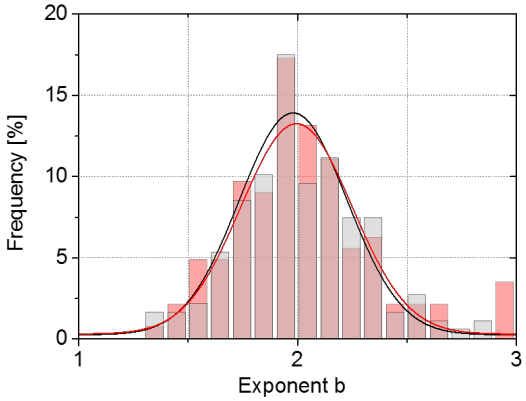

Figure 4.8.: Histogram of the exponents b obtained by fitting Eq. 4.4 to all measured indentation curves. The distributions could be fitted to a Gaussian distribution of the form $y=y_0 + \frac{A}{\sigma\sqrt{2\pi}} exp\left(-\frac{(x-x_c)^2}{2\sigma^2}\right)$ and show an almost perfect overlap (p-value>0.3). Adapted from [189].

To be noted that, for dimensionality reasons, A_2 also is expressed in units of Pa.
Also in this case data clearly pointed towards a softening of cells lacking a keratin network. Above the nucleus, WT values ranged from 270 Pa to 9173 Pa, while KO cells had values of A_2 between 116 Pa and 3624 Pa; again the distributions resulted log-normal, and statistically significantly different (p-value = 0.008). Mean distribution values resulted at least 25% lower for the mutant than for the wild type cell line (see Fig. 4.9). On the cell body the p-value was 0.003.

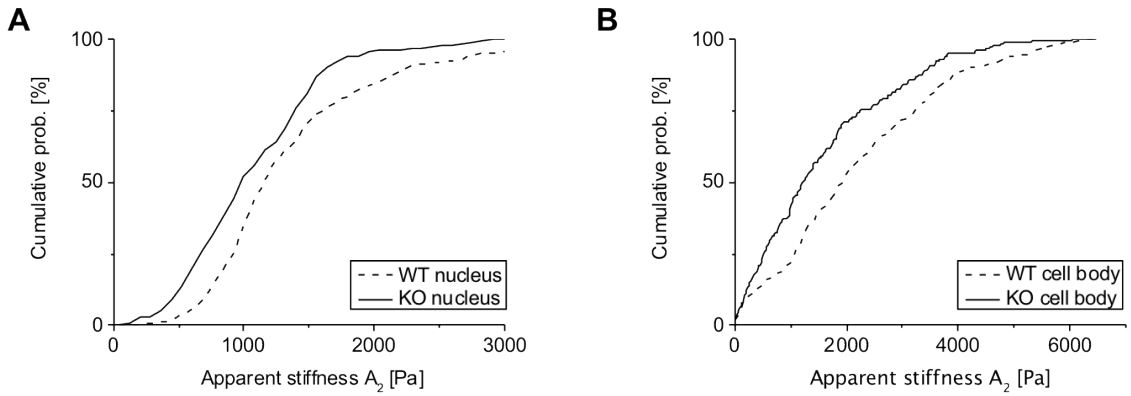

Figure 4.9.: Distributions of the prefactors A_2 obtained by fitting Eq. 4.5 to the indentation curves recorded on the nuclei **(A)** and cell body **(B)** of WT and KO cells.

Table 4.3.: Log-normal distributions of the prefactors A_2 calculated according to the power law model with fixed exponent b=2 (Eq. 4.5) after independent contact point determination

	med(A_2) [Pa]	σ^*
WT nucleus	1271	1.65
KO nucleus	969	1.72
WT cell body	1523	2.89
KO cell body	1022	3.16

4.3.4. Comparison of the different analysis methods for force curve fitting

While fitting experimental data to the different equations presented in the previous section, it became clear that the Hertz model is a rather approximate mathematical description for the measured data. The power law model with an exponent of b=2 resulted in the best fits of data, in contrast to what expected theoretically for the case of a spherical indenter. Independent determination of the contact point was crucial for identifying this discrepancy. As long as the contact point coordinate it is considered as a free fit parameter, in fact, the fit residuals can still be minimized just by moving it of the appropriate distance. Figure 4.10 shows representative fits of the three different models to the same data curve.

The RMS residuals were 13.8 pN for the JPK-DP fit (blue curve), 16.9 pN for the Hertz model with independently determined contact point (red curve), and of 12.6 pN for the power law with b=2 (green curve).

The reassuring aspect, though, is that the same fundamental conclusions regarding the elasticity of WT and KO cell populations could be reached via all three analysis methods.

As previously mentioned, possible sources of inaccuracy affecting data fitting lie not only in the heterogeneity of cells, but also in the imperfect geometry and surface roughness of both indenter and cellular surfaces. To try to assess the deviation of such parameters in our experimental system from the idealized description depicted by the Hertz model, we observed shape and roughness of the silica beads used as indenters via RICM (see Section 3.3.3): the images showed a rather inhomogeneous distribution of shapes and demonstrated how, very often, defects are present on the bead's surface (see Fig. 4.11 C).

Starting from topographical images of live cells, the surface RMS_{rough} of a cell's surface was calculated according to Eq. 2.3. An estimate of keratinocytes plasma membrane's

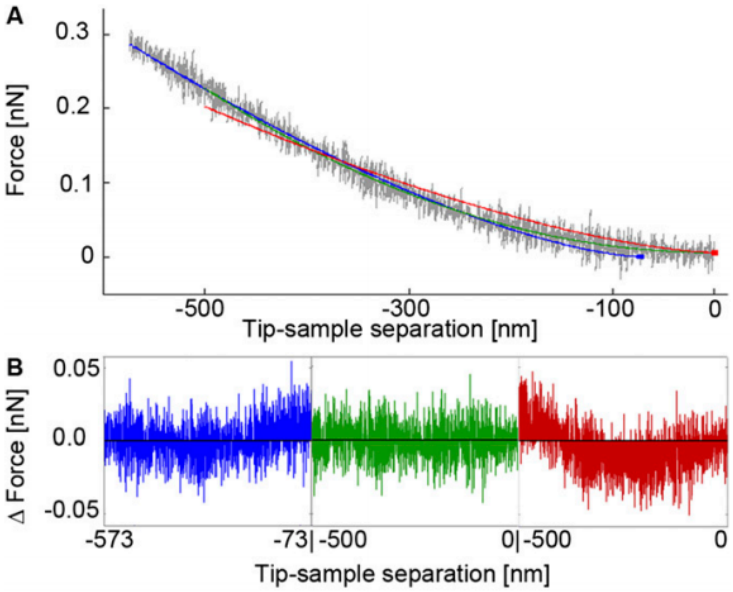

Figure 4.10: A. Fitted portion (500 nm) of a force-distance curve recorded on a nucleus. In gray: original data. In blue: JPK-DP software fit with contact point as free fit parameter (Eq. 4.1). Blue dot: fitted contact point. In green: fit of a power law (Eq. 4.5) with fixed exponent $b = 2$. In red: same fit with $b = 1.5$ (Hertz model, cfr. Eq. 2.5). Red dot: contact point determined directly from the third derivative method described in Section 3.4.4. **B.** Corresponding fit residuals. Adapted from [189].

roughness was performed by averaging values measured above the nucleus (41 ± 18 nm, with N=5) and the cell body (50 ± 23 nm, with N=7; errors are s.d.) for areas of 500 × 500 nm. A 3D reconstruction of a stripe of cellular plasma membrane is shown in Figure 4.11 B.

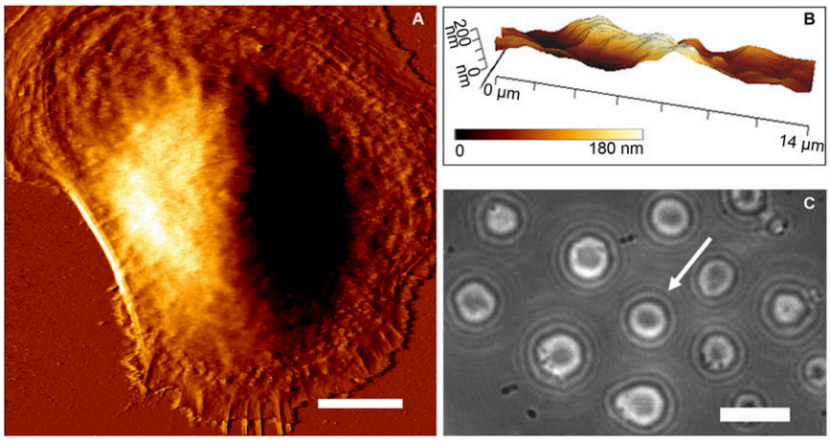

Figure 4.11.: A. Contact-mode AFM error signal image of a live WT keratinocyte. Tip velocity: 7.5 µm/s; force setpoint: 0.2 nN. Scale bar: 10 µm. **B.** 3D reconstruction of the surface topography of a 14×1.3 μm^2 portion of the plasma membrane used to estimate surface roughness. **C.** RICM micrograph showing shape and surface roughness of the silica beads attached to AFM tipless cantilevers and used as nanoindenters. The arrow indicates a representative bead selected for mounting. Scale bar: 10 µm. Adapted from [189].

4.4. Comparison of raw force-indentation data

Given all the above considerations regarding the difficulty of accurately applying the Hertz model to biological experimental data, we proceeded with a further step of analysis in which raw data directly read from indentation curves were compared. This allowed to obtain a model-independent comparison of the behavior of the two cell populations. When pressing upon two different objects up to the same indentation depth, it is only intuitive to expect that more force will be needed to indent the stiffer material than to indent the softer one. This was indeed the case; such a simple control, once again, confirmed the differences precedently observed between the elasticities of WT and KO cells. The force values needed to reach an indentation depth of 500 nm upon the nucleus were $304 \cdot 1.65$ pN for the WT and $239 \cdot 1.72$ pN for the KO (medians of the log-normal distributions. Errors are multiplicative s.d. σ^*). On the cell body, the median forces needed to indent 200 nm into the cell were $44 \cdot 3.52$ pN for the WT and $42 \cdot 2.95$ pN for the KO. For all indentation depths analyzed (and both for the nuclear and the lamellar measurements) statistically significant differences in the forces distributions were observed. The corresponding p-values are plotted in Figure 4.12. This final validation allowed us to conclusively proof that keratin-free keratinocytes are softer than their WT counterparts both in proximity of the nucleus and of the cell body.

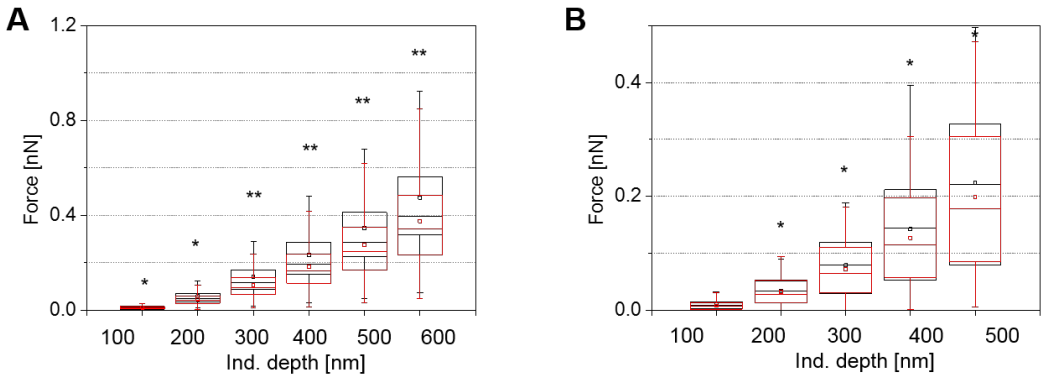

Figure 4.12.: Box plots showing the forces needed to reach a certain indentation depth **(A)** above the nucleus (N_{WT}=106, N_{KO}=110) and **(B)** above the cell body (N_{WT}=71, N_{KO}=59). In black: WT. In red: KO. Statistically significant differences are indicated as star symbols (p-value(*) < 0.05, p-value(**) < 0.01).

4.5. Control analyses

4.5.1. Indentation of type II KO keratinocytes

To rule out possible cell line specific artifacts and validate the generality of the obtained results, AFM measurements were repeated on WT and keratin type II KO cells. This time, a lower number of cells was analyzed (N_{WT}=11, N_{KO}=12), and measurements were only performed above the nucleus, given the higher homogeneity displayed on this position in previous measurements. Even such a small sample population showed statistically significant differences in cellular stiffness regardless of the fitting procedure used. Generally, type II KO keratinocytes displayed stiffness values (be it E moduli or A_2 prefactors) that were about 40% lower than the WT ones. Table 4.4 shows median values and corresponding multiplicative standard deviation σ^* of the measured log-normal distributions.

Table 4.4.: Log-normal distributions of E moduli calculated according to the JPK-DP software ($E_{JPK\text{-}DP}$) and the Hertz fit with independent contact point determination ($E_{A=1.5}$ and A_2) of WT (N=11) and type II KO keratinocytes (N=12)

	$Med(E_{JPK\text{-}DP})\cdot\sigma^*$ [Pa]	$Med(E_{A=1.5})\cdot\sigma^*$ [Pa]	$Med(A_2)\cdot\sigma^*$ [Pa]
WT	$205 \cdot 1.37$	$247 \cdot 1.32$	$653 \cdot 1.31$
KO	$116 \cdot 1.38$	$130 \cdot 1.40$	$346 \cdot 1.4$
p-value	< 0.001	< 0.001	< 0.001

4.5.2. Indentation of K14 rescue cells

To introduce a positive control and unmistakably attribute the reduced stiffness of KO cells to the absence of a keratin network, rescue (RES) keratinocytes re-expressing K14 were also analyzed.

The cell line was generated by the Translational Center for Regenerative Medicine (TRM) in Leipzig through insertion of YFP (yellow fluorescent protein)-marked human keratin 14 (K14) cDNA in the KO cells via lentiviral vectors [25]-[26]-[27]. Given that in type I KO the basic keratins were left unaffected, in fact, re-expression of the acidic K14 proteins was sufficient to restore the potential for heterodimerization with the basic binding partner K5. The YFP tag allowed to check the proper formation of a keratin network in each analyzed cell by means of a fluorescent microscope coupled to the AFM. Force distance curves were again analyzed by the standard power law function

with exponent b as a free parameter (Eq. 4.4). Because RES K14 cells were also characterized by a mean value of 2.01 ± 0.75 (normal distribution center and σ, respectively), the exponent was once more fixed at the value b=2 and the apparent stiffness A_2 was calculated as previously reported. To perform a reliable control experiment, WT and KO cells were measured again in parallel using the same cantilever.
When observing the cumulative histograms of E values and A_2 prefactors (Figure 4.13), it becomes clear that the stiffness moduli of rescue cells showed a biphasic distribution: about half of cells displayed reduced elasticity (comparable or even lower than the KO) while the other half presented WT-like values of stiffness. Because of this effect, when comparing median values of the distributions (reported in Table 4.5), the RES appears even softer than the KO.

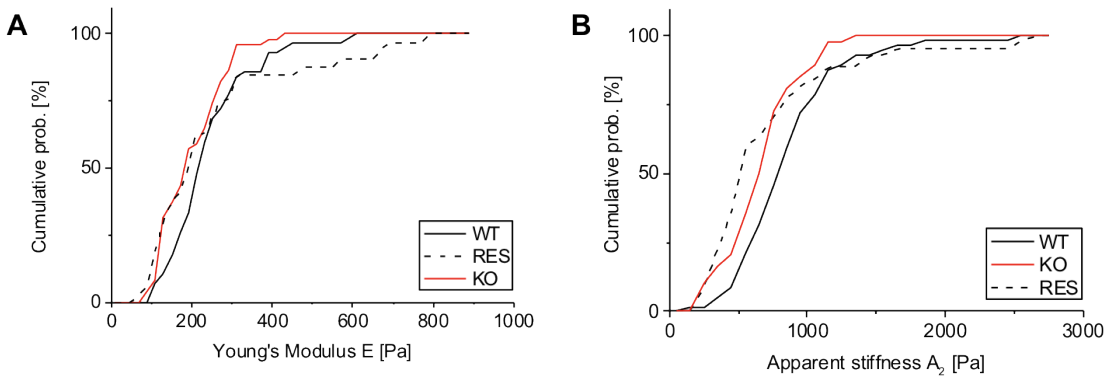

Figure 4.13.: Cumulative histograms representing the distributions of E moduli **(A)** and prefactors A_2 **(B)** of WT, KO und RES keratinocytes. Adapted from [189].

Table 4.5.: Log-normal distributions of E moduli calculated according to the JPK-DP software ($E_{JPK\text{-}DP}$) and the Hertz fit with independent contact point determination ($E_{A=1.5}$), as well as prefactor A_2 of WT (N=57), KO (N=51) and RES (N=46) cells

	Med($E_{JPK\text{-}DP}$) [Pa] · σ^*	Med($E_{A=1.5}$) [Pa] · σ^*	Med(A_2) [Pa] · σ^*
WT	229 · 1.48	315 · 1.64	840 · 1.63
KO	190 · 1.47	234 · 1.68	639 · 1.54
RES	196 · 1.75	230 · 1.74	614 · 1.79

On the other hand, when computing the mean values of the three groups the opposite effect is observed: the E modulus in that case corresponds to 304 ± 135 Pa for the WT, 212 ± 82 Pa for the KO and 254 ± 171 Pa for the RES (errors are s.d.). Analogously,

A_2 prefactor values average 960 ± 685 Pa for the WT, 700 ± 270 Pa for the KO and 740 ± 530 Pa for the RES. The heterogeneity of behaviors displayed by RES cells indicates how the restoring of cellular elasticity upon reintroduction of K14 is only partial.

4.5.3. Western blot and IF-stainings of actin and microtubule networks

In order to verify the independence of the biomechanical differences observed between WT and KO cells from cytoskeletal components other than keratin, the morphology and structure of actin filaments and microtubules was observed via immunofluorescence stainings in WT, KO and RES cells. No substantial differences could be observed, demonstrating that the overall actin and microtubule organization was unaffected by the absence of keratins (see Fig. 4.14).

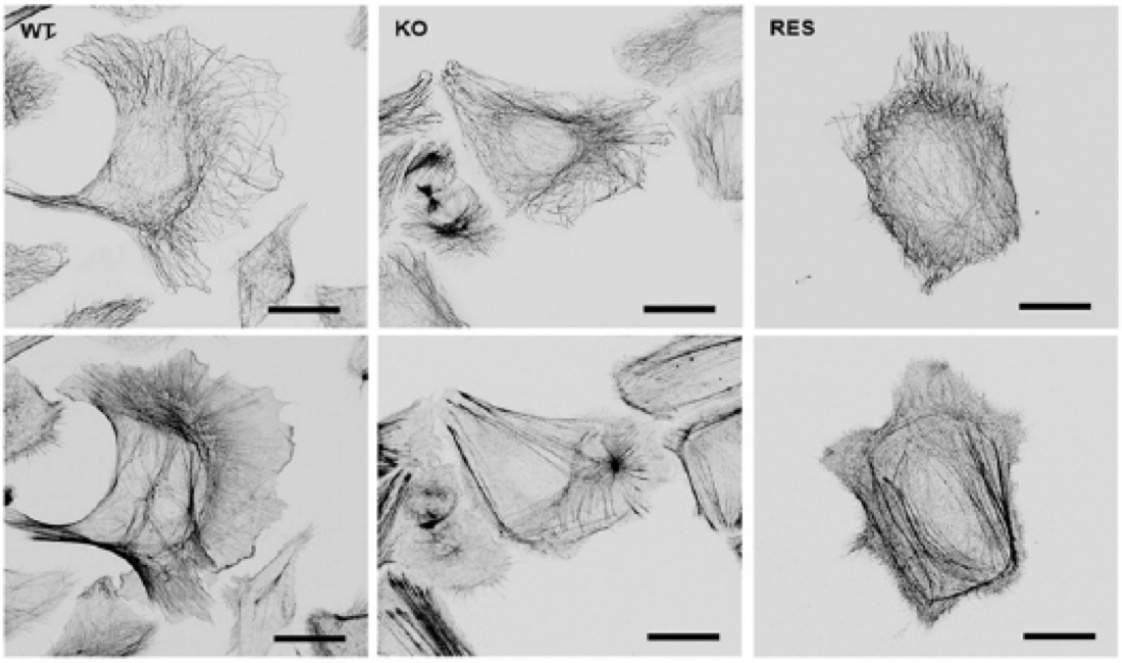

Figure 4.14.: A. Immunofluorescence staining of microtubules (upper row) and actin (lower row) in WT, KO and RES cells respectively. The images are contrast inverted. Scale bars: 20 µm. Source: [189].

To quantify the level of protein expression, Western blots were performed: in agreement with previous findings, no overexpression of actin or tubulin was revealed, meaning that the cells did not compensate for the absence of the IF network with an increased concentration of other cytoskeletal proteins (see Fig. 4.15).

Finally, to further rule out a possible influence of actin on the altered mechanical properties of KO cells, microfilaments were disassembled by latrunculin A (LatA) according to the protocol described in Section 3.4.3 in both WT and KO cells: an idea of the resulting damage in the actin network is given in Figure 4.16 B.
AFM measurements indicated again that WT cells are substantially stiffer than KO cells ($p<0.003$), strongly supporting the hypothesis that the keratin network is fundamental in determining cell stiffness (see Fig. 4.16).

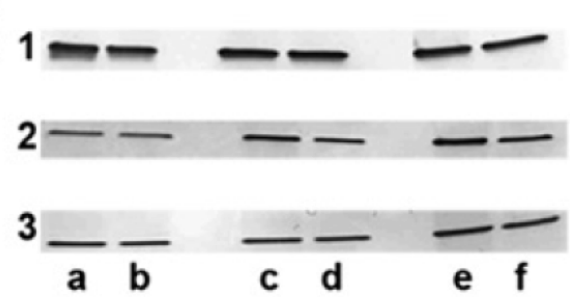

Figure 4.15: Crude protein extract analysis by Western blotting. GAPDH, a constitutively expressed marker, was used to equalize protein concentrations (1); subsequently tubulin (2) and actin (3) expression levels were analyzed. (a) and (b) indicate the WT corresponding to (c) KO type I and (d) KO type II. (e) and (f) show the K14 and K5 rescue, respectively. Source: [189].

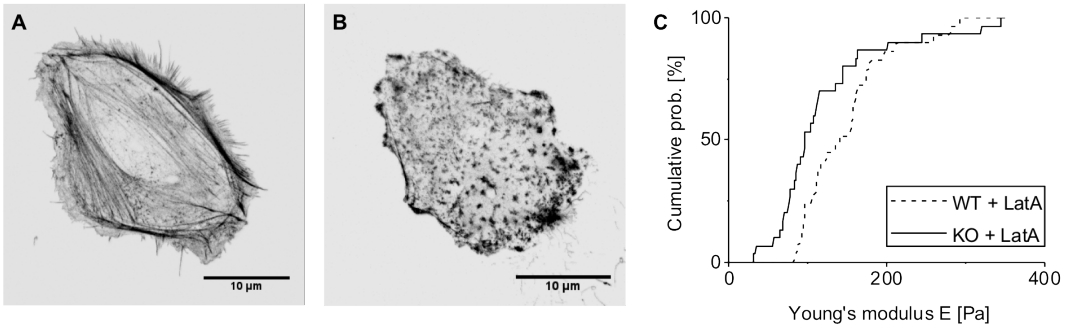

Figure 4.16.: A. Actin staining of a KO keratinocyte and (**B**) actin staining of a KO keratinocytes incubated with a 0.5 µM solution of latA in medium. The images are contrast inverted. **C.** Cumulative histograms representing the distributions of Young's moduli obtained via AFM elasticity measurements performed above the nucleus of WT and KO type I cells after depolymerization of actin filaments by LatA ($N_{WT} = 30$, $N_{KO} = 30$).

4.6. Keratinocyte monolayers

To assess the relevance of these findings also in a more physiological context, monolayers of keratinocytes were also analyzed via AFM indentations, this time only in correspondence of the nuclei positions. In these experiments (performed by T. Marković as part of an IHRS BioSoft summer school supervised at the ICS-7) a lower number of cells was analyzed (N_{WT} = 68, N_{KO} = 66 and N_{RES} = 72) but the resulting elasticity moduli confirmed our previous findings.
Notably, again significantly less force was required to indent KO cells than WT cells: a plot of raw force-indentation data is presented in Figure 4.17. In this case, despite re-expression of keratin K14, cell monolayers appeared more similar to KO cells than to the WT. This fact, together with the observations reported for the single cell case, suggests that K14 would not be sufficient to completely restore the biomechanical properties of keratin networks.

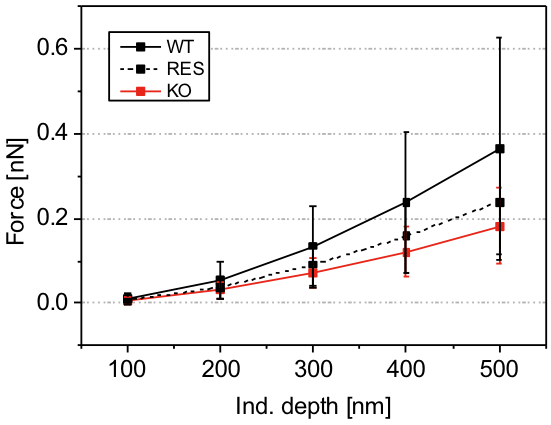

Figure 4.17: Plot showing the average forces needed to reach a certain indentation depth on WT, KO and RES keratinocytes monolayers. Error bars are s.d.

Upon fitting with the Hertz model, a statistically significant difference between the WT and KO distributions was observed (p-value<0.05), with mean values of E_{KO} about 47% lower than E_{WT}. Fitting a power law with free exponent b to the measured force curves again gave a Gaussian distribution almost centered around 2 (1.86 ± 0.33).
Therefore, fits of Equation 4.5 were repeated in order to obtain the apparent stiffness modulus A_2 of cells interconnected in monolayers; again, the fit range was held to 500 nm. Interestingly, the absolute values of both Young's moduli and A_2 prefactors were systematically higher than in the single cell case (see Table 4.6). This effect, minimal for KO cells, was especially pronounced for WT and RES keratinocytes, indicating the importance of desmosomal connections in binding IF together and thereby creating a

coupling effect able to strengthen the whole cell cluster. The corresponding distributions are plotted in Figure 4.18.

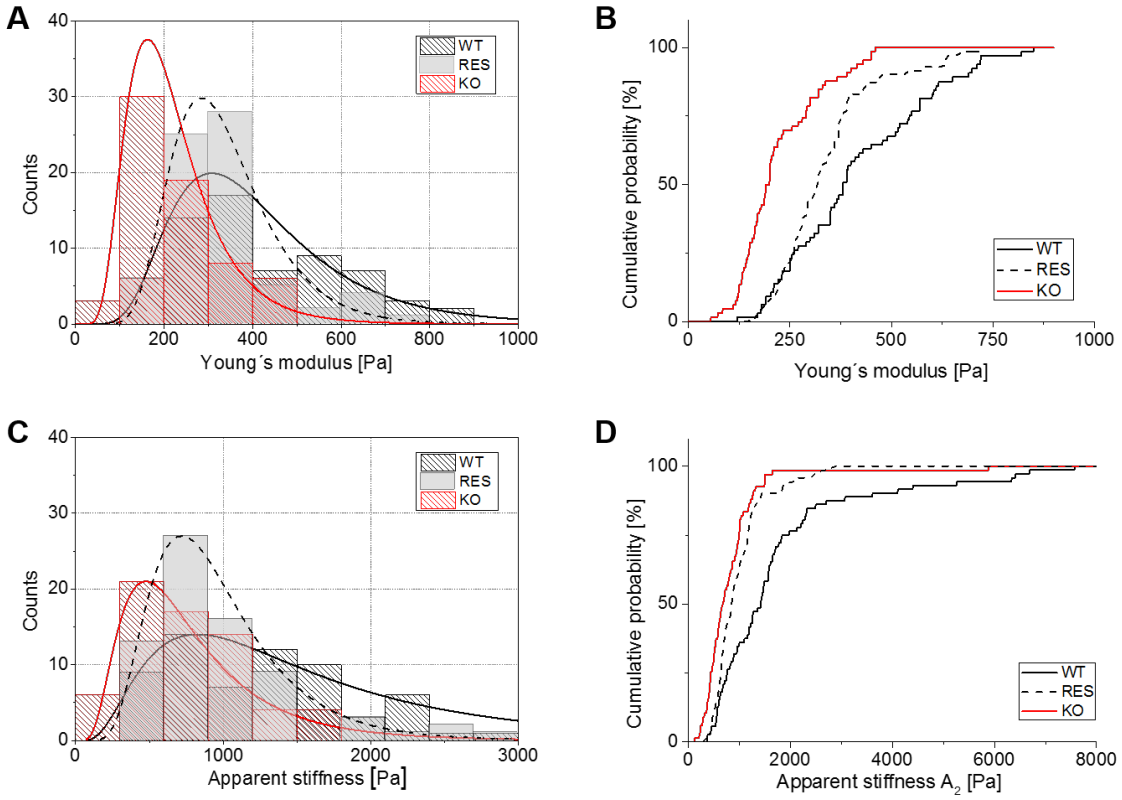

Figure 4.18.: A. Distributions of WT, RES and KO cell clusters Young's moduli as calculated with the Hertz model and (**B**) corresponding cumulative histograms **C.** Distributions of WT, RES and KO cell clusters prefactors A_2 and (**D**) corresponding cumulative histograms.

Table 4.6.: Log-normal distributions of Young's moduli E and apparent stiffness A_2 for WT, KO and RES cell monolayers and comparison to the single cell case

	Med(E) $\cdot$ σ^* [Pa]		Med(A_2) [Pa] $\cdot$ σ^*	
	Single cells	Monolayer	Single cells	Monolayer
WT	229 $\cdot$ 1.48	376 $\cdot$ 1.56	840 $\cdot$ 1.63	1355 $\cdot$ 2.02
KO	190 $\cdot$ 1.47	198 $\cdot$ 1.57	639 $\cdot$ 1.54	675 $\cdot$ 1.80
RES	196 $\cdot$ 1.75	318 $\cdot$ 1.40	614 $\cdot$1.79	879 $\cdot$ 1.57

Unlike the single cell case, rescue cell monolayers showed a larger sensitivity upon fitting method: when analyzed with the Hertz model, in fact, the distribution was much closer to the WT one than when analyzed with the power law. Given that fit quality, in the latter case, is much higher, and considering the raw data plots, we can conclude that in the case of cellular clusters, re-expression of a single keratin protein is not enough to restore the network's elasticity.
A confirmation of this fact lies in the structure of the keratin networks that can be observed via immunostainings (see Figure 4.19). The KO obviously still lacks any filament structure, but the differences in the morphology of WT and RES cells are in this case amplified. Wild type monolayers show a fine structure spanning the whole cellular surface, and the desmosomal connections between filament bundles of neighboring cells can be clearly seen (an example is shown in Figure 4.19 A). On the other hand, rescue cells display a larger mesh size and single, broader, better defined filament bundles, probably responsible for the biphasic distribution in elasticities measured above the nuclei. In this case, desmosomes are especially well-defined, as revealed by the desmoplakin immunostainings (see Fig. 4.19 F).

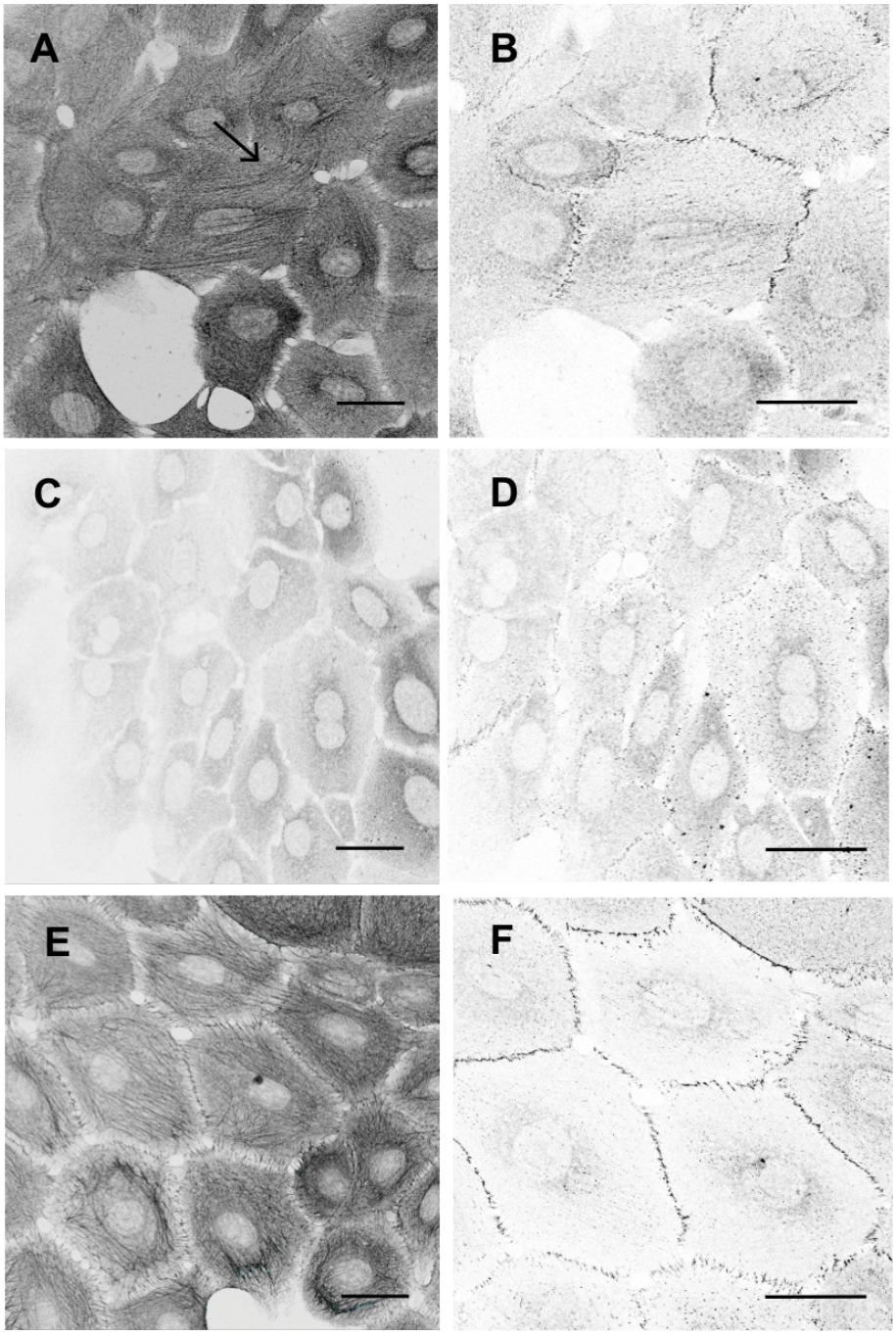

Figure 4.19.: Immunofluorescence stainings of keratin (left) and desmoplakin (right) in WT (**A-B**), KO (**C-D**) and RES (**E-F**) keratinocytes monolayers. The arrow indicates bundles of filaments of neighboring cells connected by desmosomes. Images are contrast inverted. Scale bars: 10 µm.

4.7. Discussion of the results on keratinocytes

In this part of the work, the elasticity of wild-type and keratin-free epidermal keratinocytes has been analyzed. The resistance of such cells to external mechanical stress has been of interest for decades because of its crucial implications in many cellular functions, such as differentiation [51], cancer progression [152], migration and wound healing [145]. In tissue, epidermal keratinocytes are subject to stress in all directions, and are highly resilient and extensible: single filaments in vitro can be stretched more than 2.5-fold [21], and elongations of more than 130% without filament rupture have been reported in cultured keratinocytes [22]. A growing interest for the mechanical properties of individual IFs has led to studies reporting, for example, that single keratin filaments adsorbed on surfaces have a persistence length of about 0.30 to 0.48 µm (in the absence or presence of magnesium ions, respectively [137]), or that keratin gels, like other biopolymer networks, show strain stiffening. Suspensions of keratin IFs behave like viscoelastic solids, recover very rapidly after cessation of deformation and have an elastic modulus that strongly depends on shear parameters and history [60].

But probing the role of IF filaments in living cells is more challenging, due to the large number of interactions present in such a complex and dynamic environment.
Seminal publications have proposed that, in vivo, IFs might serve as a major mechanical buffer system protecting cells from environmental stress [151]. In literature, this hypothesis has been investigated either by studying biomimetic model systems of artificial IF networks [146], or by analyzing whole cells or mouse models [148]-[147]: such papers reported a very low bending stiffness for keratin filaments and recorded only a minor effect of keratin on cell elasticity. So far, though, elasticity measurements had mainly focused on investigating the role of the actin network to the mechanical properties of keratinocytes [136], given that IFs cannot simply be depolymerized by drug treatment as is instead possible for microtubules (using, for example, nocodazole or colchicine) or actin filaments (via cytochalasins or latrunculin [57]).
The challenge of understanding the mechanical role played by keratin filaments for the structural stability of whole cells, though, can only be overcome upon direct observation of completely functional and yet keratin-free cells: therefore it becomes necessary to block the expression of keratin proteins by deleting the whole gene cluster expressing them. Thanks to the work of Prof. T. M. Magin and coworkers [25], two different mutant cell lines were established: these are type I and type II keratinocyte KO cells, lacking all acidic and basic keratins respectively. Given that keratin IFs need the coupling of

an acidic and a basic dimerization partner as fundamental building blocks, such mutant cells are completely devoid of an intermediate filament cytoskeleton although they still retain normal microfilaments and microtubules.

Here, as a first experiment we characterized the keratin network of WT, KO and RES keratinocyte cell lines by means of light microscopy. Fluorescent imaging showed that KO cells display a diffuse, finely distributed keratin signal that only becomes visible upon higher laser power and longer illumination times than those necessary to identify the network in wild-type cells. It is possible that, in absence of a dimerization partner, the translated keratin proteins are immediately degraded and therefore not visible. To introduce a control system, matched rescue cell lines re-expressing the basal cell-specific keratin pair K5/14 were also analyzed. Expression of the individual binding partners was completely sufficient to restore the formation of a keratin network in RES cells, although this appeared less homogeneous and finely distributed than the wild-type one (see Section 4.1). This lets us speculate the need of putative interactions of the K5/K14 heterodimers with other keratins in order to form a completely functional IF network, which might help explain the high redundancy of keratin proteins expression in epithelia. The compensatory effect of keratins is well known: in vivo, for example, upon deletion of K14, K15 is overexpressed in order to allow for the creation of K5/K15 pairs substituting for the missing K5/K14 ones [143]. But yet the over 10 acidic keratin proteins encoded in epithelia must have a more stringent function than just acting as "reserves" in case of a genetic defect [144].
To assess the role played by keratin in determining cellular stiffness, such RES cells were compared to WT and KO epithelial keratinocytes by means of AFM indentation experiments. Typically, analysis of the indentation curves is performed applying the Hertz solution of the contact problem of a rigid sphere indenting a linearly elastic half-space to the AFM data [182]. This approach, though, is not without its problems.

4.7.1. Limitations of the Hertz model

Application of the Hertz model to the analysis of cellular indentation measurements only has a limited theoretical legitimation. The situation it depicts, in fact (namely, a perfectly spherical, hard indenter pressing upon a homogeneous, isotropic, linearly elastic, infinite half space) is certainly not a faithful description of an AFM tip indenting a cell. Such an approach can nonetheless represent a precious tool for analyzing cellular elasticity, provided that some attention is exerted upon its application.

The first possible source of error lies in the assumptions about the geometry of both indenter and analyzed surface, which are described as smooth and frictionless. Here, AFM imaging allowed to estimate the surface roughness of keratinocytes plasma membranes (which lies in the range of 20-70 nm for areas of 500×500 nm^2) and RICM imaging displayed the many surface imperfections of the silica beads used as indenters, which are neither perfectly smooth nor exactly spherical.
The finite thickness of cells is another violation of the model assumptions: to minimize the introduction of error from this source, the height of living, single keratinocytes was determined by means of AFM imaging and indentations were kept at values lower than 10% of the total thickness [173], both in correspondence of the nucleus and the cell body. Despite our efforts to reduce experimental error (for instance, all indentations on single cells were performed using the same cantilever in order to minimize calibration differences between different measurements), these of course can never be ruled out.
But, most importantly, we should account for the fact that cells actually are viscoelastic objects, as well demonstrated by the hysteresis cycles ubiquitously present in indentation curves and by the fact that AFM data report higher stiffness values when cells are indented at higher speeds [135]. The contribution of this viscous component increases at larger deformations, so that experiments in which a force-clamp phase is added during the tip-sample contact allow the extraction of quantitative viscoelastic sample properties [90]. When performing comparative measurements between different cell populations, though, these factors can be neglected as they do not impair the fundamental outcomes of experiments.

An especially delicate issue in AFM force spectroscopy experiments lies in the determination of the contact point. The extreme sensitivity of fit results on this parameter, in fact, is well known and has been the object of numerous studies reporting estimates of the error introduced upon its inaccurate determination [174] as well as automated methods for its identification [175]. Misidentifying the contact point of as little as 100 nm, for example, has been shown to already completely prevent correct estimation of the material's properties [186].
On hard substrates, the contact point can be identified with a precision in the order of the nanometer. On soft substrates, though, because of the indentation of the tip into the sample, the cantilever deflection is not instantaneous but rather gradual; this fact is reflected by the shape of indentation curves, which are not straight lines but bend as shown in Figure 2.3. It would therefore be unthinkable to rely on manual contact point identification procedures: here, because of its conceptual simplicity and good accuracy,

we used an algorithm searching for local maxima of the curve's third derivative (Section 3.4.4). The importance of following such an approach has been shown while comparing different data analysis methods (Section 4.3.4). The AFM manufacturer's software for data analysis (JPK-DP), for instance, leaves the contact point as a free fit parameter able to vary until the overall residuals are minimized: in Section 4.3.2 we showed that, if one keeps using the traditional Hertz formula while, instead, independently determining the contact point prior to any fitting procedure, the fit quality significantly worsens.
We therefore decided to verify whether the exponent expected by the Hertz law for the force-indentation relationship of a spherical indenter (i.e. 1.5) actually is the best one for describing data recorded on live cells. Fits of a simple power law equation ($F=A\delta^b$) showed a distribution of the exponents b almost exactly centered around 2 for all analyzed cell types (Section 4.3.3); curiously, this is the value one would theoretically expect for conical indenters [174].

This discrepancy just confirms the limitations of the Hertz model to describe the present scenario. Besides all the aforementioned approximations, another notable one lies in the hypothesis of material incompressibility, which leads the universally accepted postulate that the Poisson's ratio of single cells would be ν=0.5. Despite the difficulty of actually experimentally determining such a parameter for live cells, there have been sporadic studies in this direction; an example is a work reporting values of ν=0.38 for single chondrocytes as assessed by micropipette aspiration experiments [96]. Assigning a probably erroneous value of ν=0.5 to keratinocytes might not alter the value of our comparative analysis (in that it would introduce a systematic error for all analyzed cells), but surely makes it less precise.
The underlying assumption that the analyzed materials are homogeneous and linearly elastic, though, is probably the main approximation introduced by a Hertzian approach: in the following chapters we will see how more elaborated models, describing biological samples as hyperelastic materials, can go one step further in offering a realistic description of objects as complex as cells and tissues.

4.7.2. Keratin loss causes significant cell softening on the single as well as on the multicellular level

Regardless of the issues concerning data analysis, both by fitting AFM curves to various models and by directly comparing raw indentation data we could clearly observe an overall cellular softening upon deletion of the keratin networks. This was the case both

in correspondence of the nucleus and of the cell body, with median values for the elastic modulus of KO cells about 25% to 35% lower than their WT counterparts, respectively. This result reveals the crucial importance of a functional keratin network for determining cellular stiffness and therefore in enhancing the capacity of keratinocytes to withstand external stress.
The extremely broad distributions of the measured force-indentation curves (and of the different elasticity moduli calculated from them) should not come as a surprise: cells are highly heterogeneous systems whose cytoskeleton rearranges dynamically and never has the same configuration twice. In a first phase of measurement, only single, adherent and rounded cells were analyzed in order to try and minimize the differences in the actin architecture within the sample population. Given the rather small radius of the indenter used to probe the cells, though, it is very probable that part of the scatter of the data was simply caused by accidental indentations in correspondence of very stiff stress fibers or other cytoplasmic components. This also explains why the data recorded on the cell body show a larger variance than those recorded above the nucleus, where the keratin network is thicker and the cytoplasm mostly free of organelles. For this reason, measurements on cell monolayers were exclusively performed in correspondence of the nuclei.
Quite similar biomechanical deficiencies were reported for both type I and type II knockout cells (Section 4.5.1): the reductions in Young's moduli were in this case even higher (about 45%), but on the other hand the sample population analyzed was smaller. Given that the two mutant cell lines showed very similar morphologies and IF immunostainings, taken together we could exclude cell-line specific artifacts.

Additional microrheological magnetic tweezers analyses were performed by the group of Prof. R. Leube (MOCA center, RWTH Aachen) in collaboration with our institute and specifically in the context of this thesis, but they are not reported here (for details, see [189]). In such experiments, a microbead of few micrometer diameter was injected into the cytoplasm and cyclically pulled by means of a magnetic field to test the resistance it experiences in the viscous cytoplasmic medium. Given that the viscoelastic response of cells to small deformations is characterized by a weak power law in time [142], the so-recorded creep response curves could be used to extract elastic and viscous parameters characteristic of WT, KO and RES cells.
The results in this case pointed towards even more drastic differences between the phenotypes than the ones recorded via the AFM indentation experiments: only in KO cells, in fact, but not in WT and RES, did the application of successive magnetic tweezers

pulses cause plastic deformations. Such observations further confirmed the effectiveness of keratin networks as mechanical buffer system, the absence of which resulted in a lower effective spring constant and a reduced cytoplasm viscosity of KO cells.
Previous reports on other IF systems are in line with these results: flow cytometry studies for example showed how the rigidity of T-lymphocytes primarily depends on intact vimentin filaments [141] and extracellular magnetic twisting cytometry experiments demonstrated that vimentin-deficient fibroblasts offer a reduced resistance to mechanical stress [139].

AFM measurements repeated on cell monolayers not only confirmed this trend, but actually showed even more dramatic differences between wild-type and mutant keratinocytes than in the single cell case. A shift of almost 50% was in fact recorded between the median values of the elasticity modulus distributions of WT and KO monolayers (Section 4.6). This amplification in cellular stiffness (absolute values of the Young's modulus were systematically higher, within the same cell population, for multicellular clusters) is due to the presence of desmosomes. A study analyzing the effect of an Arg125Pro point mutation of K14 leading to downregulation of desmosomal proteins in keratinocytes reported how impaired desmosomes led to a significantly lower integrity and overall weakening of epithelial sheets upon shear stress [89]. Along the same lines, AFM analysis of keratinocytes stiffness after desmosomal disruption by means of anti-desmoglein 3 antibodies have showed how the absence of desmosomes leads to a change in the prestress which defines cellular stiffness [88]; desmosomes therefore not only anchor intermediate filaments at the plasma membrane, but effectively form a 3D supracellular scaffolding that acts as a collection of tethers providing mechanical strength to the tissue.

4.7.3. Keratin loss does not affect actin and microtubule networks

To ensure that the biomechanical differences observed between WT and KO cells exclusively depended on keratin IFs, a number of control experiments was performed (Section 4.5). Western blotting showed that neither actin nor tubulin expression levels were altered in the mutant cells, and immunofluorescence stainings confirmed no substantial change in the architecture and organization of the corresponding cytoskeletal structures. These results are well in line with previous observations on protein levels in type II KO cells [25]-[26]. Furthermore, pharmacological actin network disruption by means of latrunculin treatment had the effect of reducing the overall cellular stiffness (as it would be expected upon removal of cortical actin) but did not influence the clear biomechanical

differences observed between WT and type I KO cells (Section 4.5.3).
Such data therefore clearly indicated the keratin network as responsible for the differences in elasticity observed between WT and KO cells: despite the relatively low indentation depths analyzed (500 nm above the nucleus, where the network is denser and the cell thicker, and 200 nm on the cell body), AFM indentations were sufficiently deep to deform not only the cortical actin but also the keratin network underneath. Picturing the morphological complexity of a cell, whose cytoplasm is obviously not only composed of cytoskeletal filaments but also by a vast and heterogeneous collection of organelles, and considering that the bending stiffness of IFs has been estimated to be as low as 4-12 $\cdot$ 10^{-27} Nm^2 [146], it is striking to manage to measure such small differences in elasticity in a live cell. These results just offer one more demonstration of the incredible sensitivity of AFM measurements, and of how successfully such an instrument can be applied to the investigation of biological systems.

4.7.4. Re-expression of keratin 14 partially rescues the keratin network and cellular elasticity

Finally, analysis of type I RES cells (which express a single acidic protein, K14) showed that the pair K5/K14 is sufficient to build a keratin network rather similar to the WT one, despite the morphological differences already described. In the case of single cells, AFM indentation experiments indicated a partial recovery of cellular elasticity, with a mean value of the Young's moduli distribution reaching about 80% of the wild-type ones (Section 4.6). Median values, on the other hand, were not substantially different between the RES and KO groups. This was due to the distribution shape, which appeared biphasic; about 50% of the cells presented a reduced elasticity and the other 50% showed values of stiffness even higher than the WT ones. At least two cellular populations were therefore present in this case. This effect disappeared in the case of cellular monolayers, which showed median values for the RES distribution spanning 65% to 85% of the WT level, according to the fitting method used.
Such differences are most likely caused by the slight alterations observed in the structure and morphology of the RES keratin networks: the absence of acidic dimerization partners other than K14 in fact makes the networks of such cells strongly dependent on the expression level of this particular protein, which significantly varies within the population. Although during measurements only those cells displaying a fully formed IF network were analyzed, in fact, many others did not express a keratin network at all. It is possible that the increased networks mesh size, on the one side, and the local

bundling of filaments on the other side were the cause for such differences. Magnetic tweezer analysis, anyhow, recorded a full recovery of the network viscoelastic properties upon reintroduction of K14 [189].

Taken together, these results answer the pivotal question regarding the function of keratin IF in protecting epithelial cells against mechanical stress: lack of keratin filaments significantly softens cells and reduces cell viscosity, an effect that can only partially be reversed by re-expression of single keratin genes. The data presented therefore make a very strong case for the crucial contribution of keratins to cell mechanics, with far-reaching implications for epithelial pathophysiology [189].

5. Results: biomechanical analysis of MCF10A spheroids

In this chapter, we shift the focus from the analysis of 2D to that of 3D cell culture systems and report the biomechanical characterization of MCF10A acini as popular in vitro model for breast gland terminal ductules.
In a preliminary step, the morphology of the different age groups of MCF10A acini was characterized via fluorescence microscopy. Next, we performed a permeability study of the basement membrane surrounding the acini: to this end, the fluorescence profiles of dextran tracers added in solution were followed over time as they penetrated through the BM and into the intracellular space. From the different penetration speeds of differently sized dextran molecules, semi-quantitative information regarding the membrane permeability could be obtained.
Successively, comparative AFM indentation experiments on native and decellularized MCF10A acini revealed the fundamentally elastic nature of basement membranes and their crucial importance in conferring mechanical stability to MCF10A spheroids. BMs were then isolated and characterized by means of AFM, SEM and fluorescent imaging; this allowed to obtain information regarding their thickness, surface roughness and network structure.
In a final step, AFM indentation experiments were performed on MCF10A acini of different maturation grades as well as on the corresponding malignant multicellular agglomerates (MDA-MB-231 3D structures). A comparison between the two cell lines is reported along with an analysis of the indentation curves assuming a hyperelastic material behavior. The application of such a material model to 3D cell clusters is finally validated via FEM simulations.

5.1. Morphology of MCF10A acini

As already reported in literature [52]-[54], 3D MCF10A acini grown in EHS matrix gels display a morphology that changes according to the maturation grade: at first, spherical

structures showing apico-basal polarization are formed; successively, these start secreting a basement membrane layer to surround them and progressively build a luminar space by extruding the apoptotic cells from the sphere interior. Immunocytochemical stainings of MCF10A cultures are presented in Figure 5.1: the image gives an idea of the large differences which can arise in acinar size.
This refined tissue architecture is completely lost when breast cancer cell lines are cultivated in analogous conditions (for details on the culture protocols, see Section 3.2): here we used MDA-MB-231, a highly invasive cell line used as a model for the study of metastases. MDA-MB-231 3D agglomerates show less uniform morphologies, going from the roundish to the stellate structure, and do not secrete a basement membrane, in line with previous reports [55]. The difference between the two can be appreciated in Figure 5.2.

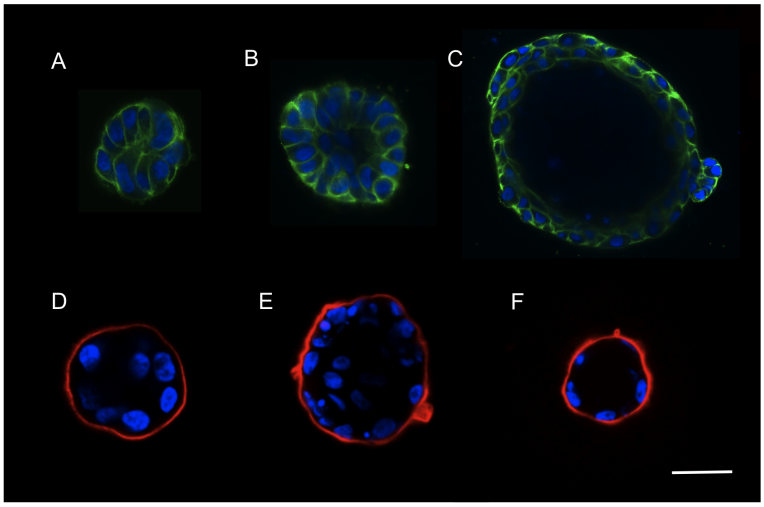

Figure 5.1: Immunofluorescence stainings of fixed MCF10A acini in EHS matrix at different maturation grades. In green: actin phalloidin cytoskeletal stain; in blue: draq 5 nuclear stain and in red: collagen type IV basement membrane stain. (**A**) and (**D**): low-matured group; (**B**) and (**E**): semi-matured group and (**C**) and (**F**): highly-matured group. Note the heterogeneity of sizes. Scale bar: 20 µm. Adapted from [54].

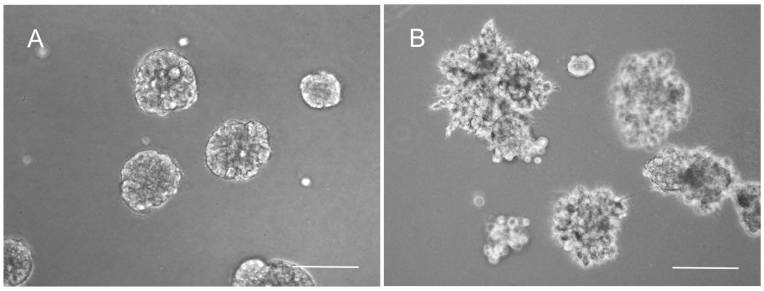

Figure 5.2: Phase contrast images of (**A**) MCF10A spheroids and (**B**) MDA-MB-231 3D agglomerates. Note the loss of epithelial organization typical of invasive cells. Scale bar: 100 µm.

5.2. Dextrane permeability analyses

To assess the permeation properties of the basement membrane (BM), TexasRed-labelled fluorescent dextran-tracers of increasing size (3 kDa, 10 kDa and 40 kDa) were used to analyze diffusion within low- and semi-matured MCF10A acini. The high levels of autofluorescence displayed by older acini (highly-matured group, day 25 to 35) caused by the apoptotic cells present in the luminar space made the analysis of such group impossible. In a series of preliminary tests, the dextran solution was directly added on the GelTrex-embedded spheres, to observe the diffusion profile through the membrane while making sure that it had not been ruined or partially damaged during the isolation of acini from the EHS matrix. The resulting permeation sequence was clear, and in line with the expectations for such a system (see Fig. 5.3): first, a halo-shaped red fluorescent signal appeared around the acini. Positive laminin-5 colocalization demonstrated that this accumulation was localized in the BM scaffold. Over time, dextran signal started appearing within intercellular cleft regions, and finally inside the cytoplasm of luminal cells. A schematization of the general molecule diffusion sequence can be seen in see Figure 5.3 B.

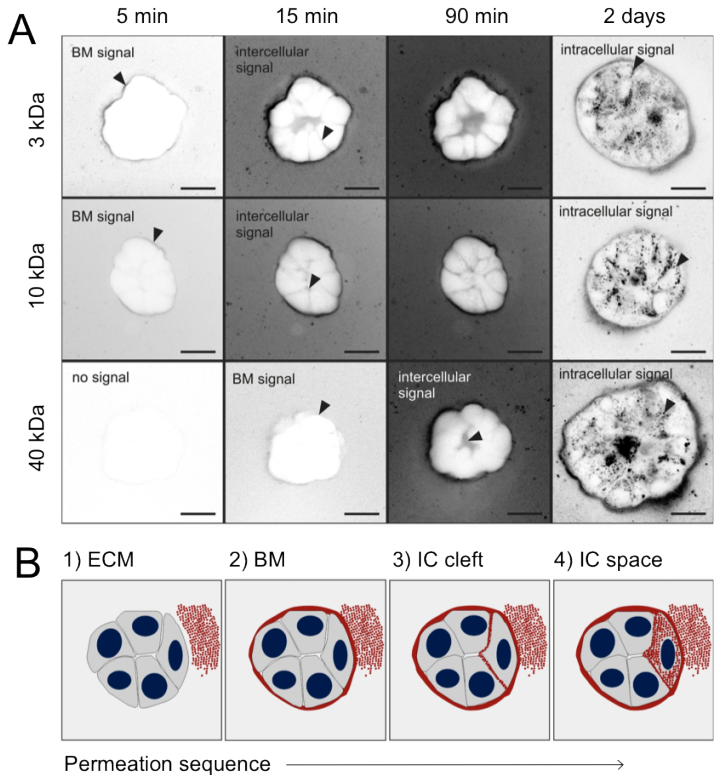

Figure 5.3: A. Representative temporal sequence of the *in situ* permeation of 3, 10 and 40 kDa labelled dextran in young-, mid- and old-matured MCF10A acini embedded in GeTrex. Black arrows indicate the first temporal appearance and spatial localization of dextran. The images are contrast inverted. **B.** Schematization of the molecule influx sequence through the BM and into MCF10A acini. In red: dextran; in grey: cytoplasm; in blue: nuclei. Scale bars: 20 µm. Adapted from [54].

In order to obtain a quantification of this process, though, and analyze the permeation rates of the different dextran molecules through the BM, in the next cycle of experiments MCF10A acini had to be analyzed after isolation from the EHS matrix; were this not the case, data evaluation would be significantly complicated by the necessity to additionally consider diffusion through such a substrate.
After isolation from GelTrex and transfer of the spheres on a cell-culture coated Petri dish according to the protocol described in Section 3.2.5, culture medium was quickly exchanged with a premixed solution of dextran in EGF-free assay medium and the fluorescent signal propagation through the BM was monitored over time. In order to quantitatively analyze the permeation process, the first step lied in the development of a masking algorithm capable of recognizing and dividing the exterior space from the BM boundary and an acini interior (for a detailed description of the method, see Section 3.3.4). The resulting fluorescence intensity values were then averaged for each time point over the whole masked domain (corresponding to the interior of the acini). Given the need to normalize the signal against the background signal, four ROIs were manually selected from each sphere and their fluorescent intensity values were followed over time as well (see Fig. 5.4).

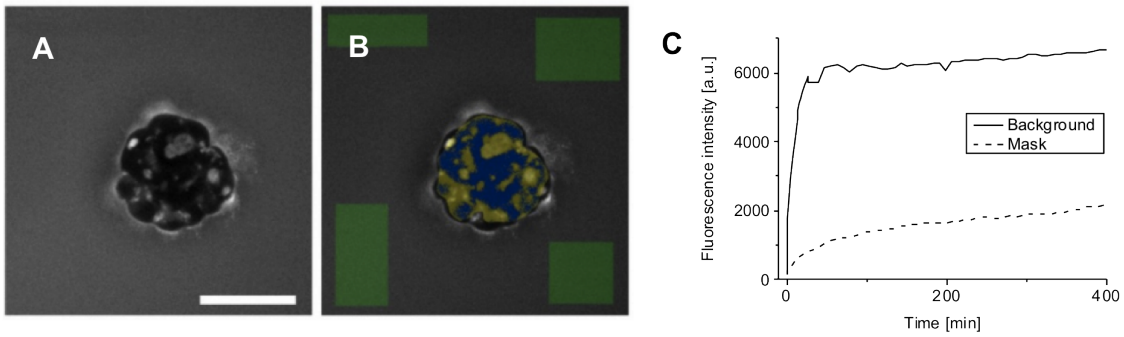

Figure 5.4.: A. Fluorescent signal of TexasRed labelled 40 kDa dextrans permeating through the BM of a highly-matured MCF10A acinus and (**B**) mask used to measure the intensity profile inside the sphere. In blue: TexasRed signal. In yellow: autofluorescence domains. In green: manually selected ROIs. Scale bar: 50 µm. **C.** Corresponding intensity profile recorded over time in the background ROIs and in the blue mask domain, respectively. Adapted from [54].

Given that in order to obtain a precise time course of the fluorescent intensity we were forced to track only a single image plane at the confocal microscope, what we observed was always a quick initial increase in background intensity, followed by the reaching of a plateau concentration. This was simply due to the initial mixing phase of the dextran solution with the thin medium layer remained after aspiration: the diffusion of our

labelled solute in the focal plane was in fact not instantaneous, but occurred at a certain speed. Now, consider a simple model in which two compartments containing different solute concentrations are divided by a semipermeable membrane. For such a system, one can write down the equations for concentration equalization as follows [70]:

$$C(t) = C_\infty + (C_0 - C_\infty)e^{-t/\tau} \tag{5.1}$$

Where, for a given compartment, $C(t)$ is the concentration profile as a function of time, C_0 defines the initial condition ($C_0 = C(t = 0)$) and C_∞ the final one. The time constant τ would then be linked to the permeability constant P of the membrane via formula

$$\frac{1}{\tau} = AP\frac{V_1 + V_2}{V_1 V_2} \tag{5.2}$$

(where A represents the membrane surface, and V_1 and V_2 are the two compartment volumes). In principle, after having obtained τ from fitting Eq. 5.3 to the intensity profile of the dextran tracers permeated within the MCF10A acini, this would allow us to calculate P.

In our case, though, the constant cellular uptake of dextrans is such that one cannot strictly speak of concentration equilibration. Furthermore, neither the osmotically active enclosed volume V nor the BM surface area A could be determined with reasonable accuracy from the experiments. Given such complications, it was not possible to directly extract P from our data; therefore we followed a different approach, fitting the experimental results with an equation describing the time-course of the fluorescent intensity, rather than the dextran concentration:

$$I(t) = I_\infty + (I_0 - I_\infty)e^{-t/\tau} \tag{5.3}$$

and just using the time constants τ as semi-quantitative measure of permeability (the fit results are plotted in Figure 5.5).

The characteristic time constant for the fluorescence intensity increase in the background ROIs (τ_0) and in the interior of the acini (τ) were therefore extracted and compared for each dextran group and acinar maturation stage. Intuitively, τ_0 describes the speed of free diffusion and mixing of the dextran solution on the imaged focal plane, while τ characterizes the combined retardation effect of free diffusion and the BM permeation barrier. By computing the difference $\Delta\tau = \tau - \tau_0$, the permeability speed of different tracer sizes through low- and highly-developed BM scaffolds could be compared in a semi-quantitative manner.

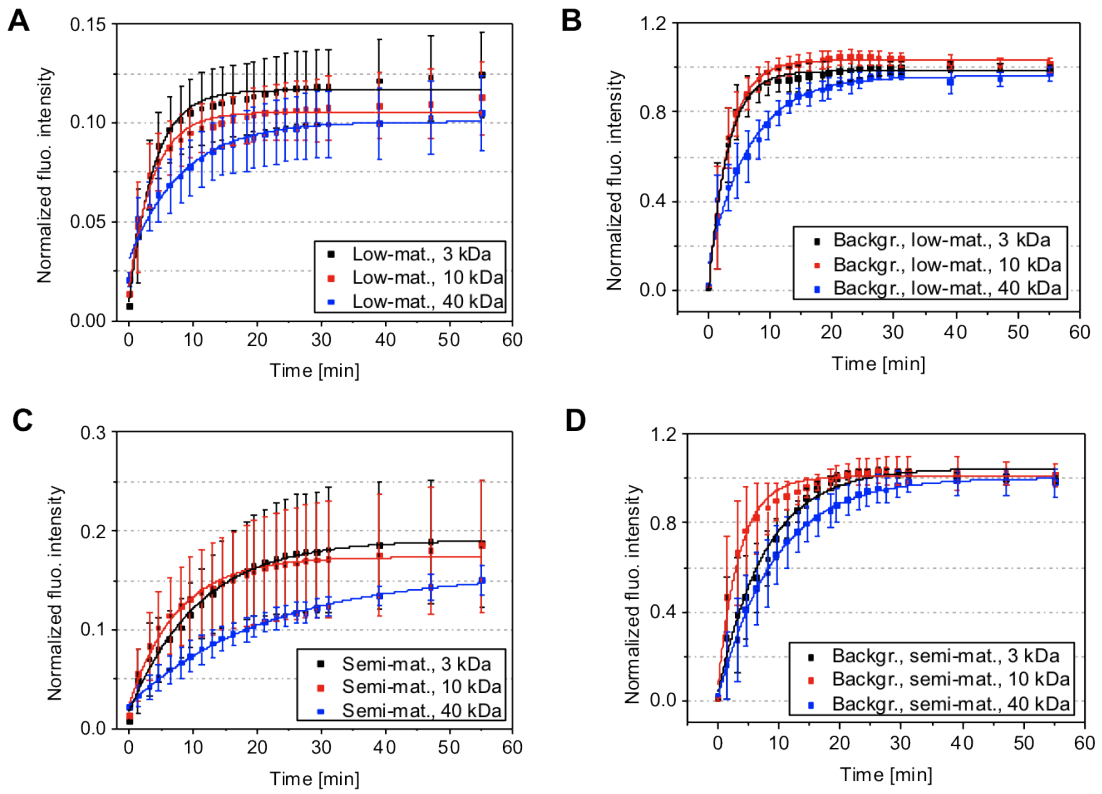

Figure 5.5.: Average fluorescence intensity profiles of (**A**) low-matured MCF10A acini with (**B**) corresponding background and (**C**) semi-matured acini with (**D**) corresponding background. Curves (A) and (C) were normalized to the background plateau for each molecular weight. Mean values with s.d. are shown. The full lines represent fits to the semi-empirical law described by Eq. 5.3. Please note that the absolute signal intensities of low- and semi-matured acini cannot be directly compared because the increased autofluorescence of the second group imposed in this case the use of an adapted masking algorithm. Adapted from [54].

Already this simple approach clearly revealed that low-developed basement membrane scaffolds (low-matured acini group) do not act as permeation barriers: solutes of the lowest molecular weights (3 and 10 kDa) in fact could penetrate through the BM almost as fast as they freely diffuse in solution, as indicated by very low values of $\Delta\tau$ ($\Delta\tau_{3\mathrm{kDa}}$ = 0.7 min; $\Delta\tau_{10\mathrm{kDa}}$ = 0.8 min). A slight retardation effect was only observed in the case of the largest dextrans ($\Delta\tau_{40kDa}$ = 1.8 min) but the differences were not statistically significant (the number of analyzed spheres was N=20 for each dextran size).
In contrast, semi-matured acini clearly acted as size-dependent permeation barriers, as

indicated by the considerably higher values for $\Delta\tau$ (see Table 5.1). This retardation effect peaked for the largest dextrans, with a value of $\Delta\tau_{40\text{kDa}} = 12$ min ($p < 0.001$). The corresponding decrease in diffusion speed for the 40 kDa tracer was about 6.6-fold (semi- versus low-matured group), while values within the highly developed BM sample group indicated a 3.9-fold retardation effect when comparing 40 kDa to 3 kDa tracers. In this case, the number of analyzed spheres was $N_{3\text{ kDa}}$=20, $N_{10\text{ kDa}}$=21 and $N_{40\text{ kDa}}$=18.

Table 5.1.: Diffusion retardation parameters $\Delta\tau$ recorded upon penetration of dextran tracers of different molecular weights through the BMs of MCf10A acini of different maturation stages. Errors are s.d.

	3 kDa	10 kDa	40 kDa
$\Delta\tau$ (low-matured)	0.7 ± 0.6	0.8 ± 0.5	1.8 ± 1.1
$\Delta\tau$ (semi-matured)	3.1 ± 0.7	4.1 ± 0.6	12 ± 0.7

Taken together, this approach clearly confirmed a significant increase in molecule retardation with increasing dextran size and acinar development, pointing at a maturation of the BM which probably affects both its thickness and pore size. Note that 40 kDa dextrans feature a hydrodynamic radius of approximately 9 nm [164]; TexasRed labeled tracers might display a slight variation from this value, but since these molecules were capable to pass through the BM barrier, we expect the BM pore size to lie in a similar range.

5.2.1. Collagenase IV control experiments

To validate the hypothesis that the observed molecule retardation effectively correlates with progressing BM development, experiments comparing the intact and disrupted BM scaffolds had to be performed. To this end, MCF10A acini were treated with collagenase IV to selectively digest their collagen IV meshwork. Interestingly, selective fragmentation of collagen IV also affected the structure of laminin-5 networks; the inhomogeneous staining visible in Figure 5.6 A suggests that collagen IV must be a main structure-lending protein of the BM. Subsequent permeation measurements showed how, in this case, the dextran signal appeared diffuse and fragmentary, no longer resembling the BM-specific halo-like structure found in native acini (see Fig. 5.6 B). Dextran fluorescence was visible both in the BM and acinar interior (intercellular clefts) after only 2 minutes from solution exchange - and independent of the dextran size.

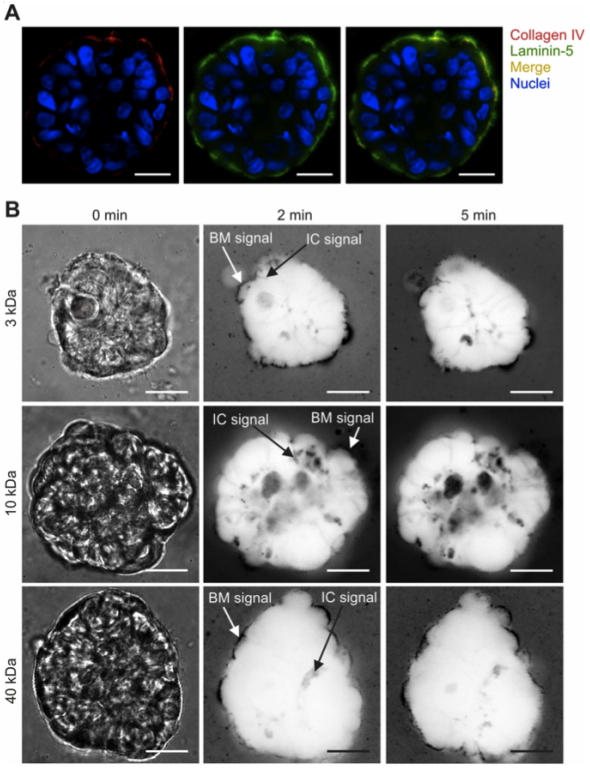

Figure 5.6: Role of intact collagen IV network for size-dependent dextran retardation. **A.** Control immunofluorescence staining of collagen IV (in red) after selective enzymatic digestion by means of collagenase IV and comparative detection of laminin-5 (in green): note the colocalization of the two signals, indicating an overlap between the residual collagen IV network fragments present in the disrupted BM structure and the intact laminin 5 meshwork. **B.** Representative time-lapse images of dextran influx in collagenase IV treated MCF10A acini: the fluorescent signal is independent of both dextran tracer size and BM maturation stage. Left panel (0 min): bright field images. Other panels: contrast inverted images recorded after 2 and 5 min, respectively. IC: Intercellular cleft signal. Scale bars: 20 µm. Source: [54].

5.3. AFM indentation on native and decellularized MCF10A acini

After having addressed the permeation properties of the MCF10A acini, we turned to the study of their mechanical properties: also in this case, one of the first steps to take was that of understanding and isolating the role played by the basement membrane in conferring stability and resistance to such multicellular structures. Numerous types of detergents are known for their capacity of disrupting the lipid bilayers which form plasma membranes: here, octyl-β-D-glucopyranoside (OGP) was used to efficiently break down cell membranes, cell-cell contacts and cell-matrix anchorage while leaving the BM protein scaffolds unaffected [180]. Comparative AFM indentation experiments were then performed on native and OGP-treated acini in order to isolate the contribution of the BM to their mechanical stability.

Directly after OGP application, an immediate and transient overall swelling of MCF10A acini was observed, most likely caused by an increase in osmotic pressure due to cellular breakdown and the release of osmotically active material within the BM shell (see Fig.

5.7 B). After 7 minutes of OGP-incubation, decellularized acini displayed statistically significantly ($p < 0.0001$) larger values of their perimeters P ($P = 227 \pm 59\,\mu m$, $N = 21$), when compared to the corresponding untreated sample ($P = 195 \pm 54\,\mu m$; errors are s.d.). This swelling was accompanied by a progressive process of cellular disorganization, with large clefts appearing over time between the disrupted cell bodies and the BM to indicate the breakdown of cell-matrix connections and the subsequent isolation of BM shells from their interior. Within 30 minutes the swelling reversed, pointing at a likely counter permeation of the macromolecules released during plasma cell fracture. Most visible debris, residual cell nuclei and diffuse F-actin remained inside the acinar structures. In the final, equilibrated state, the acinar sizes had gone back to the original ones. Phase contrast images of the different stages are presented in Figure 5.7 A. In contrast, during OGP treatment BMs always retained their structural integrity: a first indication of this is to be found in the collagen IV signal recorded during immunostainings (see Fig. 5.7 E).

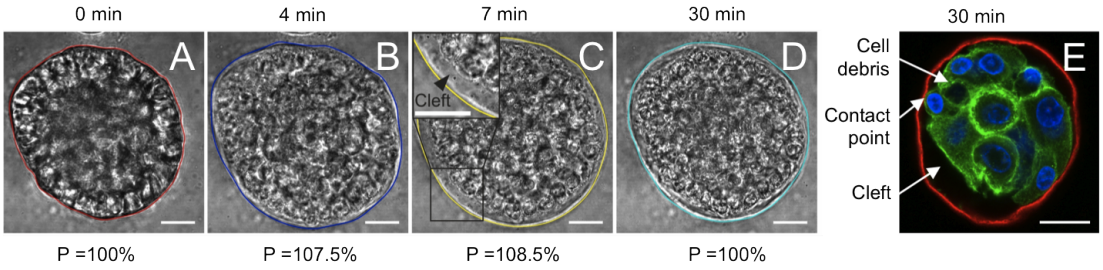

Figure 5.7.: Osmotic swelling and decellularization of an MCF10A sphere induced by treatment with a 1% solution of OGP. **A.** Phase image of the acinus prior to detergent incubation, and then after 4 (**B**), 7 (**C**) and 30 minutes (**D**) of incubation respectively. Percentages indicate the relative change in the sphere's plane-cut perimeter P (marked with colors at each stage). **E.** IF staining showing complete disruption of the cellular architecture and cleavage of cell-matrix connections induced by OGP treatment. In red: collagen IV; in green: F-actin and in blue: nuclei. Scale bar: 20 µm. Source: [54].

After having established a substantial separation of the BM from the acinar cell cluster, AFM indentation experiments were performed on low- and semi-matured acini before and after OGP treatment. Again, the overall elastic response of the analyzed samples was tested by means of fast, successive indentations: for the native acini group, in virtually all cases the raw data curves showed a very precise overlap. Surprisingly, this was the case also for the OGP-treated, semi-matured acini group: only rarely did the AFM indentations lead to a partially plastic deformation. In most cases, curves looked like in Figure 5.8.

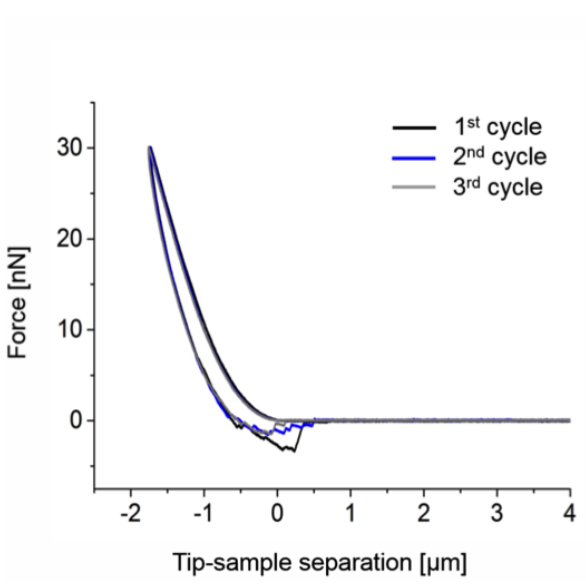

Figure 5.8: Plot showing three consecutive AFM indentation cycles performed on an OGP-treated MCF10A acinus. The almost perfect overlap of successive curves indicated the absence of plastic deformation and an overall elastic behavior of the acinar structures even upon decellularization. Source: [54].

Low-developed acini, though, could not withstand the osmotic swelling induced by OGP treatment: this was in fact sufficient to cause a fracture of the BM for nearly every acinus analyzed, making the AFM measurements impossible due to the high unspecific adhesion forces developing between the indenter tip and the cellular debris. This fact already demonstrated how partially developed BMs offer a much lower mechanical resistance against loads than well-matured ones. Quantitative confirmation of this fact came from the AFM measurements: a representative single AFM cycle performed on the same semi-matured acinus before and after incubation with OGP is given in Fig. 5.9 A. The clear difference observed between the curves already points at an overall softening of the sphere after detergent incubation. A readout of the forces needed to reach certain indentation depths is presented in Figure 5.9 B.

Upon repetition of this procedure for all analyzed spheres, a highly significant ($p < 0.001$) softening of the decellularized BM shell population became evident: native acini expressing a fully matured BM required about 3.9-fold higher indentation forces (5.5 nN $\pm$ 3.8 nN, N = 40) than decellularized samples (1.4 nN $\pm$ 0.6 nN, N = 31; errors are s.d.) to reach an indentation of 1 µm. This effect became even more pronounced at higher indentation depths (see Fig. 5.10) although, even after decellularization, the mechanical integrity of BM shells was retained up to indentation as high as 20 nN.
Since the geometry of the AFM indenter glass sphere used during the experiments is known (radius: 22.3 µm), the force corresponding to a given indentation depth can be

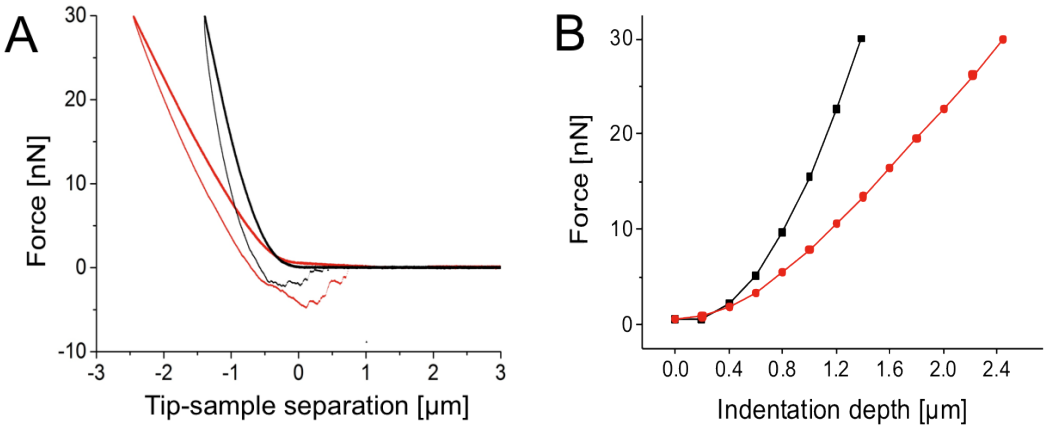

Figure 5.9.: A. AFM indentation cycles as performed on the same 17-days old MCF10A acinus before (black) and after (red) OGP-treatment. The softening of the decellularized sphere is evident. **B.** Force values needed to reach a certain indentation depth into the acinus as directly read from the raw data in (A). Source: [54].

approximately converted in pressure: in the case of maximal load (F = 20 nN for an indentation of 2 µm), the acini withstand a pressure of about 80 Pa. We will see in the following how this value is in line with many physiological situations.

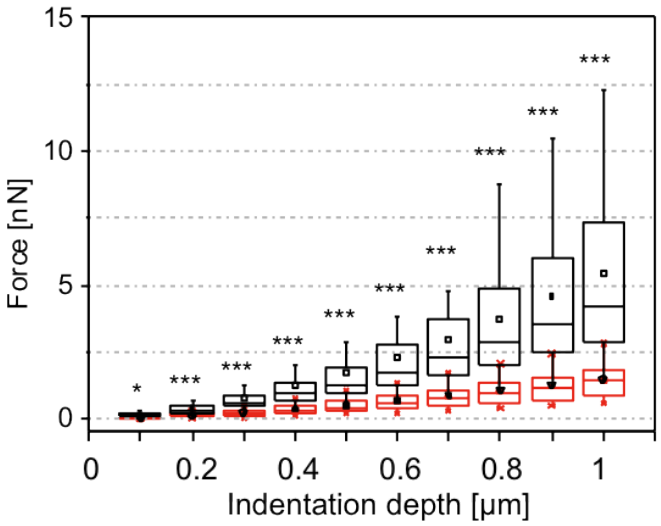

Figure 5.10: Box plot representing the force distributions for increased indentation depths in native (black, N=40) and OGP-treated (red, N=31) MCF10A acini with highly-developed BMs. The differences between the two cellular populations are highly statistically significant, with p-values p(***) < 0.001.

5.4. Basement membrane characterization

Having started to understand what an important role the basement membrane plays in determining the mechanical response of MCF10A spheroids, a more accurate characterization of its properties was a fundamental step. After having established that the overall behavior of BMs is substantially elastic (as shown by the equilibration after the osmotic pressure shock and by the reproducibility of indentation), we were in fact interested in characterizing parameters like membrane thickness and structure, topography and material response.
Some reports describing the nanoscale topography and mechanical properties of other types of BMs are present in literature [167]-[166]-[34]-[130], but no such studies have been performed on the BM of breast glands so far. The techniques used in this section are AFM, SEM and LSM.

5.4.1. AFM imaging and indentation of isolated basement membranes

After isolation of BMs performed according to the protocol described in Section 3.2.6, basement membranes of low- and old-matured MCF10A spheres were characterized by means of AFM contact imaging in PBS to obtain precise information regarding their thickness, topography, and surface roughness. As expected, a large variability was observed between different BMs, underlying once more the high level of heterogeneity characterizing such complex biological samples.
For the low-matured spheres group, 13 different samples were analyzed, isolated from 9 different membranes. Typical image sizes were of 15×15 µm^2: after background flattening, histograms of pixel heights were produced for each image. In some cases, a double layer of BM could be identified: given the three-dimensional curvature of such membranes, in fact, larger fragments that were isolated via centrifugation (i.e. coming form low-matured spheres, see Section 3.2.6) often displayed folds and wrinkles in proximity of the edge. These could be observed both in phase contrast images and during AFM imaging. An example of such an image, and the corresponding multi-peak height histogram, are given in Figure 5.11.
Single height histograms could always be fitted by Gaussian distributions of the form:

$$y = y_0 + \frac{A}{\sigma\sqrt{2\pi}} \exp\Big(- \frac{(x - x_c)^2}{2\sigma^2} \Big) \tag{5.4}$$

where x_c is the distribution center, σ^2 its variance, A a proportionality factor and y_0 an offset term. Distribution widths varied greatly, with the narrowest Gaussians barely

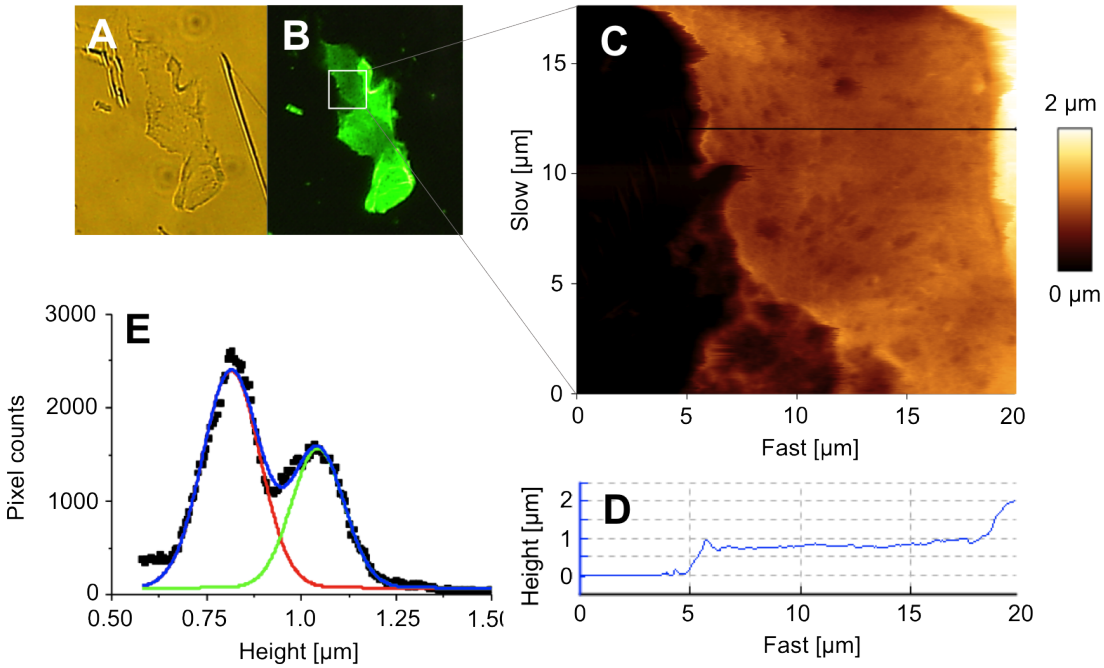

Figure 5.11.: A. Phase contrast and **B.** fluorescent image (staining: collagen IV) of a native BM fragment isolated from a 31 days old MCF10A sphere. **C.** AFM contact image of the flat, intact BM area enclosed in the white inset in (B). The membrane remained fully hydrated during both isolation and imaging, as all measurements were performed in PBS. **D.** Height profile of the black line scan shown in (D) and (**E**) height histogram of image (C). Black dots: pixel counts. Red line: first Gaussian peak fit. Green line: second Gaussian peak fit, caused by the fold of the membrane visible as the whitish area in (C) and as the bright green area enclosed in the white inset in (B).

spanning 100 nm around the center, and the broadest reaching up to σ= 750 nm. Especially BMs isolated from older spheres where found to have very broad height distributions. This fact could point towards a higher heterogeneity of such membranes when compared to the younger ones; but, conversely, it could also just indicate a poorer quality of measurements. The method employed for isolating older BMs, in fact (a peel-off performed by means of glass microcapillaries, see Section 3.2.6) is intrinsically less reproducible than the one used for younger spheres (which were literally broken apart by centrifugations at 13500 rpm). Due to the difficulty of maneuvering the micromanipulators controlling the glass capillaries with sufficient precision, in fact, local scratches and fractures of the isolated BMs could not always be avoided. Also, it was hard to ensure that only perfectly flat BM fragments would adhere to the Petri dish; at times, slight wave-like patterns could be observed on the samples. Figure 5.12 shows the surface topography of a 15×15 µm^2 BM portion.

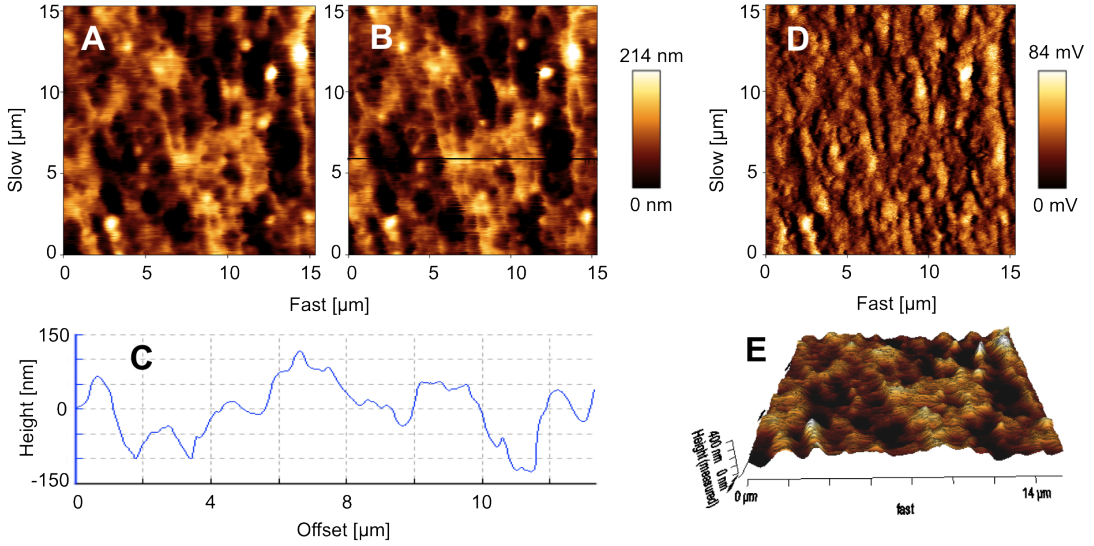

Figure 5.12.: A. Contact image of a 15×15 µm^2 portion of a BM surface in PBS. The trace image appears practically identical to the retrace image (**B**), indicating the correct setting of all imaging parameters. **C.** Height profile of the black line scan shown in (B). **D.** Error image of the same BM portion and (**E**) 3D reconstruction of the surface topography.

Overall, though, despite such difficulties and the relatively low number of samples analyzed, a clear difference could be measured between the thickness of membranes at different stages of maturation: averaging over the distribution centers x_c, a value of 204 ± 97 nm was obtained young BMs (N=13), and of 660 ± 265 nm for the older ones (N=6; errors are s.d.). Gaussian fits of the height histograms of BM images are presented in Figure 5.13. This trend indicates an overall thickening of the basement membrane as acini progress in their development. The recruiting of collagens from the EHS-medium in which the spheres are cultivated only accounts for a part of such growth; immunostainings performed with anti-human laminin 5, in fact, confirmed that the proteins forming the BM are at least partly secreted endogenously. Surely this observation is in line with the retardation effect measured for high molecular weight dextrans (40 kDa) when permeating through older BMs.

Unfortunately, given the challenging nature of this sample from the point of view of AFM imaging (it is very soft, not always adhering perfectly to the substrate and at times still retaining small debris and adhesive cellular components not completely eliminated by the OGP washing step), a thorough RMS_{rough} study could not be performed. It would be interesting to assess whether breast gland BMs display side-specific organization, as

is the case, for instance, for retinal internal limiting membranes [34]-[166].

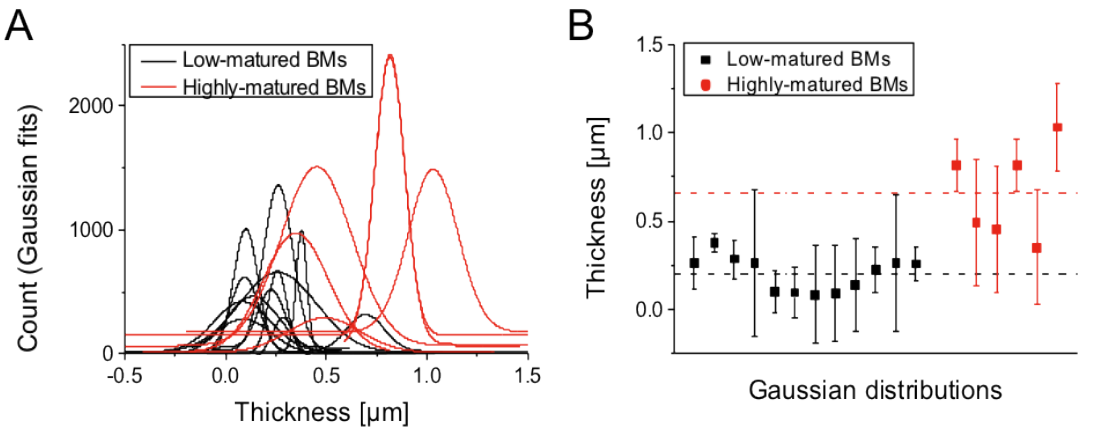

Figure 5.13.: A. Plot showing all the single Gaussian distributions fitted on the height histograms of AFM topographical images of isolated BM fragments. In black: low-matured BMs (N=13); in red: highly-matured BMs (N=6). **B.** Plot showing the centers x_c and full widths at half maximum (FWHM=2.355 σ) of the Gauss distributions plotted in A. Black dotted line: average value of the young matured BM's x_c. Red dotted line: same average for highly-matured BMs.

In our case, only few images offered a resolution sufficient to a RMS_{rough} estimation: mean values for the 5×5 µm^2 portions analyzed to this end were of 46 ± 4 nm and 70 ± 9 nm for low- and highly-matured BMs, respectively (N=3 in both cases. Errors are s.d.). Although these data are not sufficient to draw any conclusion, we at least have a first idea about the substantial similarity of surface roughness between the two groups.

The last step in our AFM characterization of basement membranes consisted of indentation experiments in the form of force maps: after having characterized the average thickness h of a BM via imaging, approach-retraction cycles would be performed at every position of a certain pixellated scan area. An example of a force map is presented in Figure 5.14. Once more, the good overlap of successive indentation curves gave a first indication of the applicability of the Hertzian elastic theory for analysis of basement membrane's Young's moduli (see Fig. 5.15 A). Given the very thin and flat nature of such samples, though, we could not possibly use the equations describing the penetration of a sphere in a semi-infinite elastic space. Instead, we adopted the thickness-corrected model developed for thin layers and described in Section 2.2.1. Because of the geometry of the indenter used, the force-indentation relation chosen for fitting the experimental curves was Equation 2.10. In this case, the fit range was limited to 50 nm: a typical fit

is shown in Figure 5.15 B.

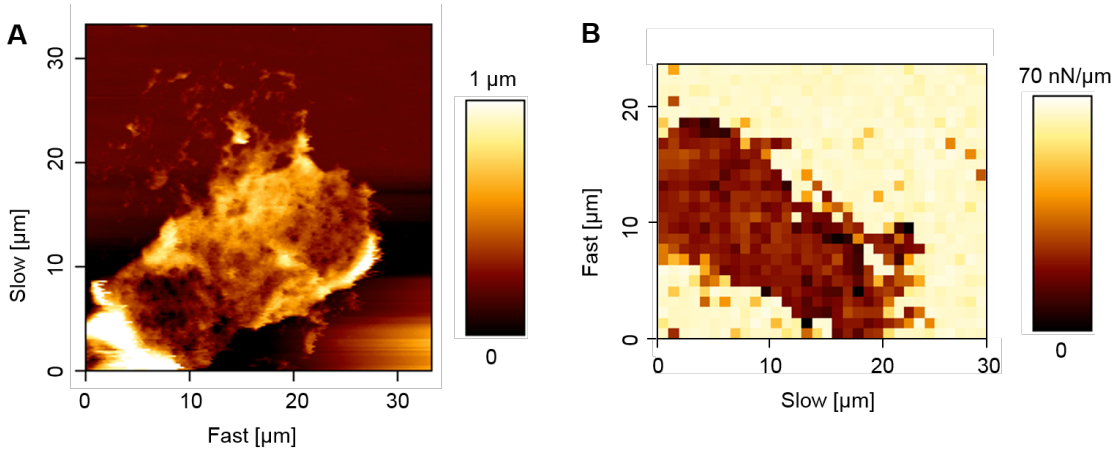

Figure 5.14.: A. Contact-mode imaging of an isolated fragment of BM in PBS and (**B**) corresponding force-map (one force-indentation curve per pixel). The tip indentation speed was held to v =5 µm/s for imaging (f setpoint: 1.5 nN) and v =2 µm/s during indentations (f setpoint: 5 nN). The scale indicates the slope of the linear domain of the approach curve.

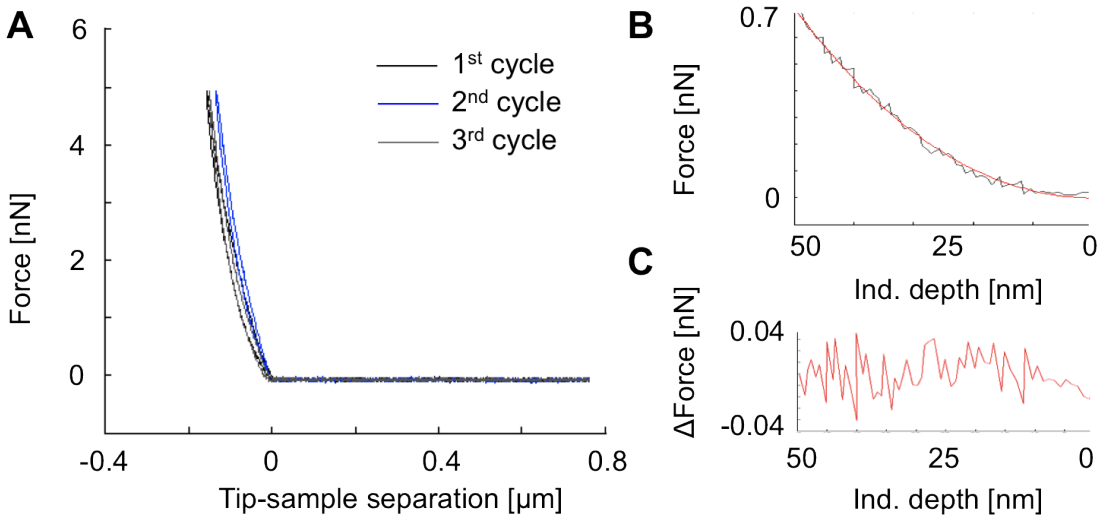

Figure 5.15.: A. Plot showing 3 consecutive indentation cycles recorded on an isolated fragment of basement membrane: the very precise overlap of the curves hints at an overall elastic response of the material. **B.** Plot showing the first 50 nm of an indentation curve (in black) with the corresponding fit of Eq. 2.10. **C.** Fit residuals.

Force maps recorded on BMs at different maturation levels ($N_{low\text{-}mat.}$=4, $N_{highly\text{-}mat.}$=3), were thus analyzed as thin elastic layers in order to obtain the Young's moduli E. For highly matured BMs, the data set of all fitted E ($N_{highly\text{-}mat.}$=543) followed a log-normal distribution characterized by med(E)=395 kPa and σ^*=2.09. The distribution of Young's moduli obtained for low-matured BMs, instead, could not be readily described as log-normal. Nonetheless, it displayed an almost 100-fold decrease in Young's modulus, with values of med(E)=3.5 kPa and σ^*=3.07 ($N_{low\text{-}mat.}$=932).
Although in this case the two groups of samples could not consistently be measured with the same cantilever (and are therefore possibly subject to systematic errors), the very strong differences observed are a further indication of the maturation and differentiation process that BMs undergo during their development.

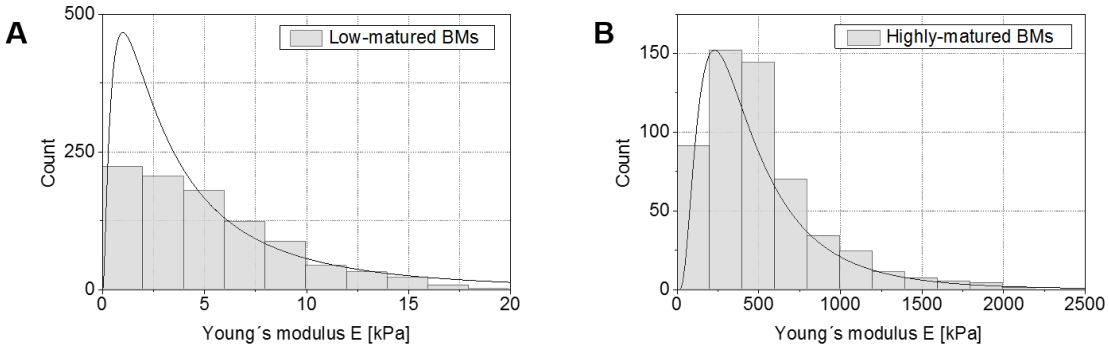

Figure 5.16.: Histograms of the Young's moduli E obtained by fitting Eq. 2.10 to indentation curves recorded on (**A**) low-matured and (**B**) highly-matured isolated BMs. Straight lines: corresponding log-normal distributions.

5.4.2. SEM imaging of isolated basement membranes

Surface analysis by means of AFM is a precious source of information regarding membrane's topography and structure, but given the soft nature of such a specimen it is hard to obtain high resolution images. To identify the ultrastructure of BMs, isolated samples were observed via scanning electron microscopy. Some exemplary images are presented in Figures 5.17 and 5.18. During specimen preparation, critical point drying is employed to dry out the sample in absence of surface tension, which would otherwise easily damage the nanostructure of fragile biological samples [165]. In spite of this, in our case the delicate membranes presented fractures and holes in numerous points following handling and preparation. This is perhaps due to the fact that the BM fragments derived from spheres only 8-10 days old, because of the difficulty in isolating older ones.

This inconvenience though revealed the "backbone" of the protein network: very often an intricate meshwork creating pores of few micrometers in size could be observed, formed by thick bundles of what we assume to be collagen IV. Despite the sparse presence of lipid and cellular residues that could not be completely eliminated, within this structure lending polymer network a finer, thinner net of individual fibers could be seen. Although biological specimens are known to shrink at least 20-30% in volume during the dehydration process necessary for SEM preparation, this "pore size" is still compatible with the grooves observed in the AFM images (typically around 2 µm). Unfortunately, the information obtained through such measurements is not quantitative: neither membrane thickness nor typical mesh size can be assessed in a sensitive manner. The high resolution that can be obtained during imaging, though, gives a more precise idea about the nature and structure of this thin layer of material, so relevant in determining the mechanical properties of breast glands.

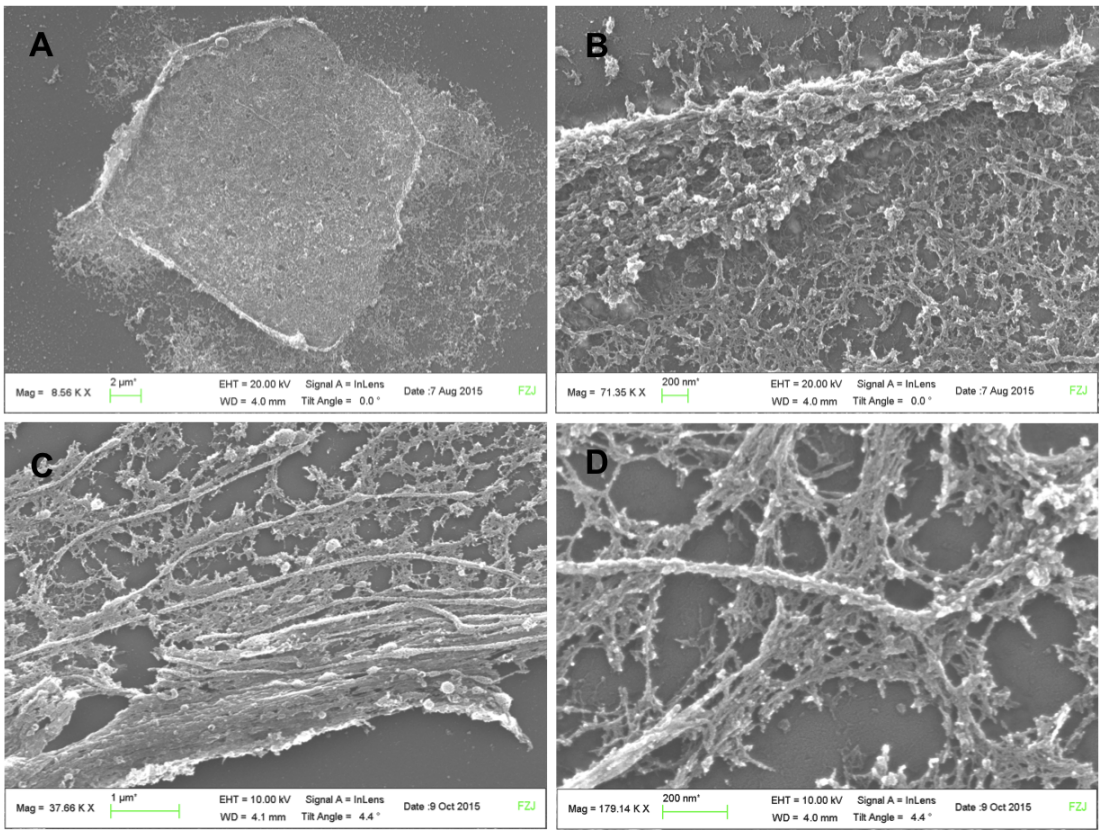

Figure 5.17.: SEM micrographs displaying (**A**) the overview of an isolated BM (day 9) laying flat on the substrate and (**B**) a zoom-in on a side fold. **C.** shows a series of thicker fiber bundles which we hypothesize being formed of type IV collagen. In (**D**) a zoom-in on one such fiber interconnected with the rest of the meshwork is presented.

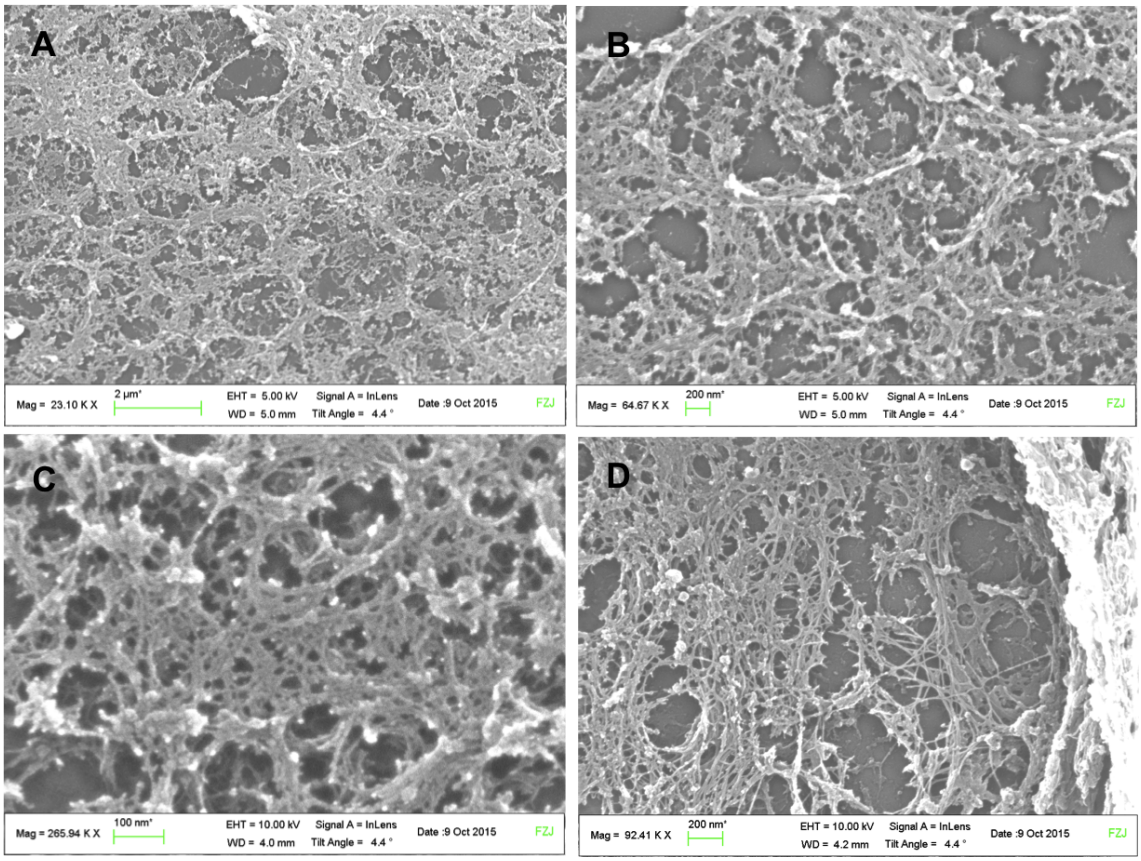

Figure 5.18.: SEM micrographs displaying (**A**) a series of regular, pseudo-hexagonal bundles of fibers constituting the backbone of the BM and (**B**) a zoom-in of (A). (**C**) and (**D**) show zoom-ins on the finer fiber structure composing the BM network.

5.4.3. Basement membrane fluorescent imaging with superresolution Airy scan microscopy

Characterizing BMs from isolated live MCF10A highly-matured acini by means of superresolution Airy scan microscopy revealed the network structure of collagen IV, not otherwise visible by means of traditional fluorescence imaging. Via image processing (for description of the algorithm, see Section 3.3.1) it was possible to measure the distribution of the network's pore sizes, presented in Figure 5.20. This roughly centers around $0.2\,\mu m^2$ (the log-normal distribution parameters are med(area)=$0.22\,\mu m^2$ and σ^*=2.22). In this case, the number of analyzed membranes was N=2 and the number of detected pores N=1682. Interestingly, the network structure is resemblant of the surface organization observed via AFM imaging, both in terms of morphology and size: comparative

images are presented in Figure 5.19 A and 5.19 B.
Note that the BM shown in Figure 5.19 lies so flat on the glass substrate because the acinus it belongs to is being pressed via an AFM-like indentation at the time of imaging (for details, see Section 3.4.7).

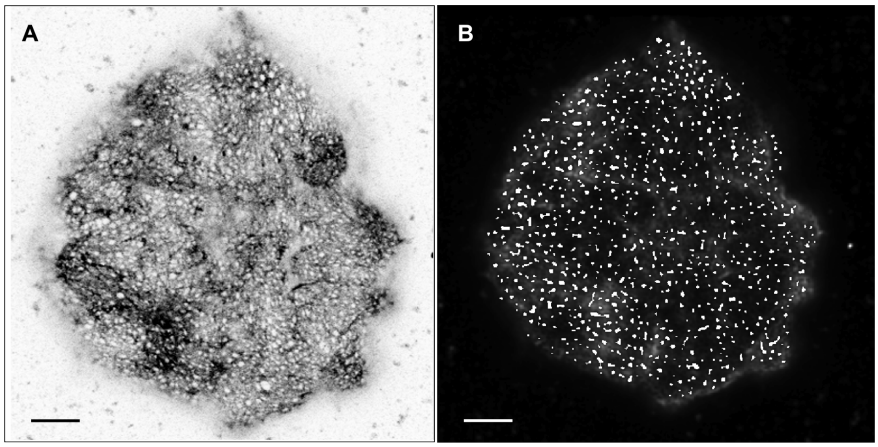

Figure 5.19: **A.** Superresolution image of the collagen IV staining of a native BM. **B**. collective mask used to determine pore sizes. Scale bar: 15 µm.

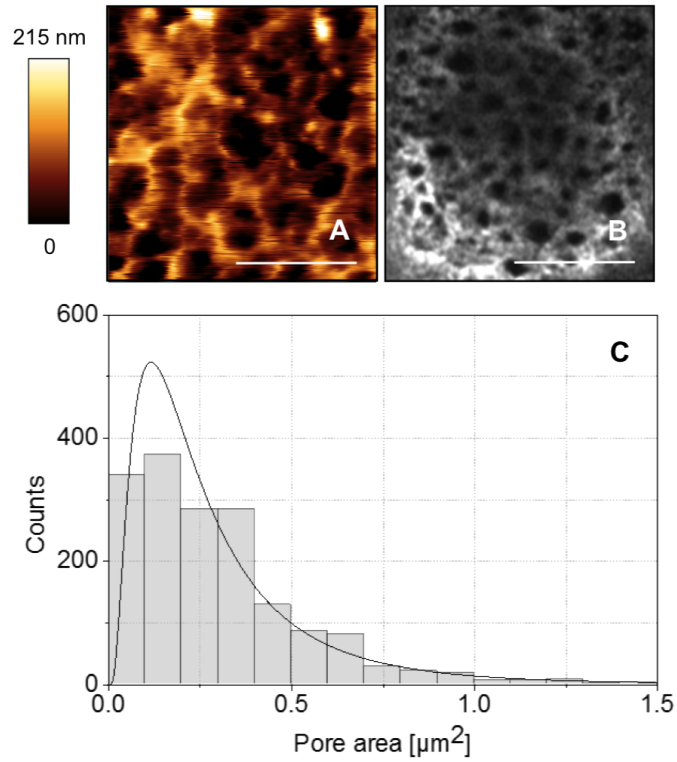

Figure 5.20: Comparison of (**A**) AFM imaging of an isolated BM and (**B**) immunofluorescence staining of the collagen IV network in a native BM. Scale bar: 5 µm. **C**. Log-normal distribution of the sizes of pores identified in the collagen IV network of highly-matured BMs after immunofluorescence staining. For details on the masking algorithm, see Section 3.3.1.

5.5. The role of maturation for the mechanics of MCF10A acini

As a next step of analysis, AFM indentations on whole spheres were performed in order to characterize possible biomechanical differences arising during the acinar maturation process. Prior to measurements, MCF10A spheroids were isolated from the EHS-matrix bed according to the protocol described in Section 3.2.5 and transferred on hard substrates. The cantilever was modified by attachment of a bead having a radius of 22.3 µm. All experiments were performed under physiological conditions in HEPES-buffered EGF-free medium.

5.5.1. Comparison of raw force indentation data of MCF10A acini

At first, raw force-indentation data were compared for all measured spheres; an overview of the results is shown in Figure 5.21. On average, significantly less force was necessary to indent highly-matured spheres than low- or semi-matured ones. For instance, an average force of 1.5 ± 1.4 nN was needed to indent old acini up to a depth of 1 µm, against the 3.5 ± 2.0 nN for the young and 2.9 ± 1.9 nN for the semi-matured groups (errors are s.d. Throughout this section, the number of analyzed spheres is $N_{low\text{-}mat}$=91, $N_{mid\text{-}mat}$=209, $N_{highly\text{-}mat}$=131).
Despite all indications pointing towards a thickening and stiffening of the BM with progressing development, we here find that highly-matured acini, *as a whole*, are softer than both younger groups. This fact is most intuitively simply due to lumen formation, and indicates how the presence of a hollow space necessary for lactation dramatically alters the biomechanical properties of breast gland acini.

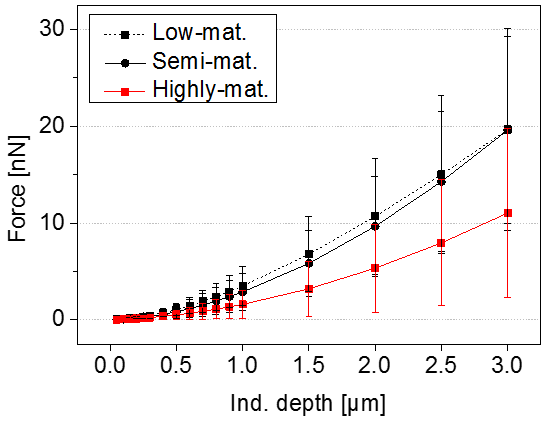

Figure 5.21: Plot showing the average forces needed to reach indentation depths up to 3 µm in MCF10A acini of different maturation grades. Error bars are s.d.

The large variance of the experimental data in this case should not surprise. The sample population is given by complex, heterogeneous three-dimensional structures formed by multiple types of materials. Variations in factors like BM thickness, sphere radius or degree of lumen formation are unavoidable and very hard to control. The large sample size analyzed, though, allowed to average out such effects and identify significant shifts between force distributions; a clearer representation of the latter is offered in Figure 5.22.

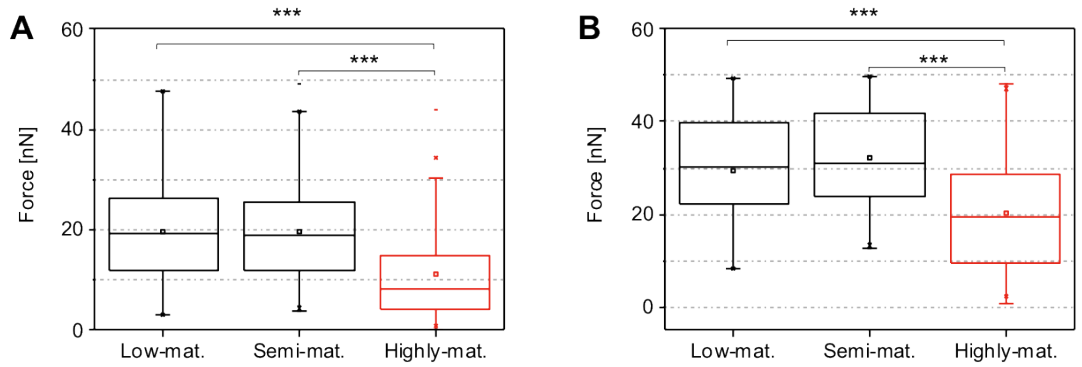

Figure 5.22.: Box plots showing distributions of the forces needed to reach an indentation depth of (**A**) 3 µm and (**B**) 5 µm in MCF10A acini of different maturation grades. For 3 µm, $N_{low\text{-}mat}$=91, $N_{semi\text{-}mat}$=209, $N_{old\text{-}mat}$=131. For 5 µm $N_{low\text{-}mat}$=57, $N_{semi\text{-}mat}$=112, $N_{old\text{-}mat}$=106. The sample of analyzed acini was the same in both cases; given a force setpoint of 50 nN, though, not all spheres could be indented up to 5 µm, hence they do not appear in plot (B). P-values are p(***)<0.001.

Among the distributions of forces needed to reach an indentation depth of 3 µm, for instance, no significant difference was observed between low- and semi-matured acini (displaying the nearly identical mean force values of 13 ± 6 nN and 13 ± 7 nN, respectively), but both groups had a p-value <0.001 when compared to the highly matured sample (whose mean force value was of 7 ± 5 nN, 47% lower than for the other groups). The same trend was observed for indentation depths of 5 µm, with a relative decrease in indentation forces of about 33%.

5.6. Comparison of healthy and malignant breast gland acini

As a next step, MCF10A spheroids were compared with three-dimensional cultures of MDA-MB-231, a highly invasive breast tumor cell line known, on the single cell level, to be much softer and more viscous than its benign counterpart [134]. When cultivated on EHS-matrix gels, such cells also form 3D agglomerates, but the fine organization of polarity, lumen formation and BM secretion displayed by MCF10A is in this case completely lost [55].
AFM-based microrheology experiments have revealed significant differences in the viscous response between the two cell lines [114] and variations in elasticity of about 20% to 35% have been recorded using AFM indentation experiments or MEMS-resonant sensors to measure cellular stiffness, respectively [116].
Here, at first we compared raw AFM force-indentation data: in line with the results obtained in literature for the case of single cells, the difference between the two groups was indisputable. The forces needed to reach depths of up to 5 µm were systematically even lower than those for old-matured MCF10A. Given that MDA-MB-231 3D agglomerates form no lumen at all, though, from a morphological perspective the best MCF10A age group to compare them with is that of low-matured spheres, which display a thin and not fully developed BM. Box plots showing the measured force distributions (along with a zoom-in of the plot for the indentation depth of 0.05 µm) are presented in Figure 5.23, and the corresponding mean values are reported in Table 5.2. The number of analyzed MDA-MB-231 3D spheroids was N=55.

Table 5.2.: Table showing mean values of force distributions (± s.d.) recorded during indentation experiments on 3D cell cultures of MDA-MB-231 and MCF10A acini.

Ind. depth [µm]	Force [nN]			
	MDA-MB-231	**MCF10A**		
		Highly-mat.	Mid-mat.	Low-mat.
0.05	0.006 ± 0.005	0.020 ± 0.017	0.030 ± 0.025	0.027 ±0.025
1	0.6 ± 0.4	1.5 ± 1.4	2.9 ± 1.9	3.5 ± 2.0
2	2.0 ± 1.1	5.3 ± 4.5	9.7 ± 5.2	10.6 ± 5.0
3	4.0 ± 2.3	11.0 ± 8.7	19.0 ± 9.0	19.7 ± 10.0

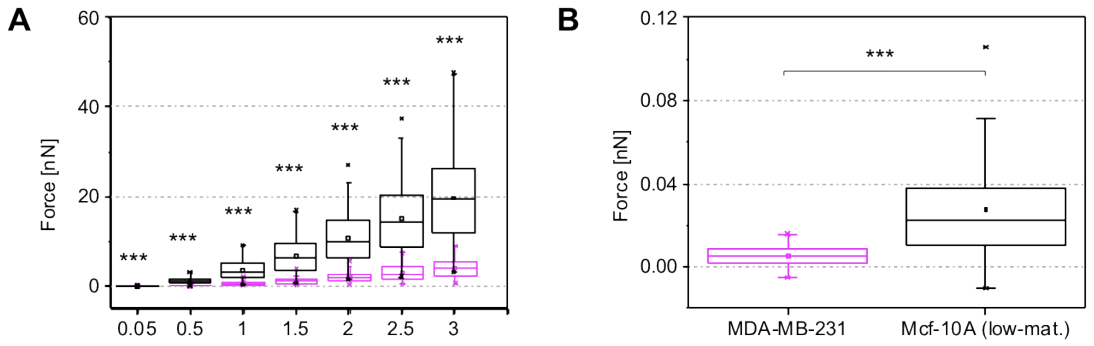

Figure 5.23.: A. Box plots showing distributions of the forces needed to reach different indentation depths on low-matured MCF10A acini (in black) and 3D cell cultures of MDA-MB-231 agglomerates (in magenta). **B.** Zoom-in of the lowest indentation depth value (0.05 µm). p-values are p(***)<0.001.

Such large differences in the behavior of healthy vs. tumorogenic cell lines, besides fully confirming the trend reported in literature for single cells, possibly offer an additional hint towards the relevance of the BM in conferring structural stability to breast glands.

5.7. Beyond Hookean elasticity: hyperelastic models

After analyzing the raw indentation data, fitting of AFM force-distance curves to three different hyperelastic models was performed. The equations presented in Section 2.3.4 for the uniaxial loading of rigid spherical indenters to a Fung (Eq. 2.43), an Ogden (Eq. 2.42) and a Mooney-Rivlin (Eq. 2.40) material were fitted via a least-square method to the indentation portion of all measured AFM curves.
The resulting material parameters distributions for MCF10A acini at different maturation levels, as well as of MDA-MB-231 3D agglomerates, are presented in the following section. Figure 5.24 displays a comparison of the three fitting methods when applied to the same, representative force-distance curve. As can be seen, no major difference in fit residuals is observed for the chosen fit range (1 µm), although some differences will arise for larger indentation depths.

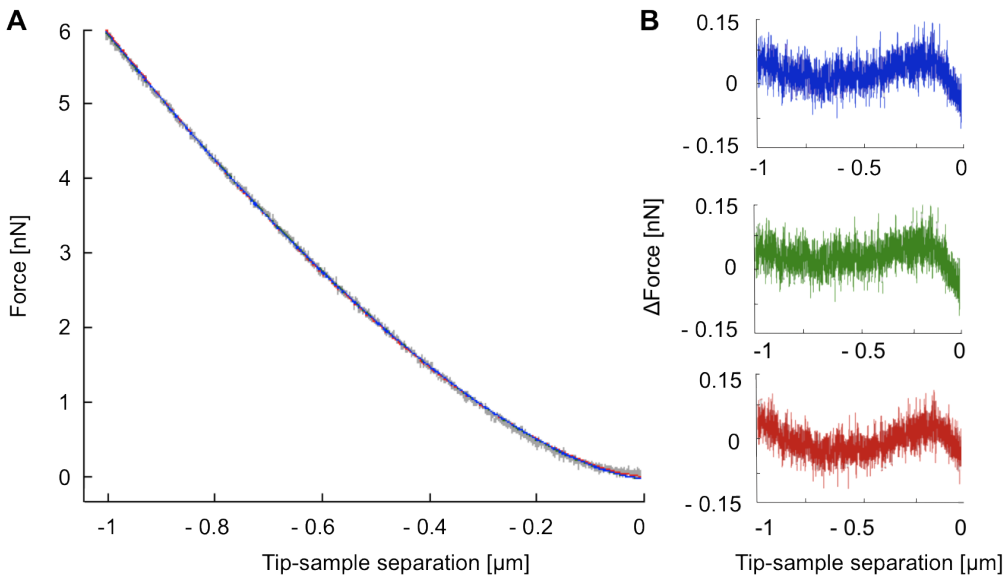

Figure 5.24.: A. Fitted portion (1 µm) of a force-distance curve recorded on an MCF10A spheroid. In gray: original data. In blue: Ogden model. In green: Fung model. In red: Mooney-Rivlin model. The contact point was determined via the third derivative method described in Section 3.4.4. **B.** Corresponding fit residuals.

Fung model

The first analyzed hyperelastic material model was the one developed by Y.C. Fung to describe the elastic properties of soft tissue [159]. Equation 2.43 was fitted to the indentation portion of AFM force-distance curves using increasing fit ranges in order to assess the sensitivity of the material parameters E_0 and b upon indentation range. Recall that, here, E_0 represent a sort of instantaneous Young's modulus, and b is a semi-empirical stiffening exponent.

Figure 5.25 offers an overview of the distributions of E_0 and b for semi- and highly-matured acini. A zoom-in of the results obtained for a fit range of 3 µm is presented in Figure 5.26: the fit parameter E_0 is distributed log-normally, with median values of 223 $\cdot$ 3.65 Pa for the low-matured group, 294 $\cdot$ 2.06 Pa for the semi-matured and 115 $\cdot$ 2.98 Pa for the highly-matured one (errors are multiplicative s.d. σ^*).

A clear and statistically significant shift is present between such elasticity distributions, indicating how, despite the effect of BM stiffening and thickening already reported, the process of lumen formation in this case is the main determinant of the mechanical properties of MCF10A spheroids; this notion is intuitively confirmed by the fact that the differences grow with increasing indentation depth. Although we always remain in a

regime of small, superficial indentations (roughly up to 5 µm), such AFM measurements nonetheless allow a sort of "global" probing of our cellular structures, given that they record differences between samples whose main morphological difference lies in the structure of their interior.

The exponent b, on the other hand, shows a higher level of uniformity with increasing indentation depth, reaching nearly identical distributions for a fit range of 3 µm: in this case, b=15 ± 7 for semi-matured acini and b=16.5 ± 5 for highly-matured ones (errors are 95% confidence intervals). The corresponding p-value was p=0.3.

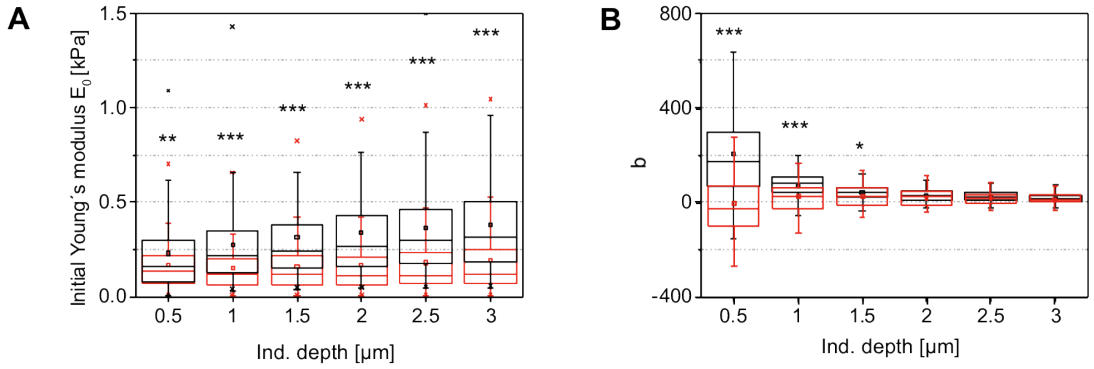

Figure 5.25.: A. Initial Young's modulus E_0 and (**B**) corresponding stiffening exponent b obtained by fitting Fung's model (Eq. 2.43) to different portions of AFM force-indentation curves recorded on mid-matured (black) and highly-matured (red) MCF10A acini. The p-values are p(*)<0.05, p(**)<0.01 and p(***)<0.001.

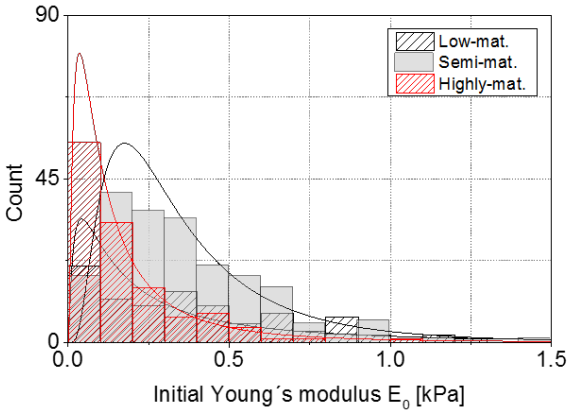

Figure 5.26: Histograms of initial Young's moduli E_0 obtained by fitting Fung's model (Eq. 2.43) to AFM force-indentation curves of low-, semi- and highly- matured MCF10A spheroids. Plotted lines: corresponding log-normal distributions. Fit range: 3 µm.

Ogden model

Successively, analyses were repeated using the Ogden material model (Eq. 2.42) as a fitting function. The results obtained were remarkably similar to the previous case: again, a significant shift was recorded in the initial elastic modulus of semi- and highly-matured MCF10A spheroids (see Fig. 5.27 A), and again the second fitting parameter (α) showed increasingly similar distributions with increasing indentation depths (Fig. 5.27 B). Median values for the log-normal E_0 distributions were of $215 \cdot 3.55$ Pa for the low-, $257 \cdot 2.09$ Pa for the semi- and $108 \cdot 4.74$ Pa for the highly-matured group (errors are multiplicative s.d. σ^*). These results indicate the substantial similarity of the two models in describing soft tissues, despite the differences in their formulation.

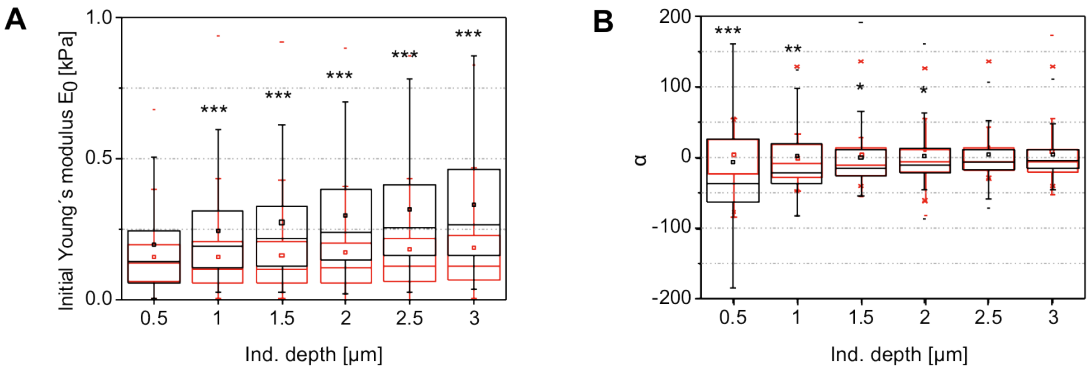

Figure 5.27.: A. Initial Young's modulus E_0 and (**B**) corresponding Ogden exponent α obtained by fitting Eq. 2.42 to different portions of AFM force-indentation curves recorded on mid-matured (black) and highly-matured (red) MCF10A acini. The p-values are p(*)<0.05, p(**)<0.01 and p(***)<0.001.

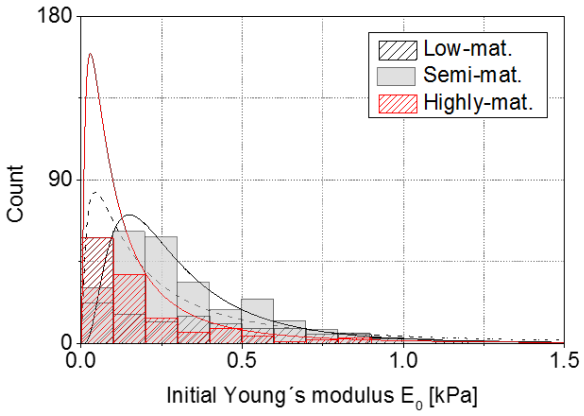

Figure 5.28: Histograms of initial Young's moduli E_0 obtained by fitting Ogden model (Eq. 2.42) to AFM force-indentation curves of low-, semi- and highly- matured MCF10A spheroids. Plotted lines: corresponding log-normal distributions. Fit range: 3 µm.

Mooney-Rivlin model

Finally, we performed fits of the Mooney-Rivlin model (Eq. 2.40) in order to compare this approach with the previous ones. This time, at indentation depths higher than 1 µm the fit started failing. The reason for this was an additional constraint that we needed to impose upon the free fit parameters B_1 and B_2. Because of the condition:

$$B_1 + B_2 = \frac{20E_0}{9\pi(1-\nu^2)} \tag{5.5}$$

in fact, B_1 and B_2 could not freely vary as their sum had to fulfill the condition that E_0 be positive. For this reason, only parameter values obtained via fits of the first 0.5 µm are reported in Figure 5.29.

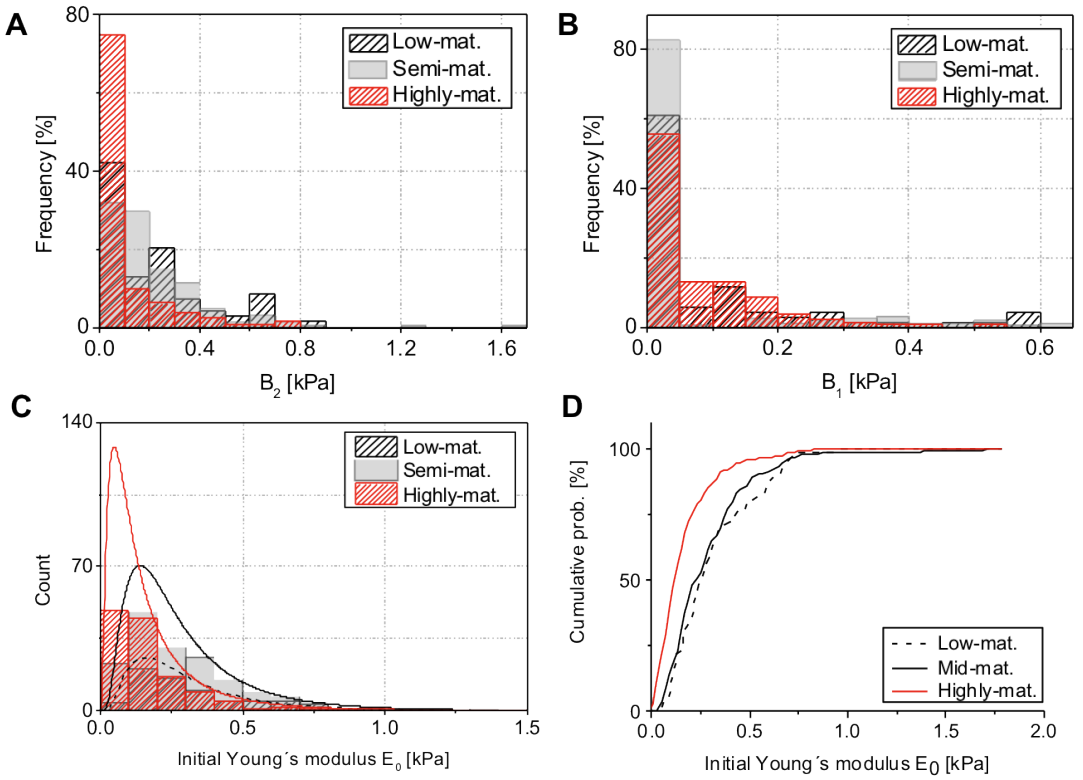

Figure 5.29.: Histograms of Mooney-Rivlin material parameters (**A**) B_1 and (**B**) B_2 obtained from fitting Eq. 2.40 to AFM force-indentation curves on MCF10A acini. Fit range: 0.5 µm. **C**. Instantaneous initial Young's moduli E_0 calculated from Eq. 2.41 with corresponding log-normal distributions and (**D**) cumulative histograms.

Even in this case, though, the same trend regarding semi- and highly-matured spheres

was observed, with a significant shift in instantaneous elastic modulus. Table 5.3 presents the mean values of the B_1, B_2 parameter distributions obtained from curve fitting, and of the corresponding E_0 distributions calculated from Equation 5.5.

Table 5.3.: Mean values of parameters distributions obtained from fits of the Mooney-Rivlin model (Eq. 2.40) to AFM indentation curves. Errors indicate 95% confidence intervals.

	Low-matured	Semi-matured	Highly-matured
B_1 [Pa]	94 ± 37	62 ± 22	77 ± 18
B_2 [Pa]	203 ± 53	212 ± 33	81 ± 25
E_0 [Pa]	319 ± 49	294 ± 31	168 ± 25

Elasticity of MDA-MB-231 3D cell cultures

To conclude, in Figure 5.30 we present the distributions of the initial Young's moduli E_0 of MDA-MB-231 3D cell cultures as calculated via the three above-discussed models. In all cases, the invasive cell line displayed elasticity values that were statistically significantly lower than those of low-matured MCF10A spheroids ($p<0.001$). The fit range was held to 3 µm for the Fung and the Ogden model, and to 0.5 µm for the Mooney-Rivlin model.

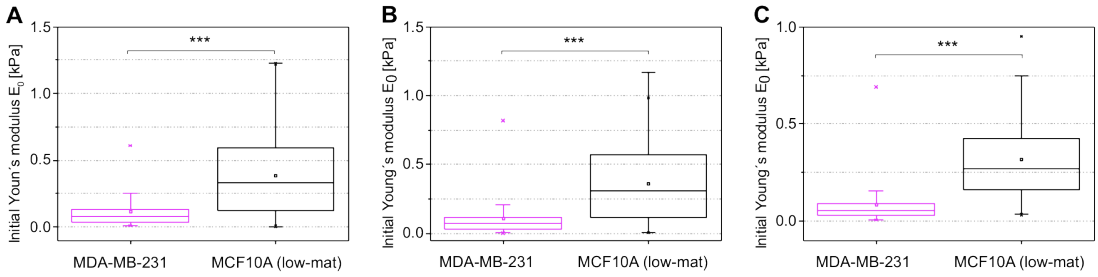

Figure 5.30.: Box plots of the distributions of E_0 of MDA-MB-231 and low-matured MCF10A 3D cell cultures as calculated from (**A**) the Fung model, (**B**) the Ogden model and (**C**) the Mooney-Rivlin model. p-values are $p(***)<0.001$.

5.8. Finite element simulations

In order to validate the application of hyperelastic models to the experimentally derived AFM force-spectroscopy curves, a finite element simulation of the indentation of an MCF10A acinus was set up.
Given that AFM indentations never exceeded 5-6 µm, we could work in the approximation of small deformations and consider each acinus as a half-infinite space having the material parameters obtained from the fits. The model of choice in this case was the Mooney-Rivlin material: this is just due to the software suite used for implementing the simulations. When defining an Ogden material model in the FEBio PreView package, in fact, the first six terms in the summation of Equation 2.32 are required. Similarly, for the accurate definition of a Fung (orthotropic) material, knowledge of the defining material parameters along the three cartesian directions is necessary. Given the impossibility of retrieving such information from our experiments, we limited this step of analysis to the case of a Mooney-Rivlin material. In the future this analysis could and should of course be extended; but due to time restrictions this has not been possible yet.
Given the large variance of the obtained parameters, we characterized the three different MCF10A maturation groups by the mean values of the corresponding C_1 and C_2 distributions (Table 5.3). The geometry of the system was set up to reproduce the experimental conditions as closely as possible: the indenter radius corresponded to the effectively used one (R=22.3 µm), and the spheres dimensions were taken as the radius averages of all MCF10A acini used during AFM indentation experiments (presented in Figure 5.31).

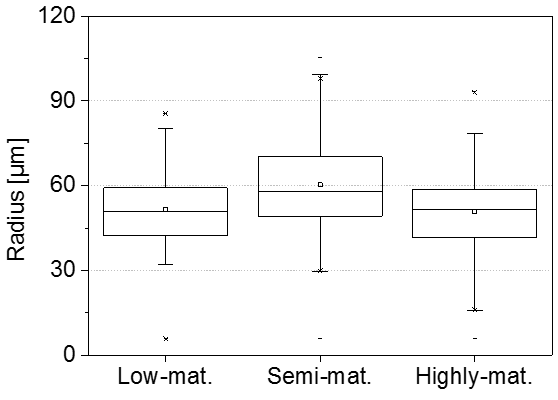

Figure 5.31: Radii distribution of MCF10A acini used during indentation experiments divided by maturation grade. $N_{low\text{-}mat}$=106, $N_{semi\text{-}mat}$=256 and $N_{highly\text{-}mat}$=138.

In the first step of analysis, the multicellular aggregates were considered as a single

hyperelastic material. After creating the geometry and choosing a mesh, imposing the boundary conditions and loads (for details on the chosen parameters, see Section 3.6), we could simulate the force-indentation relation of a rigid, glass sphere pressing up to a depth of 5 µm onto a Mooney-Rivlin material roughly shaped like an MCF10A acinus. The results of the simulations are shown in Figure 5.32.

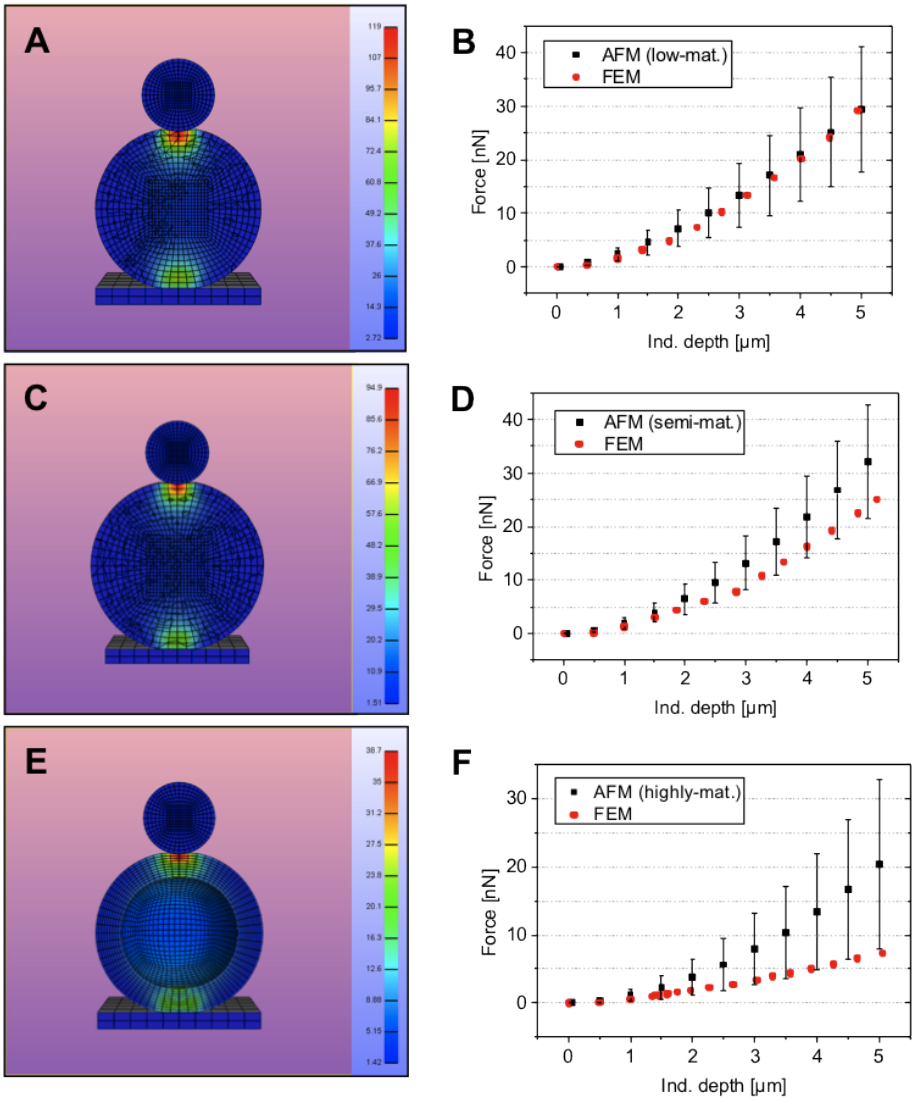

Figure 5.32.: FEM simulations of MCF10A acini of different maturation grades modeled as Mooney-Rivlin materials characterized by the parameters C_1 and C_2 obtained experimentally. **A.** Effective stresses distribution on a low-matured sphere indented by a rigid sphere up to a depth of 5 µm and (**B**) corresponding force-indentation curve as compared with experimental results. The same is depicted for mid-matured (**C**, **D**) and highly-matured (**E**, **F**) spheres.

In the plots, the simulated force-distance relationships are compared with the experimentally measured ones. In the case of spheres without a lumen, no major discrepancy between the two appears, indicating the validity of our approach: the 3D cell structures can, effectively, be described as hyperelastic materials characterized by the parameters obtained from AFM data fitting. In the case of the highly-matured group, though, the simulation does not capture the mechanical behavior of our cellular shells. This is most probably due to the poor definition of the luminar space; in reality, in fact, the lumen is a fluid-filled cavity whose internal pressure has an important role in determining the mechanical response of the shell. This fact was already indicated by the softening observed via AFM indentation experiments, despite the thickening and toughening of the BM. Due to the complexity of modeling solid-fluid interactions, though, in these preliminary simulations such effects were not accounted for, so that the lumen here was simply defined as a hollow space. A more detailed analysis in this direction will be an essential upcoming step.

As we anticipated in Section 2.4, finite element simulations are a precious tool for modeling situations that could not easily be described analytically. An interesting possibility lies therefore in the assessment of the impact of the BM on the mechanical response of whole MCF10A acini. Modeling now the cellular shell as a Mooney-Rivlin material surrounded by a thin elastic layer, we can once more mimic the scenario we observed through experiments. Of course this approach is not completely legitimated: the material constants C_1 and C_2 obtained from fitting derive from the response of *whole* acini, hence from the coupled response of single cells, cell-cell connections, lumen and basement membrane. Assigning now these material constants exclusively to the cellular component while at the same time adding a basement membrane to the system's geometry does not depict a very realistic scenario. This approach nonetheless allowed to qualitatively assess the effect of the BM on the stress distribution imposed on acini by indentation. The simulation result is given in Figure 5.33. Assigning a stiffness value of 5 kPa to the BM, almost no change is observed in the force-indentation curve (Fig. 5.33 C), but a major difference now appears in terms of stress distribution: unlike the previous case, the effective stress now mostly concentrates on the BM, leaving the underlying cells practically unaffected. This fact confirms the importance of the BM as a mechanical barrier performing a fundamental shielding function in breast glands.

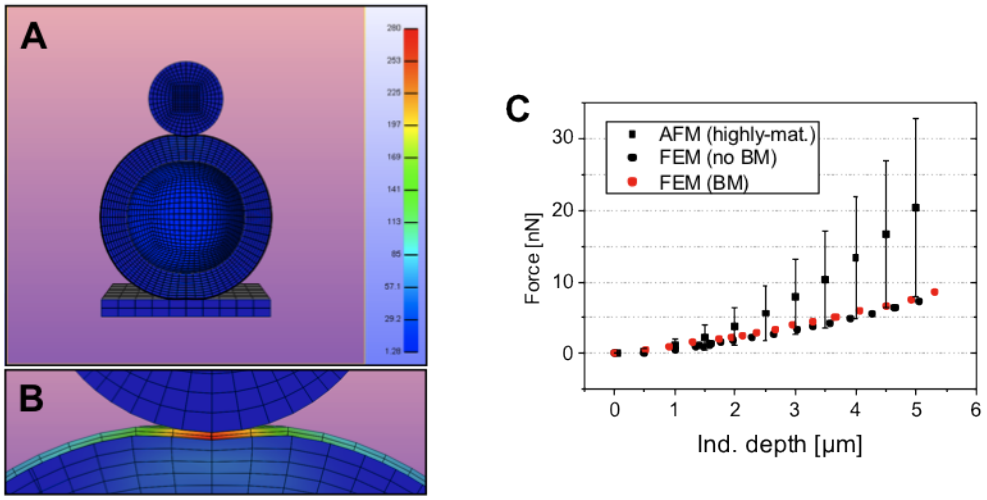

Figure 5.33.: FEM simulation of a hollow MCF10A acinus modeled as a Mooney-Rivlin material surrounded by an 800 nm thick basement membrane of elasticity E=5 kPa. The color scale indicates the effective stresses distribution.

5.8.1. Deformation at large indentations

After having analyzed a regime of small indentation, we were interested in assessing what happens to MCF10A acini subjected to large compressions. In order to observe the sphere's shape during indentation, we decided to work in a confocal microscope: obviously, this is not equipped to also serve as an AFM, hence the following custom-made set-up was implemented: calibrated AFM tips modified by the attachment of glass-beads were glued to glass microcapillaries about 10-15 cm in length, which were then moved by means of micromanipulators installed within the LSM set-up (for details on the procedure, see Section 3.4.7). This allowed to maneuver the cantilever with a precision sufficient to deeply indent into the spheres while imaging the latter by means of Z-stacks. A control over the force exerted during indentation was in this case very rough: only by taking Z-stacks of the whole cantilever in reflection mode before and after the indentations could we estimate the forces applied (assuming the spring constant k of the cantilever was known). The large errors affecting such measurements made the results obtained so far not conclusive; hence they are not reported here. Based on the available information, though, we estimated the application of forces in the range of the hundreds of nN; considering the indenter geometry, these corresponded to pressures around 150-450 Pa. A typical indentation sequence of an isolated MCF10A acinus is presented in Figure 5.34.

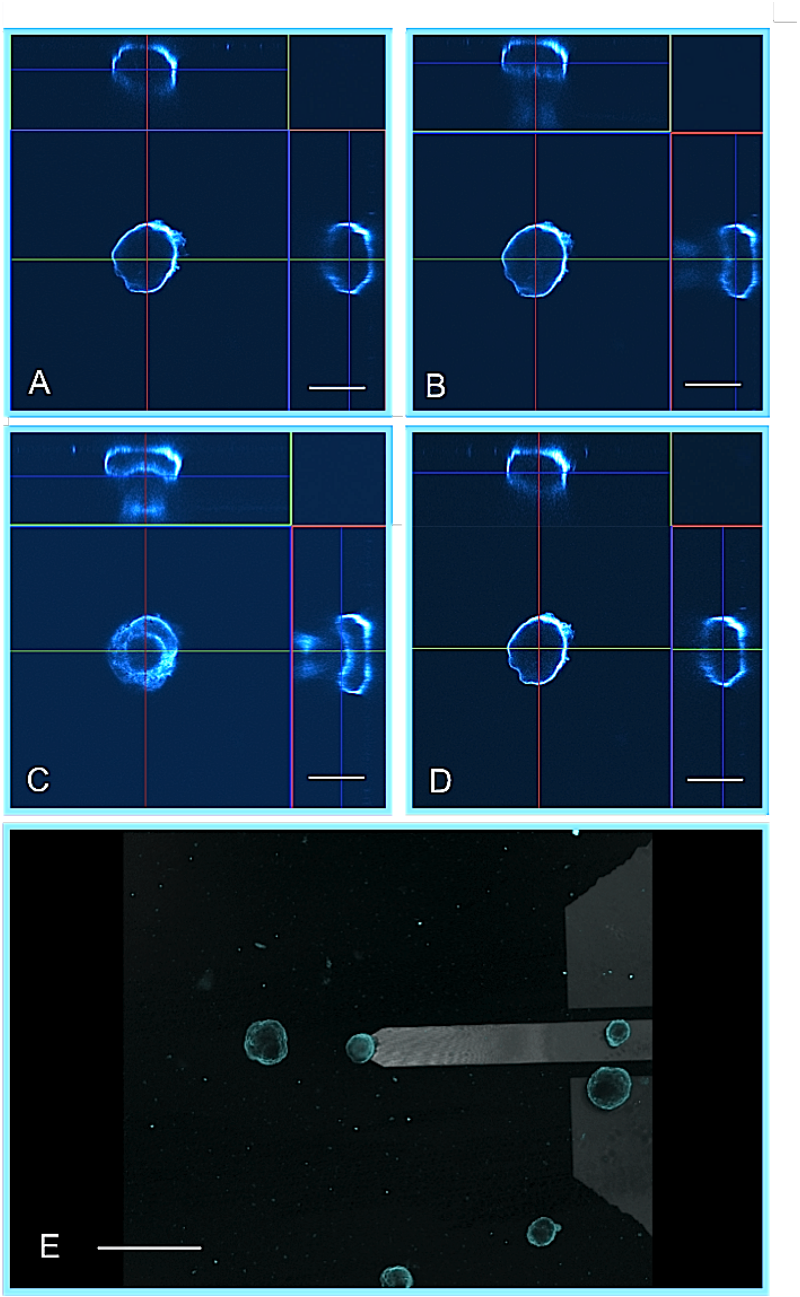

Figure 5.34.: 3D orthogonal projections of a highly-matured live MCF10A acinus before (**A**) during (**B**, **C**) and after (**D**) a large strain indentation performed by means of a glass spherical indenter attached to an AFM cantilever. In blue: collagen IV staining (basement membrane). Scale bars: 50 µm. **E.** 3D reconstruction of the AFM cantilever indenting on a sphere (bottom view). Scale bar: 200 µm.

Interestingly, even after very deep indentations, the acini manage to go back to a configuration that is very similar to the original one, implying a substantial elasticity at large deformations which is the hallmark of hyperelastic materials.
In such indentations the volume is not conserved (in Fig. 5.34 B for instance it is about 96% and in Fig. 5.34 C about 94% of the original one); this indicates that some fluid must leak outside the sphere during indentation, even though the system goes back to an equilibrium configuration shortly after the cessation of strain.
A higher resolution zoom-in on a single hollow sphere subject to a very large indentation can be seen in Figure 5.35: here, the single cells most probably undergo irreparable damage due to the excessive compression, and yet the basement membrane does not fracture and can withstand an expansive strain, on the equatorial plane, of about 140%.
Finally, in Figure 5.36 we present a FEM simulation of a hollow acinus subjected to a large indentation. Note the overall similarity to the structures displayed in Figure 5.35.
These experiments represent an interesting qualitative validation of the behavior of breast gland acini in a regime of large strain; single cells undergoing such pressures would simply break down: but their organization into spherical hollow units enclosed by a protein layer as resistant and elastic as the BM confers completely new mechanical properties to the system and a much higher level of resistance against external stress.

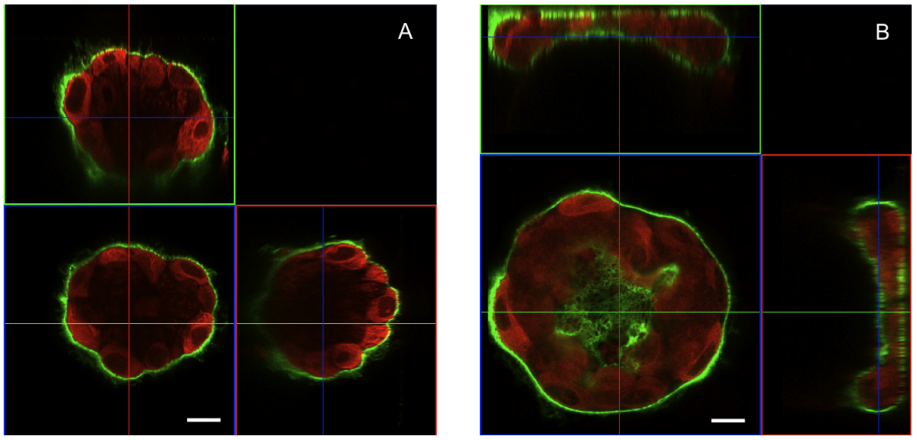

Figure 5.35.: 3D orthogonal projections of a highly-matured live MCF10A acinus before (**A**) and during (**B**) large strain indentation performed by means of a glass spherical indenter attached to an AFM cantilever. In red: CellTracker staining (cytoplasmic dye); in green: collagen IV staining (basement membrane). Central panels: equatorial focal planes (xy). Top panels: xz plane cuts. Right panels: yz plane cuts. Scale bars: 10 µm.

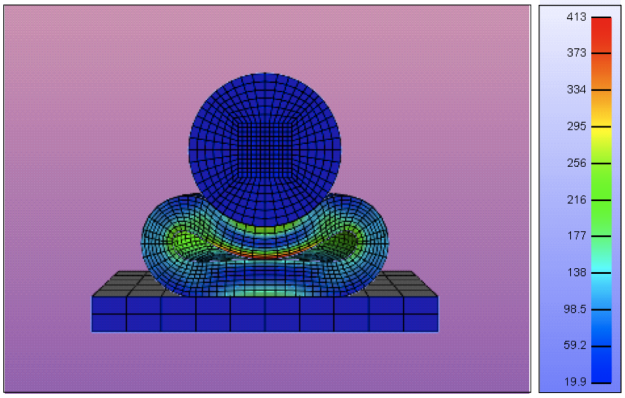

Figure 5.36: FEM simulation of a hollow MCF10A acinus modeled as a Mooney-Rivlin material subject to an indentation of 40 µm. The geometry of the system is very resemblant the one observed during AFM-like experiments at the LSM setup. The color scale indicates the effective stresses distribution.

5.9. Discussion of the results on 3D cell cultures

In this part of the work, the biomechanical properties of 3D breast gland acini have been analyzed. Despite the crucial centrality of this tissue for breast development and tumorogenesis, in fact, many of its qualities are still poorly understood. The main results obtained are summarized and discussed in the following.

5.9.1. The basement membrane regulates substrate permeation in breast acini

As we have seen, the role and function of BMs can be very wide and tissue-specific [31]. Here, given the possible implications for drug delivery, we were especially interested in understanding if the breast gland basement membrane acts as a permeation barrier; and if so, what is the size-threshold for macromolecules to penetrate.
To analyze the permeation properties, dextran tracers of different sizes were used as marker molecules and their diffusion through the BM and within the intracellular space of MCF10A acini was observed via fluorescence microscopy. By comparing the so-obtained profiles with the background signal we could observe potential molecule retardation effects. Due to the apoptotic material produced in the process of lumen formation, highly-matured spheres presented strong autofluorescence artifacts which would have affected our measurements; this group was therefore discarded from the analysis.
Despite the high flexibility of dextran polymer chains, which has at times been reported as a disadvantage during permeation experiments [66], the neutral character of these polysaccharides as well as the reproducible and precise character of their sieving through gels and membranes make them reliable and popular candidates for permeation studies [67].

The first prerequisite for an unbiased analysis of passive molecular transport into the intracellular space lies in the absence of tight-junctions (TJs): such cell-cell adhesion complexes would in fact make the acinar structures virtually impermeable [112], thereby completely altering the role of the BM for passive diffusion of ions and macromolecules. Thanks to the work of A. Gaiko-Shcherbak (ICS-7), the complete lack of functional TJ complexes from our MCF10A 3D cultures could be verified [54], in line with previous observations [111]. Next, spheres had to be isolated from the GelTrex bed in order to avoid the complication of having to account for the diffusion of dextran tracers in the EHS substrate during data analysis. A semi-empirical model was used to fit the time course of fluorescence intensity profiles recorded *within* the volume enclosed by the BM; as a result, time constants describing the variation of the diffusion speed with respect to the background ($\Delta\tau$) were obtained (Section 5.2). Data clearly indicated a functional relation between the acinar maturation grade and the selectivity of the permeation barrier; dextrans of all analyzed molecular weights (3, 10 and 40 kDa) could in fact penetrate without substantial retardation through the BMs of low-matured acini, but delays were observed in the semi-matured ones, especially significant for the 40 kDa molecules.
This implies a substantial alteration in the maturation level of the BM between the two age groups. Responsible for this effect are most intuitively a thickening of the membrane and (or) a decrease in pore size [110]; the first was observed by means of AFM imaging on isolated, flat BM layers (Section 5.4.1) and the second is implied by the progressively increasing of the $\Delta\tau$ values with increasing dextran molecular weight. From our experiments it was not possible, though, to elucidate which effect was the dominant one.
Unlabelled 40 kDa dextrans feature a hydrodynamic diameter of approximately 9 nm [109]: neglecting the slight variation caused by the presence of TexasRed dyes, we estimate that the breast gland BM pore size must be at least in the same order of magnitude. The average pore size of BMs can be very variable: in corneal epithelial BMs, for instance, it can reach up to over 110 nm [68]. Ultrahigh resolution scanning electron microscopy studies, on the other hand, have identified the pore sizes of different renal basement membranes as spanning from 10 nm (for the glomerular BM) to about 14 nm (for the Bowman's capsule BM) [108]. Interestingly, the glomerular BMs is well-known for its fundamental function as a compressible filter [37] and has a molecular permeability barrier in the range of 40 to 200 kDa [109]-[107]. These values are well in line with the ones derived from our experiments, validating the idea that, if pore size relates to organ function, the human breast gland BM indeed also acts as a filtration barrier.
In a physiological context, a good example of a small signaling molecule that needs to cross the BM in order to perform its function is the lactogenic hormone *prolactin*.

Prolactin stimulates breast cell differentiation and lactation [104] and, like many other hormones, it is directly secreted into the bloodstream by the hypophysis, from where it travels to the breast glands. In its biologically active form, it has a molecular weight of 23 kDa and an estimated diameter of about 8 nm [105]. This value is in very good agreement with our experimental result of 9 nm.
Moving from a physiological to a pathological scenario, when thinking about permeation in a context of drug design, an important point to touch is the so-called enhanced permeation and retention (EPR) effect: in general, tumor vasculature appears to be more permeable to macromolecules than normal vasculature, and shows reduced levels of lymphatic clearance [102]. That is why the recommended molecular cancer drug size is of at least 50 kDa: a good example is the polymer-conjugate variant of the classical chemotherapeutic drug paclitaxel known as paclitaxel poliglumex (PPX), a macromolecular complex about 45 times larger than the "naked" drug. A study on the delivery efficiency of PPX has reported 100-fold higher intratumoral drug concentrations, prolonged tumor exposure times and, in general, a higher efficiency and less side effects on healthy tissue than caused by paclitaxel [103].
These findings are in line with our data. The retardation effect observed for 40 kDa dextrans implies that, in a context of chemoterapeutic drug delivery, the BM would act as a gatekeeper protecting healthy tissue from adverse cytotoxic effects, while BM-lacking tumor cells would be targeted more effectively.

Interestingly, permeation experiments performed after enzymatic degradation of the collagen IV network (via collagenase IV treatment) revealed no size-dependent molecule retardation effect whatsoever. It seems therefore that collagen IV must play a fundamental role towards the creation of a meshwork capable of acting as a molecular sieve (Section 5.2.1).
It is well known that collagen chains composition can vary according to developmental stage [101] and physiological requirements [30]: for instance, collagen $\alpha 3 \alpha 4 \alpha 5$ chains are believed to be associated with increased macromolecule size-selectivity of kidney BMs [99]: comparable chains are located in mammary gland BMs [100], and might have a similar effect on molecule permeation. Superresolution microscopy imaging of the collagen IV network, though, displayed a mesh size in the order of the micrometer (Section 5.4.3): this clearly indicates that this protein alone is not enough for effectively providing a size-selective filter effect. The structure of this network, instead, indicated how it probably serves as a fundamental backbone within the BM to which other elements bind and crosslink in order to create a finer structure; therefore, in the future we shall

expand superresolution analyses to other ECM components as well.
A similar pattern was also observed via SEM imaging of isolated BMs. In this case it was unfortunately not possible to identify the molecular components of the membrane, and when assessing structure dimensions it must be kept in mind that SEM preparation has a shrinking effect on biological samples [165]. Nonetheless, a series of ring-like structures composed of larger fibers bundles with a mesh size in the micrometer range could be identified (Section 5.4.2); because of the resemblance of such structures to those observed via fluorescence microscopy, we hypothesized that this would be the collagen backbone. Within this larger structures, a much finer meshwork could be observed in the parts of the samples that were not damaged by the preparation procedure. Note that the BMs observed at the SEM had always been isolated from low-matured MCF10A spheres: it would therefore be interesting to also perform SEM investigations of highly-matured BMs. Given that AFM imaging of two different age groups pointed at a significant thickening of the membranes over time (Section 5.4.1), we can assume that SEM imaging of highly-matured BMs would reveal lower pore sizes and a generally denser structure.

5.9.2. The mechanical stability of breast acini strongly depends on the basement membrane

To proceed in our biomechanical characterization of MCF10A acini, at first we investigated the impact of the BM for the overall stability of breast glands. Simple decellularization experiments performed via detergent incubation allowed to disrupt all cellular structures while leaving the BMs unaffected. During OGP-incubation, spheres underwent a fast, osmotically-driven swelling and a subsequent, slow re-equilibration phase leading to a shrinking to their original size. Along with this process, cell debris detached from the BM shells, reflecting a thorough loss of hemidesmosomal cell-BM connections [111]; such contacts therefore seem not to be mandatory for BM stability.
At this point, comparative AFM indentation experiments were performed: the data collected in this phase were not analyzed according to any specific material model, but were just compared based on raw force-indentation curves: trying to model cellular debris enclosed by a thin protein layer as any kind of analytically characterizable material would have in fact not been possible.
Despite such limitations, the raw data still offered interesting insights: first, we observed that native MCF10A acini required up to 3-fold higher forces to be indented up to the same depth than cell-free BM shells. This very intuitive result just confirmed the impor-

tance of cytoskeletal components, of cell-cell connections (mostly adherence junctions) and of cell-BM adhesions (notably, hemidesmosomes and $\alpha 6\beta 4$ integrin receptor bonds [111]) to the mechanical stability of these highly organized cellular clusters.
But, more importantly, such experiments allowed to assess the fundamental elasticity of BM shells (Section 5.3). Indentation curves performed on decellularized acini, in fact, were systematically reproducible, and showed that even OGP-treated shells could withstand loads of up to 20 nN without loss of structural stability. Given the geometry of the AFM indenter used, this force corresponded to a compressive pressure of about 80 Pa. It is worth noting how this value lies in a physiologically relevant range: the interstitial fluid pressure in healthy breast gland tissue has in fact been reported to lie in the range of 40 to 53 Pa. Benign breast tumors and invasive ductal carcinomas instead exhibit ten- to hundredfold higher pressure values of 480 Pa to 3.9 kPa, respectively [98].
Even decellularized BM shells, therefore, are capable of withstanding loads that physiologically occur under normal conditions in vivo; a further indication of the relevance of MCF10A acini as a biophysical in vitro model for breast glands.
In order to test the resistance and deformation pattern of MCF10A acini under conditions of extreme load, AFM-like indentation experiments were performed at a confocal microscope setup (Section 5.8.1). Despite the impossibility, in this case, to precisely measure the applied force, images of the cantilever deflection allowed to at least roughly estimate it, provided that the spring constant k of the cantilever was known. In this case, pressures of about 150 to 450 Pa were applied on breast acini. These might be enough to irreversibly damage the inner cells, although we do not have evidence for it; but still did not prove sufficient to fracture the BM, which basically returned to its initial shape after cessation of indentation.
This test allowed to validate the fundamental role played by the BM in mechanically protecting breast glands and in offering the first and foremost barrier against the pressure built up during tumor development and progression.

5.9.3. Hyperelastic models successfully describe the mechanics of microtissues

In the next step of analysis, AFM indentation experiments were repeated on MCF10A acini of different developmental stages. Given the complex and inhomogeneous nature of such biological samples, it would have been unthinkable to simply rely on a Hertzian description to extract material properties from the AFM data. Although certain multi-

cellular structures behave in a linear elastic fashion (for example, murine sarcoma models [79] and *Xenopus laevis* embryonic tissue [80] as probed by micropipette aspiration), for our system this was not the case.
The application of hyperelastic models to the analysis of soft biological materials has proven very successful since its conceptual introduction, in 1967, by Y.C. Fung [159]. Both nanoindentation experiments performed on single cells or cartilage specimen [155] and tensile tests of various macroscopic tissues (such as skin or brain [87]) could already be interpreted in terms of the different semi-empirical laws derived from the simplification of constitutive equations for the case of uniaxial or equibiaxial tension [155].
Therefore, we decided to model MCF10A and MDA-MB-231 3D spheroids as hyperelastic materials, and worked in a regime of small indentations in order to remain well within the limit of incompressibility (i.e., no volume variation) required by the reformulations of such models in terms of force-distance curves. Fitting the indentation portion of AFM cycles to equations describing the uniaxial indentation of a rigid spherical indenter to a Fung, Ogden and the Mooney-Rivlin material, respectively, we could verify how, for indentations of up to about 1 µm, all three models performed similarly well (Section 5.7). Despite the huge spread of data, dictated by the unavoidable variance of size, morphology and basement membrane thickness among our samples, the stiffness parameters E_0 obtained from the fits always showed comparable values and distributions. At higher indentation depths, though, the Mooney-Rivlin fits started finding material parameters C_1 and C_2 whose sum was, at times, smaller than zero. Since this quantity physically represents a shear modulus, we would expect it to be positive; that is why a constraint on the fit parameters had to be imposed, even though this imposition had the effect of significantly lowering fit quality. The Fung and the Ogden model, on the other hand, showed excellent fitting of the experimental data up to depths of at least 3 µm. The dependency of material parameters upon indentation depth was analyzed, and in both case showed narrower distributions for higher fit ranges.

Generally, what these models do not grasp is the viscoelastic nature of the analyzed tissues: soft biological materials show strain rate dependence, and their mechanical properties are influenced by a discouragingly high number of factors. Studies of the tensile behavior of skin under different thermal loading conditions, for instance, have characterized the temperature-dependency of the mechanical properties of epidermal tissue, which correlate with dermal collagen denaturation [86].
As already noted by Fung, during stretching experiments soft tissue starts behaving in a reproducible way only after a few "preconditioning" cycles; observation which has led

to a re-formulation of the Mooney-Rivlin stress-strain relation in terms of a parameter accounting for skin prestretch [85]. On the single cell level, even factors such as growth medium composition [115] and surface coating [113] can affect cellular stiffness.
These are just a few examples of the difficulties faced when trying to describe complex biological tissues in terms of quantitative biomechanical properties. Despite such limitations, though, modeling breast gland microtissue as a hyperelastic material proved to be an approximation sufficient, for the time being, to our scope. This analysis approach, in fact, gave clear indications about the biomechanical differences arising at different maturation stages of MCF10A acini; a result that would have not been achievable by using traditional linearly elastic models.

5.9.4. Breast gland stiffness changes according to the maturation grade

AFM indentation experiments performed on MCF10A acini of different maturation grades showed how low- and semi-matured acini did not display significant differences in their mechanical response: despite the thickening of the basement membrane that accompanies this maturation, in fact, force-indentation curves distributions somewhat surprisingly showed an almost perfect overlap (Section 5.5.1). This fact might simply indicate that the differences introduced by partial BM development to the overall mechanical stability of spheroids are too fine to be detected with this kind of experiment.
It would be interesting to perform force spectroscopy cycles using stiffer cantilevers and reaching deeper indentation depths; or to assess the mechanical properties on a local rather than on a global scale, by using for instance pointy tips that would therefore mostly probe the BM layer adhering on the cellular spheroids. In this case we could perhaps observe variations induced by the membrane's thickening; examples of the substantial differences in material response obtained from indentations at different levels of tissue organization (i.e. at the micrometric vs. at the nanometric scale) have already been reported for the case of articular cartilage [83] and osteoartritic tissue [84].
When probing highly-matured MCF10A acini, though, we observed a statistically significant softening with respect to younger spheres, despite all other indications pointing at the thickening and stiffening of the BM scaffold during maturation. The formation of a luminar space in the final stage of breast gland's development is in this case responsible for the observed difference; the fluid enclosed in the hollow lumen obviously plays a significant role in determining tissue homeostasis, as was also confirmed by the failure of FEM simulations to reproduce the experimental results in absence of a proper modeling of the liquid present in the lumen.

A study reporting AFM creep tests performed on MCF10AT premalignant spheroids (a c-Ha-*ras* oncogene-transfected variant of MCF10A cells which are incapable of forming lumina [81]) and comparing them to MCF10A lumen-harboring acini revealed differences of about 60% in their stiffness [58]. By analyzing the relative contributions of single cells, cell-cell junctions and lumen formation to the viscoelastic response of MCF10AT spheroids, the authors concluded that lumen filling alone could explain the observed differences in stiffness. Although in this case different cell lines were used, our results are principally in line with such data, both qualitatively and quantitatively: when comparing the median values of the initial Young's moduli E_0 distributions between semi- and highly-matured MCF10A acini, in fact, we obtained variations spanning from about 50% to about 60% according to indentation depth analyzed and fit model used. As already mentioned, lumen filling caused by unregulated cellular proliferation is typical of the arising of pathologic conditions such as of carcinoma *in situ*: the consequent disruption of organized epithelial structures can occur in response to genetic mutations [82], but also increased ECM stiffness [48]. Mechanical compression in fact drives cancer cells towards a more invasive and motile phenotype [97].
Analysis of MDA-MB-231 agglomerates, 3D microtissues derived from a highly invasive, mesenchymal-like cell line, revealed how these are even softer than the hollow MCF10A acini. This fact was previously known for single cells [116], but had never been tested on a multicellular level. A growing body of evidence suggests that tumor progression can have diverging effects on cellular elasticity [65]: in some cases, cancer cells stiffen when compared with benign cells, and no clear trend in rigidity can be identified when comparing cells of different metastatic potential from different organs [78]. MDA-MB-231 cells are known for their high motility and invasive potential: time-lapse studies of 3D co-cultures of MCF10A and MDA-MB-231 cells even revealed how the latter can move collectively while retaining their group structure [77]. Our data therefore confirm a coupling between the mechanical and dynamical properties of these cells.

In essence, the presented results offer the first attempt to characterize the mechanical properties of 3D epithelial model systems both from a global perspective and by isolating the contributions of their essential building blocks. Combined characterization of in vitro reconstructed basement membranes by means of AFM, SEM and fluorescence microscopy allowed to estimate the BM's thickness, pore dimension and size-selectivity retardation threshold for the different stages of acinar maturation, which ultimately mimic the various developmental phases that breast glands undergo in vivo. The BM was shown to offer significant structural support to breast gland acini, whose biomechan-

ical phenotype is vitally linked to the development and progression of breast tumors. Hopefully, this work will serve as a preliminary step towards a deeper understanding of the mechanical interplay between cells and their microenvironment, essential for opening new perspectives in cancer research.

6. General conclusion and outlook

In conclusion, in this work the biomechanical properties of cellular systems at different levels of organization were analyzed. At first, epidermal keratinocytes were compared to a mutant cell line lacking all intermediate filaments: AFM-based indentation experiments allowed to assess the impact of this complex cytoskeletal component on the overall mechanical stability of single cells as well as on cellular clusters. Despite some issues arising in the analysis of AFM indentation data according to the traditionally employed Hertz model (which assumes linear elasticity of samples), experimental evidence indicated a softening of about 25%-35% in single knock-out cells, which increased to almost 50% for the case of cellular monolayers. This fact is due to the increased stiffness of keratinocytes interconnected by desmosomes; such cell-cell adhesions, by directly binding intermediate filaments together, produce a coupling effect able to strengthen the whole cellular cluster and increase its stability. All data analysis approaches employed (simple Hertz fitting, application of a power law with best-fitting exponent and comparison of raw force-indentation curves) pointed at the same results. This softening effect could only be partially reversed by re-expression of single keratin genes, implicating the importance of keratins other than the classic dimerization partners K5/K14 to the building of a fully functional network. The data presented therefore make a very strong case for the crucial contribution of keratin filaments to cellular mechanics.

An interesting question is whether these two-dimensional results are directly transferable to a three-dimensional scenario. In this case, in fact, next to the cytoskeletal components also cell-ECM and cell-BM connections would need to be taken into account. An idea of the situation for different kinds of microtissues is given in Figure 6.1.
The first protocol for the 3D culture of epidermal cells was published only relatively recently [59]: the successful establishment of ex-vivo skin-like tissue relies on a rather articulated co-culture of neonatal keratinocytes and dermal fibroblasts embedded in a collagen matrix. Cells need to be grown at the air-liquid interface and a differentiation process has to be induced before artificial skin can be identified.

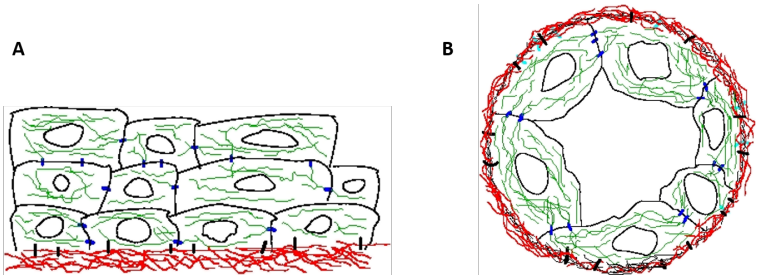

Figure 6.1.: Schematic representation of the various elements contributing to tissue mechanics in (**A**) epithelial and (**B**) breast gland microtissue. In green: cytoskeletal components; in blue: cell-cell adhesions; in red: basement membrane and ECM and in black: cell-ECM connections. Image courtesy of Dr. J.H. Yi (ICS-7).

The relative complexity of this microtissue, which displays a large interplay of biological parameters, make it unsuited for a direct bottom-up analysis. In our case, therefore, we focussed on a different model system and analyzed 3D epithelial cellular spheroids which mimic the lactating unit of breast glands. As can be appreciated from Figure 6.1 B, such lobular units provide a unique possibility of exploring different levels of biological organization: single cells carrying their very distinctive cytoskeletal polymers are connected into a complex architecture that exploits cell-cell and cell-BM contacts as a sort of "intercellular anchors" holding the various parts together. Most importantly, one of the main points of interest in deciphering the biomechanical properties of these structures lies in the fact that breast cancer initiation and progression depend not only on genetic mutations, but also on the disruption of tissue architecture.

In this work, we aimed at characterizing the overall mechanical behavior of MCF10A spheroids while at the same time isolating the contribution of the basement membrane as a fundamental structural element of the system. The permeation study here reported, supported by experiments characterizing the morphological and material properties of BMs, demonstrated a functional relation between the acinar maturation degree and the selectivity of size-dependent molecule retardation. Most probably, BM thickening is modulated by a variation in collagen composition and organization, although this hypothesis still needs to be verified. At the same time, data suggests the centrality of breast gland basement membranes as a mechanical scaffold shielding the inner cellular architecture from mechanical stress; besides offering the first quantification of the compressive force resistance properties of differentially developed acini, AFM indentation experiments allowed to verify the substantial elasticity of decellularized BM shells. Measurements of the nanoscale Young's modulus of isolated basement membranes re-

ported values spanning 3-390 kPa according to the maturation grade. Furthermore, a combination of AFM indentation and LSM confocal microscopy experiments showed how pressures well above the physiological range can be easily sustained by fully developed MCF10A acini, and how even very large deformations can be reversible and do not necessarily compromise the stability of the overall structures.
In the future, a challenge will certainly lie in the expansion and refining of the FEM simulations with the aim of achieving better modeling of our multicellular systems: this will include the need to describe the interactions with the fluid filling the cavity and surrounding the spheroids, and to incorporate the basement membrane scaffold into the system's geometry. Yet the difficulties deriving from such an ambitious goal should not be underestimated: to paint a realistic picture, one would have to take into account the fact that MCF10A spheroids are surrounded by a semi-permeable membrane which acts as a passive molecular diffusion filter. Defining the Stokes-Navier equations for such a system would not be possible without precise knowledge over the individual permeation coefficients of all macromolecules present in solution, and at least an idea about their size distribution. Given that we cannot easily access such information experimentally, the task would be non trivial.

On the up side, the possibility that such a model system offers to directly analyze the physico-chemical properties of basement membranes is just one of its many attractive features. Isolating single subcellular components and analyzing them in absence of the multitude of interactions present in vivo has allowed to identify fundamental features of individual cellular elements for decades: a good example, in this regard, are the aforementioned cytoskeletal in vitro reconstructed polymer networks [60]. This approach has proven harder for basal lamina and basement membranes, despite their fundamental function in building epithelial architecture, because very few biomimetic systems reproducing them exist so far. A body of research on loose ECM collagen networks is already present [61]-[62], but basement membranes typically need to be isolated from native tissue in order to be characterized.
Since the establishment of 3D cellular cultures, though, a major gap was bridged; in vitro reconstructed systems that directly secrete BMs allowed for a better understanding of the interplay between molecular signals and cellular environment. It is of course wishful that we proceed along this road: thoroughly analyzing collagen and laminin composition during acinar development, for example, would make us better understand the modulation of permeation properties observed in experiments.
It is well known that matrix metalloproteinases (MMPs) play a crucial role of in dy-

namically remodeling breast gland's ECM meshwork and BM structure [40]: increased ECM stiffness, for instance, induces the expression of MMP14 in MCF10A breast acini, which in turn leads to altered BM structures [63]. Resolving the interplay between membrane thickening and the putative MMP remodeling function would be a point of extreme interest and could open new insights in the molecular regulation of basement membrane's formation. Along these lines, it would be engaging to assess the impact of external forces on the development and maturation of cellular acini; when subject to periodic stress, would MCF10A cells develop some kind of adaptation mechanism? Or would the mechanosensing cascade induce an altered morphogenic response?
Microfluidic studies exposing 3D ovarian cancer nodules to a continuous laminar flow showed that fluidic forces act as modulators of many morphological and genetic cellular features, to the point of inducing epithelial-mesenchymal transitions in the OVCAR5 cell line [64]. Periodic stretching would perhaps represent a more physiologically relevant scenario in case of MCF10A cells, although the exposure of mammary microtissue to fluid-induced pressure, as we have seen, is an important feature of mechanical homeostasis.

Taken together, the possibilities of future research directions are manifold. While thinking about them, we can only stress what a precious platform 2D and especially 3D in vitro model systems offer towards a better understanding of biological structures and their properties. Living systems embody a complexity that can hardly be grasped without deconstructing it into its fundamental components: hopefully, this work offers a chance to appreciate how important at least one of such components, namely intra- and extra-cellular polymer networks, are to the mechanical properties of tissue.

Bibliography

[1] J.e. Hesketh and I.F. Pryme, editors. *The cytoskeleton: role in cell physiology.* Elsevier, 1996.

[2] B. Alberts, A. Johnson, J. Lewis, M. Raff, K. Roberts, and P. Walter. *Molecular Biology of the Cell.* Garland Science, 2014.

[3] F. Rosso, A. Giordano, M. Barbarisi, and A. Barbarisi. From cell-ECM interactions to tissue engineering. *Journal of Cellular Physiology*, 199(2):174–180, 2004.

[4] A. Szent-Györgyi. Free energy relations and contraction of actomyosin. *The Biological Bullettin*, 96:140–161, 1949.

[5] http://www.biozentrum.unibas.ch/typo3temp/pics.

[6] J.e. Hesketh and I.F. Pryme, editors. *The cytoskeleton: structure and assembly.* Elsevier, 1995.

[7] E. Mandelkow and E.M. Mandelkow. Microtubule structure. *Current opinion in structural biology*, 4:171–179, 1994.

[8] T. Mitchison and M. Kirschner. Dynamic instability of microtubule growth. *Nature*, 312(15):237–242, 1984.

[9] S. Kim and P. Coulombe. Intermediate filament scaffolds fulfill mechanical, organizational, and signaling functions in the cytoplasm. *Genes development*, 21(13):1581–97, 2007.

[10] J.E. Eriksson, T. Dechat, B. Grin, B. Helfand, M. Mendez, H. Pallari, and R.D. Goldman. Introducing intermediate filaments: from discovery to disease. *Journal of clinical investigation*, 119:1763–1771, 2009.

[11] E. Fuchs. Intermediate filaments: structure, dynamics, function and disease. *Annual Review of Biochemistry*, 63:345–382, 1994.

[12] J. Schweizer, P.E. Bowden, P.A. Coulombe, L. Langbein, E.B. Lane, T.M. Magin, L. Maltais, M.B. Omary, D.A. Parry, M.A. Rogers, and M.W. Wright. New consensus nomenclature for mammalian keratins. *Journal of Cell Biology*, 174(2):169–174, 2006.

[13] J. Kanitakis. Anatomy, histology and immunohistochemistry of normal human skin. *European Journal of Dermatology*, 12(4):390–399, 2002.

[14] E. Proksch, J. Brandner, and J.M. Jensen. The skin: an indispensable barrier. *Experimental Dermatology*, 17(12):1063–1072, 2008.

[15] C.M. Chuong, B.J. Nickoloff, P.M. Elias, L.A. Goldsmith, E. Macher, P.A. Maderson, J.P. Sundberg, H. Tagami, P.M. Plonka, K. Thestrup-Pederson, B.A. Bernard, J.M. Schröder, P. Dotto, C.M. Chang, M.L. Williams, K.R. Feingold, L.E. King, A.M. Kligman, J.L. Rees, and E. Christophers. What is the 'true' function of skin? *Experimental Dermatology*, pages 159–187, 2002.

[16] http://www.nku.edu/ dempseyd/SKIN.htm.

[17] D. Garrod and M. Chidgey. Desmosome structure, composition and function. *Biochimica et Biophysica Acta - Biomembranes*, 1778(3):572–587, 2008.

[18] P.D. Kouklis, E. Hutton, and E. Fuchs. Making a connection: direct binding between keratin intermediate filaments and desmosomal proteins. *Journal of Cell Biology*, 127(4):1049–1060, 1994.

[19] A. Al-Amoudi, L.P. Norlen, and J. Dubochet. Cryo-electron microscopy of vitreous sections of native biological cells and tissues. *Journal of Structural Biology*, 148:131–135, 2004.

[20] M.F. Jonkman, A.M. Pasmooij, S.G. Pasmans, M.P. van den Berg, H.J. Ter Horst, A. Timmer, and H.H. Pas. Loss of desmoplakin tail causes lethal acantholytic epidermolysis bullosa. *The American Journal of Human Genetics*, 77:653–660, 2005.

[21] L. Kreplak, H. Bär, J.F. Leterrier, H. Herrmann, and U. Aebi. Exploring the mechanical behavior of single intermediate filaments. *Journal of molecular biology*, 354(3):569–577, 2005.

[22] D. Fudge, D. Russell, D. Beriault, W. Moore, E.B. Lane, and A.W. Vogl. The intermediate filament network in cultured human keratinocytes is remarkably extensible and resilient. *PLoS ONE*, 3(6), 2008.

[23] R. Windoffer, M. Beil, T.M. Magin, and R.E. Leube. Cytoskeleton in motion: the dynamics of keratin intermediate filaments in epithelia. *JBC*, 194(5), 2011.

[24] P.A. Coulombe and E. Fuchs. Epidermolysis bullosa simplex. *Seminars in Dermatology*, 12(3):173–190, 1993.

[25] P. Vijayaraj, C. Kröger, U. Reuter, R. Windoffer, R.E. Leube, and T.M. Magin. Keratins regulate protein biosynthesis through localization of glut1 and -3 upstream of amp kinase and raptor. *Journal of Cell Biology*, 187(2):175–184, 2009.

[26] C. Kröger, F. Loschke, N. Schwarz, R. Windoffer, R.E. Leube, and T.M. Magin. Keratins control intercellular adhesion involving PKC-α-mediated desmoplakin phosphorylation. *Journal of Cell Biology*, 201(5):681–92, 2013.

[27] K. Seltmann, W. Roth, C. Kröger, F. Loschke, M. Lederer, S. Hüttelmaier, and T.M. Magin. Keratins mediate localization of hemidesmosomes and repress cell motility. *The Journal of Investigative Dermatology*, 1(10), 2012.

[28] F. Hassiotou and D. Geddes. Anatomy of the human mammary gland: current status of knowledge. *Clinical Anatomy*, 26(1):29–48, 2013.

[29] D.T. Geddes. Inside the lactating breast: the latest anatomy research. *Journal of Midwifery and Women's Health*, 52(6):556–63, 2007.

[30] V.S. Le Bleu, B. Macdonald, and R. Kalluri. Structure and function of basement membranes. *Experimental Biology and Medicine*, 232:1121–1129, 2007.

[31] E. Engvall. Structure and function of basement membranes. *International Journal of Developmental Biology*, 39:781–787, 1995.

[32] P.D. Yurchenco, Y.S. Cheng, and H. Colognato. Laminin forms an independent network in basement membranes. *Journal of Cell Biology*, 117:1119–1133, 1992.

[33] J. Candiello, G.J. Cole, and W. Halfter. Age-dependent changes in the structure, composition and biophysical properties of a human breast membrane. *Matrix Biology*, 29:402–410, 2010.

[34] W. Halfter, C. Monnier, D. Müller, P. Oertle, G.Uechi, M. Balasubramani, F. Safi, R. Lim, M. Loparic, and P.B. Henrich. The bi-functional organization of human basement membranes. *PLoS ONE*, 8(7), 2013.

[35] H. Tanjore and R. Kalluri. The role of type IV collagen and basement membranes in cancer progression and metastasis. *The American Journal of Pathology*, 168(3):715–717, 2006.

[36] J.P. Caulfield and M.G. Farquhar. The permeability of glomerular capillaries to graded dextrans: identification of the basement membrane as the primary filtration barrier. *Journal of Cell Biology*, 63(3):883–903, 1974.

[37] G.B. Robinson and H.A. Walton. Glomerular basement membrane as a compressible ultrafilter. *Microvascular Research*, 38:36–48, 1989.

[38] L. Ozzello. Ultrastructure of the human mammary gland. *Pathology Annual*, 6:1–59, 1971.

[39] J. Muschler and C.H. Streuli. Cell-matrix interactions in mammary gland development and breast cancer. *CHS Perspectives in Biology*, 2(10), 2015.

[40] R. Kalluri. Basement membranes: structure, assembly and role in tumour angiogenesis. *Nature Reviews Cancer*, 3(6):422–433, 2003.

[41] J. Harris, M. Lippman, M. Morrow, and C. Osborne. *Diseases of the Breast*. Lippincott, Williams Wilkins, 1999.

[42] D. Hanahan and R. Weinberg. The hallmarks of cancer. *Cell*, 100(57-70), 2000.

[43] F.T. Bosniana, M. Havenitha, and J.P.M. Cleutjensa. Basement membranes in cancer. *Ultrastructural Pathology*, 8(4):291–304, 1985.

[44] L.A. Liotta. Tumor invasion and metastases: Role of the basement membrane. *American Journal of Physiology*, 11(3):339–348, 1984.

[45] M.J. Slade, R.C. Coope, J.J. Gomm, and R.C. Coombes. The human mammary gland basement membrane is integral to the polarity of luminal epithelial cells. *Experimental Cell Research*, 247(1):267–278, 1999.

[46] D.T. Butcher, T. Alliston, and V.M. Weaver. A tense situation: forcing tumour progression. *Nature Reviews Cancer*, 9:108–122, 2009.

[47] P.A. Netti, D.A. Berk, M.A. Swartz, A.J. Grodzinsky, and R.K. Jain. Role of extracellular matrix assembly in interstitial transport in solid tumors. *Cancer Research*, 60:2497–2503, 2000.

[48] M.J. Paszek N. Zahir, K.R. Johnson, J.N. Lakins, G.I. Rozenberg, A. Gefen, C.A. Reinhart-King, S.S. Margulies, M. Dembo, D. Boettiger, D.A. Hammer, and V.M. Weaver. Tensional homeostasis and the malignant phenotype. *Cancer Cell*, (2005):241–254, 8.

[49] F. Pampaloni, E.G. Reynaud, and E.H. Stelzer. The third dimension bridges the gap between cell culture and live tissue. *Nature Reviews Molecular Cell Biology*, 8:839–845, 2007.

[50] C.A. Vacanti. The history of tissue engineering. *Journal of Cellular and Molecular Medicine*, 10(3):569–576, 2006.

[51] A.J. Engler, S. Sen, H.L. Sweeney, and D.E. Discher. Matrix elasticity directs stem cell lineage specification. *Cell*, 126(4):677–689, 2006.

[52] J. Debnath, S.K. Muthuswamy, and J.S. Brugge. Morphogenesis and oncogenesis of MCF-10A mammary epithelial acini grown in three-dimensional basement membrane cultures. *Methods*, 30(3):256–68, 2003.

[53] C. Hebner, V.M. Weaver, and J.Debnath. Modeling morphogenesis and oncogenesis in three-dimensional breast epithelial cultures. *Annual Review of Pathology: Mechanisms of Disease*, 3:313–339, 2008.

[54] A. Gaiko-Shckerbak, G. Fabris, G. Dreissen, R. Merkel, B. Hoffmann, and E. Noetzel. The acinar cage: basement membranes deterine molecular exchange and mechanical stability of human breast acini. *PLoS ONE*, 10(12), 2015.

[55] P.A. Kenny, G.Y. Lee, C.A. Myers, R.M. Neve, J.R. Semeiks, P.T. Spellman, K. Lorenz, M.H. Barcellos-Hoff, O.W. Petersen, J.W. Gray, and M.J. Bissell. The morphologies of breast cancer cell lines in three-dimensional assays correlate with their profiles of gene expression. *Molecular Oncology*, 1(1):84–96, 2007.

[56] E. Candi, R. Schmidt, and G. Melino. The cornified envelope: a model of cell death in the skin. *Nature Reviews Molecular Cell Biology*, 6:328–340, 2005.

[57] R.H. Gavin, editor. *Cytoskeleton Methods and Protocols*. Springer Protocols, 2010.

[58] G. Venugopalan, D.B. Camarillo, K.D. Webster, C.D. Reber, J.A. Sethian, V.M. Weaver, D.A. Fletcher, H. El-Samad, and C.H. Rycroft. Multicellular architecture of malignant breast epithelia influences mechanics. *PLoS ONE*, 9(8), 2014.

[59] P. Gangatirkar, S. Paquet-Fifield, A. Li, R. Rossi, and P. Kaur. Establishment of 3D organotypic cultures using human neonatal epidermal cells. *Nature Protocols*, 2(1):178–186, 2007.

[60] L. Ma, J. Xu, P.A. Coulombe, and D. Wirtz. Keratin filament suspensions show unique micromechanical properties. *Journal of Biological Chemistry*, 274:19145–19151, 1999.

[61] S. Rhee and F. Grinnell. Fibroblast mechanics in 3D collagen matrices. *Advanced drug delivery reviews*, 59(13):1299–1305, 2007.

[62] C. Mierke, P. Kollmannsberger, D.P. Zitterbart, G. Diez, T.M. Koch, S. Marg, W.H. Ziegler, W.H. Goldmann, and B. Fabry. Vinculin facilitates cell invasion into 3D collagen matrices. *Journal of Biological Chemistry*, 285(13121-13130), 2010.

[63] A. Lance, C.C. Yang, M. Swamydas, D. Dean, S. Deitch, K.J. Burg, and D. Dreau. Increased extracellular matrix density decreases MCF10A breast cell acinus formation in 3D culture conditions. *Journal of Tissue Engineering and Regenerative Medicine*, 2013.

[64] I. Rizvi, U.A. Gurkan, S. Tasoglu, N. Alagic, J.P. Celli, L.B. Mensah, Z. Mai, U. Demirci, and T. Hasan. Flow induces epithelial-mesenchymal transition, cellular heterogeneity and biomarker modulation in 3D ovarian cancer nodules. *Proceedings of the National Academy of Sciences*, 110(22):1974–1983, 2013.

[65] M.J. Rosenbluth, W.A. Lam, and D.A. Fletcher. Force microscopy of nonadherent cells: a comparison of leukemia cell deformability. *Biophysical Journal*, 90(8):2994–3003, 2006.

[66] J.C. Williams, L.A. Mark, and S. Eichholtz. Partition and permeation of dextran in polyacrylamide gel. *Biophysical Journal*, 75(1):492–502, 1998.

[67] Y. Olsson, E. Svensjö, K.E. Arfors, and D. Hultström. Fluorescein labelled dextrans as tracers for vascular permeability studies in the nervous system. *Acta Neuropathologica*, 33(1):45–50, 1975.

[68] G.A. Abrams, S.L. Goodman, P.F. Nealey, M. Franco, and C.J. Murphy. Nanoscale topography of the basement membrane underlying the corneal epithelium of the rhesus macaque. *Cell and Tissue Research*, 299:39–46, 2000.

[69] J. Pawley. *Handbook of Biological Confocal Microscopy*. Springer, 2006.

[70] G. Benedek and F. Villars. *Physics with illustrative examples from medicine and biology: statistical physics*. Springer, Second Edition.

[71] Summary notes: force spectroscopy measurements and processing. Technical report, JPK Instruments, 2009.

[72] K. Weisshart. The basic principle of airyscanning. Technical report, Zeiss, 2014.

[73] N. Hersch, B. Wolters, G. Dreissen, R. Springer, N. Kirchgeßner, R. Merkel, and B. Hoffmann. The constant beat: cardiomyocytes adapt their forces by equal contraction upon environmental stiffening. *Biology Open*, 2:351–361, 2013.

[74] G. Forgacs. On the possible role of cytoskeletal filamentous networks in intracellular signaling: an approach based on percolation. *Journal of Cell Science*, 108:2131–2143, 1995.

[75] D.E. Ingber. Cellular tensegrity: defining new rules of biological design that govern the cytoskeleton. *Journal of Clinical Ultrasound*, 21(613-627), 1993.

[76] M. Lacroix and G. Leclercq. Relevance of breast cancer cell lines as models for breast tumors: an update. *Breast Cancer Research and Treatment*, 83:249–289, 2004.

[77] L.P. Ivers, B. Cummings, F. Owolabi, K. Welzel, R. Klinger, S. Saitoh, D. O'Connor, Y. Fujita, D. Scholz, and N. Itasaki. Dynamic and infuential interaction of cancer cells with normal epithelial cells in 3D culture. *Cancer Cell International*, 14(108), 2014.

[78] J Rother, H. Nöding, I. Mey, and A. Janshoff. Atomic force microscopy-based microrheology reveals significant differences in the viscoelastic response between malign and benign cell lines. *Open Biology*, 4(5), 2014.

[79] K. Guevorkiana, D. Gonzalez-Rodrigueza, C. Carlierb, S. Dufourb, and F. Brochard-Wyarta. Mechanosensitive shivering of model tissues under controlled aspiration. *Proceedings of the National Academy of Sciences*, 108(33):13387–13392, 2011.

[80] M. von Dassow, J.A. Strother, and L.A. Davidson. Surprisingly simple mechanical behavior of a complex embryonic tissue. *PLoS ONE*, 5(12), 2010.

[81] F.R. Miller H.D. Soule, L. Tait, R.J. Pauley, S.R. Wolman, P.J. Dawson, and G.H. Heppner. Xenograft model of progressive human proliferative breast disease. *Journal of the National Cancer Institute*, 85(21):1725–1732, 1993.

[82] P.J. Dawson, S.R. Wolman, L. Tait, G.H. Heppner, and F. R. Miller. MCF10AT: a model for the evolution of cancer from proliferative breast disease. *The American Journal of Pathology*, 148(1):313–319, 1996.

[83] M. Stolz, R. Raiteri andd A.U. Daniels, M.R. VanLandingham, W. Baschong, and U. Aebi. Dynamic elastic modulus of porcine articular cartilage determined at two different levels of tissue organization by indentation-type atomic force microscopy. *Biophysical Journal*, 86(5):3269–3283, 2004.

[84] M. Stolz, R. Gottardi, R. Raiteri, S. Miot, I. Martin, R. Imer, U. Staufer, A. Raducanu, M. Düggelin, W. Baschong, A.U. Daniels, N.F. Friederich, A. Aszodi, and U. Aebi. Early detection of aging cartilage and osteoarthritis in mice and patient samples using atomic force microscopy. *Nature Nanotechnology*, 4:186–192, 2009.

[85] S.N. Azizzati Mohd Noor and J. Mahmud. Skin prestretch evaluation adapting Mooney-Rivlin model. *Journal of Medical and Bioengineering*, 4(1):31–35, 2015.

[86] B. Zhou, F. Xu, C.Q. Chen, and T.J. Lu. Strain rate sensitivity of skin tissue under thermomechanical loading. *Philosophical Transactions of the Royal Society (A)*, 368(1912):679–690, 2010.

[87] B. R, M. Destrade, and M.D. Gilchrist. Hyperelastic and viscoelastic properties of brain tissue in tension. *Proceedings of the ASME 2012 International Mechanical Engineering Congress*, 2012.

[88] Y. Ruiguo, X. Ning, C. Kar, F. Man, W. King, C. Lai, K. Seiffert-Sinha, and A.A. Sinha. Analysis of keratinocytes stiffness after desmosome disruption using atomic force microscopy based nanomanipulation. *IEEE-NANO (9th IEEE Conference on Nanotechnology)*, pages 640–643, 2009.

[89] M. Homberg, L. Ramms, N. Schwarz, G. Dreissen, R.E Leube, R. Merkel, B. Hoffmann, and T.M. Magin. Distinct impact of two keratin mutations causing Epidermolysis Bullosa Simplex on keratinocyte adhesion and stiffness. *Journal of Investigative Dermatology*, 135(10):2437–2445, 2015.

[90] F.M. Hecht, J. Rheinlaender, N. Schierbaum, W.H. Goldmann, B. Fabry, and T.E. Schäffer. Imaging viscoelastic properties of live cells by AFM: power-law rheology on the nanoscale. *Soft Matter*, 11:4584–4591, 2015.

[91] N. Gavara and R.S. Chadwick. Determination of the elastic moduli of thin samples and adherent cells using conical atomic force microscope tips. *Nature Nanotechnology*, 7:733–736, 2012.

[92] E. Limpert, W.A. Stahel, and M. Abbt. Log-normal distributions across the sciences: keys and clues. *BioScience*, 51(5):341–352, 2001.

[93] R.W. Ogden. Large deformation isotropic elasticity – on the correlation of theory and experiment for incompressible rubberlike solids. *Proceedings of the Royal Society of London (A)*, 326(1567):565–584, 1972.

[94] H. Ibach. *Physics of surfaces and interfaces*. Springer, 2006.

[95] J.E. Lennard-Jones. On the determination of molecular fields. *Proceedings of the Royal Society of London (A)*, 106(738):463–477, 1924.

[96] W.R. Trickey, F.P. Baaijens, T.A. Laursen, L.G. Alexopoulos, and F. Guilak. Determination of the poisson's ratio of the cell: recovery properties of chondrocytes after release from complete micropipette aspiration. *Journal of Biomechanics*, 39(1):78–87, 2006.

[97] J.M. Tse, G. Cheng, J.A. Tyrrell, S.A. Wilcox-Adelman, Y. Boucher, R.K. Jain, and L.L. Munn. Mechanical compression drives cancer cells toward invasive phenotype. *Proceedings of the National Academy of Sciences*, 109(3):911–916, 2012.

[98] S.D. Nathanson and L. Nelson. Interstitial fluid pressure in breast cancer, benign breast conditions, and breast parenchyma. *Annals of Surgical Oncology*, 1:333–338, 1994.

[99] N. Ferrell, K.O. Cameron, J.J. Groszek, C.L. Hofmann, L. Li, R.A. Smith, A. Bian, A. Shintani, A.L. Zydney, and W.H. Fissell. Effects of pressure and electrical charge on macromolecular transport across bovine lens basement membrane. *Biophysical Journal*, 104:1476–1484, 2013.

[100] S. Nakano, K. Iyama, M. Ogawa, H. Yoshioka, Y. Sado, T. Oohashi, and Y. Ninomiya. Differential tissular expression and localization of type IV collagen alpha1(IV), alpha2(IV), alpha5(IV), and alpha6(IV) chains and their mRNA in nor-

mal breast and in benign and malignant breast tumors. *Laboratory Investigation*, 79:281–292, 1999.

[101] W. Halfter, J. Candiello, H. Hu, P. Zhang, E. Schreiber, and M. Balasubramani. Protein composition and biomechanical properties of in vivo-derived basement membranes. *Cell Adhesion and Migration*, 7:64–71, 2013.

[102] S.D. Chipman, F.B. Oldham, G. Pezzoni, and J.W. Singer. Biological and clinical characterization of paclitaxel poliglumex (PPX, CT-2103), a macromolecular polymer-drug conjugate. *International Journal of Nanomedicine*, 1:375–383, 2006.

[103] J.W. Singer. Paclitaxel poliglumex (XYOTAX, CT-2103): a macromolecular taxane. *Journal of Controlled Release*, 109(1-3):120–126, 2005.

[104] C. Bole-Feysot, V. Goffin, M. Edery, N. Binart, and P.A. Kelly. Prolactin (PRL) and its receptor: actions, signal transduction pathways and phenotypes observed in prl receptor knockout mice. *Endocrine Reviews*, 19:225–268, 1998.

[105] K.M. Ostrom. A review of the hormone prolactin during lactation. *Progress in Food and Nutrition Science*, 14:1–43, 1990.

[106] G.Y. Lee, P.A. Kenny, E.H. Lee, and M.J. Bissell. Three-dimensional culture models of normal and malignant breast epithelial cells. *Nature Methods*, 4(4):359–365, 2007.

[107] M.G. Farquhar. Editorial: The primary glomerular filtration barrier-basement membrane or epithelial slits? *Kidney international*, 8:197–211, 1975.

[108] K. Hironaka, H. Makino, Y. Yamasaki, and Z. Ota. Renal basement membranes by ultrahigh resolution scanning electron microscopy. *Kidney International*, 43:334–345, 1993.

[109] J.P. Caulfield and M.G. Farquhar. The permeability of glomerular capillaries to graded dextrans: identification of the basement membrane as the primary filtration barrier. *Journal of Cell Biology*, 63:883–903, 1974.

[110] S.H. Gehrke, J.P. Fisher, M. Palasis, and M.E. Lund. Factors determining hydrogel permeability. *Annals of the New York Academy of Sciences*, 831:179–207, 1997.

[111] J.M. Underwood, K.M. Imbalzano, V.M. Weaver, A.H. Fischer, A.N. Imbalzano, and J.A. Nickerson. The ultrastructure of MCF-10A acini. *Journal of Cellular Physiology*, 208:141–148, 2006.

[112] E.E. Schneeberger and R.D. Lynch. Structure, function, and regulation of cellular tight junctions. *American Journal of Physiology*, pages L647–661, 262.

[113] Y. Teng, J. Qui, Y. Zheng, X. Luo abd L. Zhang, L. Chen, and G. Wang. Effects of type I collagen and fibronectin on regulation of breast cancer cell biological and biomechanical characteristics. *Journal of Medical and Biological Engineering*, 34(1):62–68, 2012.

[114] J. Rother, H. Nöding, I. Mey, and A. Janshoff. Atomic force microscopy-based microrheology reveals significant differences in the viscoelastic response between malign and benign cell lines. *Open Biology*, 4, 2014.

[115] M. Nikkhah, J.S. Strobl, E.M. Schmelz, and M. Agah. Evaluation of the influence of growth medium composition on cell elasticity. *Journal of Biomechanics*, 44(4):762–766, 2011.

[116] E.A. Corbin, F. Kong, C.T. Lim, W.P. King, and R. Bashir. Biophysical properties of human breast cancer cells measured using silicon MEMS resonators and atomic force microscopy. *Lab on a Chip*, 15(3):839–847, 2015.

[117] E.M. Darling, S. Zauscher, J.A. Block, and F. Guilak. A thin-layer model for viscoelastic, stress-relaxation testing of cells using atomic force microscopy: do cell properties reflect metastatic potential? *Biophysical Journal*, 92(5):1784–1791, 2007.

[118] J.A. Santos, L.M. Rebêlo, A.C. Araujo, E.B. Barros, and J.S. de Sousa. Thickness-corrected model for nanoindentation of thin films with conical indenters. *Soft Matter*, 8:4441–4448, 2012.

[119] S. Maas, D. Rawlins, J. Weiss, and G. Ateshian. *FEBio: Finite Elements for Biomechanics. Theory Manual*. Musculoskeletal Research Laboratories, University of Utah, 2010.

[120] M. Zhang, Y. Cao, G. Li, and X. Feng. Spherical indentation method for determining the constitutive parameters of hyperelastic soft materials. *Biomechanics and Modeling in Mechanobiology*, 13:1–11, 2014.

[121] R.S. Rivlin. Large deformations of isotropic materials. IV. Further developments of the general theory. *Philosophical Transactions of the Royal Society (A)*, 241:379–397, 1948.

[122] M. Mooney. A theory of large elastic deformation. *Journal of Applied Physics*, 11:582–592, 1940.

[123] L.R. Treloar. *The physics of rubber elasticity.* Oxford University Press, 1975.

[124] J.D. Humprey. Continuum biomechanics of soft biological tissues. *Proceedings of the Royal Society of London (A)*, 459:3–46, 2003.

[125] E.D. Sifakis. FEM simulation of 3D deformable solids: a practitioner's guide to theory, discretization and model reduction. University of Wisconsin-Madison, 2012.

[126] R.B. Agarwal. An overview of the Finite Element Analysis. San José State University.

[127] J. Reddy. *An Introduction to the Finite Element Method.* Mc Graw-Hill, Third Edition.

[128] R. Courant. Variational methods for the solution of problems of equilibrium and vibrations. *Bulletin of the American Mathematical Society*, 49:1–23, 1943.

[129] A. Hrennikoff. Solution of problems of elasticity by the framework method. *Journal of Applied Mechanics*, 8(4):169–175, 1941.

[130] L.W. Welling, M.T. Zupka, and D.J. Welling. Mechanical properties of basement membrane. *News in Physiological Sciences*, 10:30–35, 1995.

[131] M.J. Bissell, P.A. Kenny, and D.C. Radisky. Microenvironmental regulators of tissue structure and function also regulate tumor induction and progression: the role of extracellular matrix and its degrading enzymes. *Cold Spring Harbor symposia on quantitative biology*, 70:343–356, 2005.

[132] M.J. Bissell and D. Radisky. Putting tumours in context. *Nature Reviews Cancer*, 1(1):46–54, 2001.

[133] M.J. Bissell, D.C. Radisky, A. Rizki, V.M. Weaver, and O.W. Petersen. The organizing principle: microenvironmental influences in the normal and malignant breast. *Differentiation; research in biological diversity*, 70(9-10):537–546, 2002.

[134] Q.S. Li, G.Y. Lee, C.N. Ong, and C.T. Lim. AFM indentation study of breast cancer cells. *Biochemical and Biophysical Research Communications*, 374(609-613), 2008.

[135] H.J. Butt, B. Cappella, and M. Kappl. Force measurements with the atomic force microscope: technique, interpretation and applications. *Surface Science Reports*, 59:1–152, 2005.

[136] V. Lulevich, H. Yang, R.R. Isseroff, and G. Liu. Single cell mechanics of keratinocyte cells. *Ultramicroscopy*, 110(12):1435–1442, 2010.

[137] T. Lichtenstern, N. Mücke, U. Aebi, M. Mauermann, and H. Herrmann. Complex formation and kinetics of filament assembly exhibited by the simple epithelial keratins k8 and k18. *Journal of Structural Biology*, 177:54–62, 2012.

[138] J.F. Nolting, W. Möbius, and S. Köster. Mechanics of individual keratin bundles in living cells. *Biophysical Journal*, 107(11):2693–2699, 2014.

[139] N. Wang and D. Stamenovic. Contribution of intermediate filaments to cell stiffness, stiffening, and growth. *The American Journal of Physiology: Cell Physiology*, 279(1):C188–C194, 2000.

[140] M. Plodinec, M. Loparica, R. Suetterlin, H. Herrmann, U. Aebi, and C. Schoenenberger. The nanomechanical properties of rat fibroblasts are modulated by interfering with the vimentin intermediate filament system. *Journal of Structural Biology*, 174(3):476–484, 2011.

[141] M.J. Brown, J.A. Hallam, E. Colucci-Guyon, and S. Shaw. Rigidity of circulating lymphocytes is primarily conferred by vimentin intermediate filaments. *Journal of Immunology*, 166(11):6640–6646, 2001.

[142] P. Kollmannsberger, C.T. Mierke, and B. Fabry. Nonlinear viscoelasticity of adherent cells is controlled by cytoskeletal tension. *Soft Matter*, 7:3127–3132, 2011.

[143] T.M. Magin, P. Vijayaraj, and R.E Leube. Structural and regulatory functions of keratins. *Cell*, 3:2021–2032, 2007.

[144] H. Lu, A. Zimek, J. Chen, M. Hesse, H. Büssow, K. Weber, and T.M. Magin. Keratin 5 knockout mice reveal plasticity of keratin expression in the corneal epithelium. *European Journal of Cell Biology*, 85(8):803–811, 2006.

[145] P. Coulombe, X. Tong, S. Mazzalupo, Z. Wang, and P. Wong. Great promises yet to be fulfilled: defining keratin intermediate filament function in vivo. *European Journal of Cell Biology*, 83(11-12):735–746, 2004.

[146] P.A. Janmey, U. Euteneuer, P. Traub, and M. Schliwa. Viscoelastic properties of vimentin compared with other filamentous biopolymer networks. *Journal of Cell Biology*, 113(1):155–160, 1991.

[147] M. Hesse, T. Franz, Y. Tamai, M.M. Taketo, and T.M. Magin. Targeted deletion of keratins 18 and 19 leads to trophoblast fragility and early embryonic lethality. *The EMBO Journal*, 19(19):5060–5070, 2000.

[148] T. Cao, M.A. Longley, X.J. Wang, and D.R. Roop. An inducible mouse model for epidermolysis bullosa simplex: Implications for gene therapy. *Journal of Cell Biology*, 152(3):651–656, 2001.

[149] N. Walter, T. Busch, T. Seufferlein, and J.P. Spatz. Elastic moduli of living epithelial pancreatic cancer cells and their skeletonized keratin intermediate filament network. *Biointerphases*, 6(2):79–85, 2011.

[150] S. Sivaramakrishnan, J.V. De Giulio, L. Lorand, R.D. Goldman, and K.M. Ridge. Micromechanical properties of keratin intermediate filament networks. *Proceedings of the National Academy of Sciences*, 105(3):889–894, 2008.

[151] M. Beil, A. Micoulet, G. von Wichert, S. Paschke, P. Walther, M.B. Omary, P.P. Van Veldhoven, U. Gern, E. Wolff-Hieber, J. Eggermann, J. Waltenberger, G. Adler, J. Spatz, and T. Seufferlein. Sphingosylphosphorylcholine regulates keratin network architecture and visco-elastic properties of human cancer cells. *Nature Cell Biology*, 5(9):803–811, 2003.

[152] S. Suresh. Biomechanics and biophysics of cancer cells. *Acta Biomaterialia*, 3(4):413–438, 2007.

[153] D.C. Lin, E.K. Dimitriadis, and F. Horkay. Elasticity of rubber-like materials measured by afm nanoindentation. *eXPRESS Polymer Letters*, 1(9):576–584, 2007.

[154] Y.C. Fung. *Biomechanics: mechanical properties of living tissue*. Springer, 1993.

[155] D.C. Lin, D.I. Shreiber, E.K. Dimitriadis, and F. Horkay. Spherical indentation of matter beyond the hertzian regime: numerical and experimental validation of hyperelastic models. *Biomechanics and Modeling in Mechanobiology*, 8:345–358, 2009.

[156] L.R. Treloar. The photo-elastic properties of rubber. part I: theory of the optical properties of strained rubber. *Transactions of the Faraday Society*, 43:277–283, 1947.

[157] Y.C. Fung. *A first course in continuum mechanics.* Prentice-Hall, Inc., 1969.

[158] H. Petroski. *Invention by design: how engineers get from thought to thing.* Harvard University Press, 1996.

[159] Y.C. Fung. Elasticity of soft tissues in simple elongation. *American Journal of Physiology*, 213(6):1532–1544, 1967.

[160] F. Yang. Indentation of an incompressible elastic layer. *Mechanics of Materials*, 30:275–286, 1998.

[161] W.C. Hayes, L.M. Keer, G. Herrmann, and L.F. Mockros. A mathematical analysis for indentation tests of articular cartilage. *Journal of Biomechanics*, 5:541–551, 1972.

[162] G.I. Popov. The contact problem of the theory of elasticity for the case of a circular area of contact. *Journal of Applied Mathematics and Mechanics*, 26(152-164), 1962.

[163] W.T. Chen and P.A. Engel. Impact and contact stress analysis in multilayer media. *International Journal of Solids and Structures*, 8:1257–1281, 1972.

[164] J.P. Caulfield and M.G. Farquhar. The permeability of glomerular capillaries to graded 643 dextrans: identification of the basement membrane as the primary filtration barrier. *Journal of Cell Biology*, 63(883-903), 1974.

[165] J.J. Bozzola and L.D. Russell. *Electron microscopy principles and techniques for biologists.* Jones and Bartlet Publishers, 1999.

[166] P.B. Henrich, C.A. Monnier, W. Halfter, C. Haritoglou, R.W. Strauss, R. Y. Lim, and M. Leoparic. Nanoscale topographic and biomechanical studies of the human internal limiting membrane. *Investigative Ophtalmology and Visual Science*, 53(6):2561–2570, 2012.

[167] S. Brody, T.Anilkumar, S.Liliensiek, J.A. Last, C.J. Murphy, and A. Pandit. Characterizing nanoscale topography of the aortic heart valve basement membrane for tissue engineering heart valve scaffold design. *Tissue Engineering*, 12(2):413–421, 2006.

[168] E.M. Darling, S. Zauscher, and F. Guilak. Viscoelastic properties of zonal articular chondrocytes measured by atomic force microscopy. *Osteoarthritis and cartilage*, 14:571–579, 2006.

[169] https://it.wikipedia.org/wiki/File:Kontakt_Kugel_Ebene.jpg.

[170] https://www.uni-leipzig.de/ pwm/web/section=introductionpage=sfm.

[171] G. Binnig, C.F. Quate, and C. Gerber. Atomic force microscope. *Physical Review Letters*, 56(9):930–933, 1986.

[172] H. Wanga, S. Lacochea, L. Huanga, B. Xueb, and S.K. Muthuswamya. Rotational motion during three-dimensional morphogenesis of mammary epithelial acini relates to laminin matrix assembly. *Proceedings of the National Academy of Sciences*, 110(1):163–168, 2012.

[173] E.K. Dimitriadis, F. Horkay, J. Maresca, B. Kachar, and R.S. Chadwick. Determination of elastic moduli of thin layers of soft material using the atomic force microscope. *Biophysical Journal*, 85(5):2798–2810, 2002.

[174] A.R. Harris and G.T. Charras. Experimental validation of atomic force microscopy-based cell elasticity measurements. *Nanotechnology*, 22, 2011.

[175] D.C. Lin, E.K. Dimitriadis, and F. Horkay. Robust strategies for automated afm force curve analysis- I. non-adhesive indentation of soft, inhomogeneous materials. *Journal of Biomechanical Engineering*, 129:430–440, 2007.

[176] S.F. Nørrelykke and H. Flyvbjerg. Power spectrum analysis with least-squares fitting: amplitude bias and its elimination, with application to optical tweezers and atomic force microscope cantilevers. *Physics: Instrumentation and Detectors*, 2010.

[177] N.A. Burnham, X. Chen, C.S. Hodges, G.A. Matei, E.J. Thoreson, C.J. Roberts, M.C. Davies, and S.J.B. Tendler. Comparison of calibration methods for atomic force microscopy cantilevers. *Nanotechnology*, 14:1–6, 2003.

[178] D. Waschbüsch, S. Born, V. Niediek, N. Kirchgessner, I.Y. Tamboli, J. Walter, R. Merkel, and B. Hoffmann. Presenilin 1 affects focal adhesion site formation and cell force generation via c-Src transcriptional and posttranslational regulation. *Journal of Biological Chemistry*, 284(15):10138–10149, 2009.

[179] S.K. Muthuswamy, D. Li, S. Lelievre, M.J. Bissell, and J.S. Brugge. ErbB2, but not ErbB1, reinitiates proliferation and induces luminal repopulation in epithelial acini. *Nature Cell Biology*, 3:785–792, 2001.

[180] J. Dong, Y. Li, and X. Mo. The study of a new detergent (octyl-glucopyranoside) for decellularizing porcine pericardium as tissue engineering scaffold. *Journal of Surgical Research*, 183:56–67, 2013.

[181] I. Sneddon. The relation between load and penetration in the axisymmetric boussinesq problem for a punch of arbitrary profile. *International Journal of Engineering Science*, 3(1):47–57, 1965.

[182] H. Hertz. Über die Berührung fester elastischer Körper. *Journal für die reine und angewandte Mathematik*, 171:156–171, 1881.

[183] Australian microscopy and microanalysis research facility. Scanning electron microscope: training module.

[184] S. Wilhelm, B. Gröbler, M. Gluch, and H. Heinz. Confocal laser scanning microscopy: principles.

[185] L. Limozin and K. Sengupta. Quantitative reflection interference contrast microscopy (RICM) in soft matter and cell adhesion. *ChemPhysChem.*, 10(16):2752–68, 2009.

[186] S.L. Crick and F.C. Yin. Assessing micromechanical properties of cells with atomic force microscopy: importance of the contact point. *Biomechanics and Modeling in Mechanobiology*, 6:199–210, 2007.

[187] R. Rounsevell, J.R. Forman, and J. Clarke. Atomic force microscopy: mechanical unfolding of proteins. *Methods*, 34:100–111, 2004.

[188] J.L. Hutter and J. Bechhoefer. Calibration of atomic force microscope tips. *Review of Scientific Instruments*, 64(1868), 1993.

[189] L. Ramms, G. Fabris, R. Windoffer, N. Schwarz, R. Springer, C. Zhou, J. Lazar, S. Stiefel, N. Hersch, U. Schnakenberg, T.M. Magin, R.E. Leube, R. Merkel, and B. Hoffmann. Keratins as the main component for the mechanical integrity of keratinocytes. *Proceedings of the National Academy of Sciences*, 110(46):18513–18518, 2013.

A. List of abbreviations

2D	Two dimensional
3D	Three dimensional
AFM	Atomic force microscope
BM	Basement membrane
BSE	Back scattered electrons
BSA	Bovine serum albumine
CB	Cytoskeleton buffer
CO_2	Carbon dioxide
CRS	Cell recovery solution
DMEM	Dulbecco's modified eagle medium
ECM	Extracellular matrix
EGF	Epidermal growth factor
EDTA	Ethylenediaminetetraacetic acid
EHS	Engelberth-Holm Swarm
FA	Formaldehyde
GA	Glutaraldehyde
h	Hours
IC	Intercellular cleft
IF	Intermediate filaments
KO	Knock-out
LatA	Latrunculin A
min	Minutes
OGP	Octyl-β-D-glycopyranoside
PBS	Phosphate buffered saline
R	Radius
RES	Rescue
RT	Room temperature
rpm	Rounds per minute
s.d.	Standard deviation
SE	Secondary electrons
s.e.m.	Standard error of mean
WT	Wild-type

B. List of suppliers

abcam	Cambridge, ENG, UK
Amersham Pharmacia Biotech.	Little Chalfont, ENG, UK
Bal-Tec	Balzers, Liechtenstein
BD Biosciences	Fernwald, Germany
BioRad	München, Germany
BODE Chemie	Hamburg, Germany
Carl Zeiss	Jena, Germany
Cell E&G	Houston, TX, USA
Cell Signaling Tech.	Leiden, The Netherlands
Cressington	Watford, ENG, UK
Dow Corning	Steinfurt, Germany
Eppendorf	Wesseling-Berzdorf, Germany
G.Kisker GbR	Steinfurt, Germany
Heidolph	Schwabach, Germany
Heraeus/Kendro	Hanau, Germany
Ibidi	München, Germany
Invitrogen	Karlsruhe, Germany
Jackson Immunoresearch Laboratories	West Grove, PA, USA
JPK	Berlin, Germany
Kimberly-Clark	Mainz, Germany
Knick	Berlin, Germany
KNF Neuberger Inc.	Trenton, NJ, USA
Life Technologies	Darmstadt, Germany
Meditrade	Kiefersfelden, Germany
Memmert	Schwabach, Germany
Menzel	Braunschweig, Germany
Merck Millipore	Darmstadt, Germany
Mettler-Toledo	Giessen, Germany
Molecular Probes	Waltham, MA, USA
Nanosensors	Neuchatel, Switzerland
Nano World	Neuchatel, Switzerland
Orflo Technologies	Hailey, ID, USA
PAA Laboratories	Freiburg, Germany
Pall corporation	Dreieich, Germany

Polysciences Inc.	Eppelheim, Germany
Progen Biotechnik GmbH	Heidelberg, Germany
Promo Cell	Heidelberg, Germany
Sigma Aldrich	Steinheim, Germany
Sutter Instruments	Novato, CA, USA
Ted Pella, Inc.	Redding, CA, USA
ThermoFisher Scientific	Waltham, MA, USA
UHU	Bühl Baden, Germany
Worthington Biochemical Corporation	Lakewood, NJ, USA
VWR	Darmstadt, Germany
Hilgenberg	Malsfeld, Germany